UNIVERSITY OF CALIFORNIA, MERCED

Phase Behavior and Nanotube Formation in Lipid Membranes

A dissertation submitted in partial satisfaction of the requirements
for the Degree of Philosophy

in

Biological Engineering and Small-scale Technologies

by

Chai Lor

Committee in charge:

Professor Jay E. Sharping, Chair
Professor Linda S. Hirst
Professor Tao Ye
Professor Wei Chun Chin

The Dissertation of Chai Lor is approved, and it is acceptable
in quality and form for publication on microfilm and electronically:

Linda S. Hirst

Tao Ye

Wei-chun Chin

Jay E. Sharping Chair

University of California, Merced
2015

To Mom and Dad

You always pushed me forward, supported me in every way, and kept me on the right path.

To my siblings Xou, Soua, Iaong, Baonhia, and PengXue

Having you all there supporting my back, I am grateful to be your older brother.

To Jesse Thongdy

My savior, my friend, my partner, and my illustrator.

To Linda S. Hirst

The best advisor one could have asked for, your impact on me will never be forgotten.

To my Colleagues

My days are bright because you were there to share the fun, the creativity, and the knowledge. Thank you for the support and friendship, will remember you always.

To my dog Data

Woof Woof Woof

Acknowledgments

I would like to thank everyone in the Hirst Group, most importantly my advisor Linda S. Hirst. She is an intelligent, influential, and an awesome friend that has impacted my life greatly in these past 6 years of working with her. I couldn't have asked for a better advisor than her who has been my savior during my difficult times at the beginning of my graduate studies. She has always been there to share my excitements whether it's big or small. It was through the influences of everyone in the Hirst group that enable me to enjoy doing research, which made 6 years passed by so fast. I had been in the Hirst group since its establishment at UC Merced and will always considered it a special place in my heart. I am proud to announce that I am a student of Linda S. Hirst and a member of the Hirst group.

Big thanks to everyone in the Hirst group, those that have already moved forward to bigger things in their life and those that I will sadly leave behind. Ron Pandolfi, Pradeep Uppamoochikkal, Andrea Rodarte, and Tessa Pinon were supportive labmates and friends with many interesting discussions. Nathan Melton, Makiko Quint, Sheida Tayebeh, Joseph Lopes, Amanda Tan, and Ahmed Elbaradei were supportive and awesome people that I will leave behind. Hopefully, I left a good impression on them to remember me. Thanks to the many undergraduates that came and went but most grateful to Lauren Edwards for being an awesome friend.

Thank you to Jing Xu for a great collaboration with a fun and exciting research project. I learned a lot and am glad that I was able to work with her group. Thank you to Thomas Weiss and this team at SLAC for all the assistance at Beamline 4-2. The knowledge and experiences I gained there are valuable and will continue to benefit me in the future. Thanks to my committee, Jay Sharping, Wei-chun Chin, and Tao Yi for their great advices and support to complete my degree.

I am grateful to all the funding and support from UC Merced. Financial support from Linda Hirst, the Center of Excellence on Health Disparities, UC Merced School of Natural Science (Teaching Assistant), UC Merced of Engineering (Teaching Assistant), and Biological Engineering and Small-scale Technologies (BEST) graduate group.

THANK YOU EVERYONE!!!

Contents

List of Figures

Acronyms and Symbols

AFM	Atomic force microscopy
DHA-PE	1-palmitoyl-2-docosahexaenoyl-sn-glycerol-3-phosphoethanolamine
DOPC	1,2-dioleoyl-sn-glycerol-3-phosphocholine
DPPC	1,2-dipalmitoyl-sn-glycerol-3-phosphocholine
DGS-NTA	1,2-dioleoyl-sn-glybero-3-[(N-(5-amino-1-carboxypentyl) iminodiacetic acid) succinyl] (ammonium salt)
DSC	Differential scanning calorimetry
EDP	Electron density profile
FRAP	Fluorescence recovery after photobleaching
GUV	Giant unilamellar vesicle
K_a	Expansion modulus
K_b	Bending modulus
L_α	Liquid crystalline phase
$L_{\beta'}$	Gel phase
L_d	Liquid disordered phase
L_o	Liquid ordered phase
$P_{\beta'}$	Ripple Phase
S_o	Gel (solid) phase
SAXS	Small angle x-ray scattering
SLAC	Stanford Linear Accelerator Center
SSRL	Stanford Synchrotron Radiation Lightsource
T_m	Transition temperature
WAXS	Wide angle x-ray scattering

Chai Lor Curriculum Vita

Contact

Email: kai.lor87@gmail.com

Website: https://www.linkedin.com/pub/chai-lor//bb/300/321

Phone: 1-559-348-3418

Education

Doctor of Philosophy (Ph. D.): Bioengineering and Small-scale Technologies

January 2010 – October 2015
University of California, Merced – Merced, CA
Area of specialty: Biophysics of lipid membranes
Dissertation: "Phase Behavior and Nanotube Formation in Lipid Membranes"
Advisor: Professor Linda S. Hirst

Bachelor of Science (B.S.): Bioengineering

August 2005 – May 2009
University of California, Merced – Merced, CA
Emphasis: Nanotechnology
Capstone: Enhanced chemiluminescence in microfluidic chip via Shrinky-Dink

Publications

C. Lor, J. Lopes, M.K. Mattson-Hoss, L. S. Hirst, and J. Xu. "Simple Experimental Model to Investigate Force Range for Membrane Nanotube Formation". *Frontiers. Anisotropy in Biomaterials*. Submitted

C. Lor, and L.S. Hirst. "Low concentrations of docosahexaenoic acid significantly modify membrane structure and phase behavior". *Membranes*. Submitted

L.S. Hirst, P. Uppamoochikkal and C. Lor**.** "Phase Behavior and Critical Phenomena in Ternary Lipid Mixtures". LIQUID CRYSTALS. Vol. 38, 11-12, 1735-1747 (2011)

Y. Liu, C. Lor, Q. Fu, D. Pan, L. Ding, J. Liu, and J. Lu. "Synthesis of Copper Nanocatalysts with Tunable Size Using Diblock Copolymer Solution Micelles". J. Phys. Chem. C, 114(13), 5767-5772 (2010)

Presentations

BPS March Meeting 2014 – San Francisco, CA

Poster Title: Low Concentrations of Docosahexaenoic Acid Significantly Modify Membrane Structure and Phase Behavior
Authors: Chai Lor, Linda S. Hirst

UCM Health Disparity Presentation Day April 2012 – Merced, CA

Title: A Brighter Start: Health Disparity in Breastfeeding
Authors: Chai Lor

UCM Student Research Day April 2012 – Merced, CA

Poster Title: Phase Behavior in Model Membranes Containing Docosahexaenoic Acid: An AFM Study
Authors: Chai Lor, Pradeep U.K., Stephanie Chen, Linda S. Hirst

BPS March Meeting 2012 - San Diego, CA

Poster Title: Phase Behavior in Model Membranes Containing Docosahexaenoic Acid: An AFM Study
Authors: Chai Lor, Pradeep U.K., Stephanie Chen, Linda S. Hirst

California APS - Stanford November 2011, Menlo Park, CA

Title: Phase Behavior in Binary Docosahexaenoic Acid/Phosphocholine Lipid Mixture
Authors- Chai Lor, Pradeep U.K., Stephanie Chen, Linda S. Hirst

APS March Meeting 2011 March – Dallas, TX

Title: AFM Study of Lipid Domain in DPPC/DHA-PE/Cholesterol System
Authors: Chai Lor, Linda S. Hirst

California APS - Caltech Pomona November 2010 – Pasadena, CA

Title: Study of Raft Domains in Model Membrane of DPPC/DHA-PE/Cholesterol
Authors: Chai Lor, Linda S. Hirst

Professional Experience

Graduate Research

January 2010 – August 2015

University of California, Merced – Merced, CA

Investigated the effect of docosahexaenoic acid (DHA) content in the gel phase (DPPC) of model binary lipid membranes.

- Characterized lipid structure using SAXS and WAXS at SSRL BL 4-2.
- Analyzed and interpreted power diffraction data using analysis software: Origin Lab and Fit2D.
- Conducted topological study of supported bilayer was conducted using AFM in fluid mode.
- AFM data was analyzed and interpreted using MATLAB and NanoScope Image Analysis.

Designed a temperature chamber for glass and quarts capillaries to use in x-ray scattering experiments.

Assisted in collecting, analyzing, and interpreting SAXS data of nanoparticle/liquid crystal composite materials.

Conducted and designed a system to form lipid nanotubes in a flow cell via linkage system of lipid/kinesin/microtubules.

- Purified kinesin proteins by microtubule affinity.
- Assessed kinesin activity by microtubule gliding via optical trap.
- Generated lipid nanotubes from DOPC GUVs via flow assisted with fluorescence microscopy.

Synthesized Cu nanoparticles arrays as catalysts for growth of ZnO nanowires via chemical vapor deposition.

- Polymerized diblock copolymers and performed chemical analysis via Fourier Transform Infrared (FTIR) spectroscopy.
- Synthesized Cu nanoparticles via diblock copolymer micelles and characterized by AFM.

Safety and Lab Manager

August 2011 – August 2015

University of California, Merced – Merced, CA

Trained new lab members on safety and usage of lab instruments.

Wrote protocols and standard operating protocols (SOPs) for lab instrument and cleaning procedures.

Generated lab chemical inventories, was responsible for ordering of equipment and chemical reagents for the entire lab.

Organized waste and disposal system compliant with EH&S standards.

Teaching Assistant

August 2010 – May 2015

University of California, Merced – Merced, CA

Mentored/managed multiple interdisciplinary engineering capstone projects with local clients: Accurate spatial system in catheter; humidity control and waste disposal for infant incubator; efficient room for CT scanner; compact and portal cart for telemedicine; program algorithm for effective wine tank connection; water recycle system at UC Merced; and reduction of emission of toxic gas from paint spray.

Collected, analyzed, and interpreted evaluation feedback from engineering teams to improve program.

Taught college-level introductory physics, physics honors, and introductory bioengineering.

Conducted physics discussions, lab experiments, office hours, and grading rubrics and formulated exam questions for 6 semesters.

Stanford Synchrotron Radiation Lightsource (SSRL) User BL 4-2

March 2012 – August 2015

Stanford Linear Accelerator Center (SLAC) – Menlo Park, CA

Trained in hutch operation and radiation safety and procedures. – GERT certified

Worked in small team of 3-4 people in rigorous data collection for multiple 24-hour long experiments. This include analysis, interpretation, and optimization for all experiments.

Data collection using SAXS and WAXS on lamellar structure of lipid membrane mixture: DPPC/DHA-PE.

Collected using SAXS experiment on Au nanoparticles and CdSe quantum dots with ligands in the liquid crystals.

Health Disparities Fellow

August 2011 – May 2012

Center of Excellence on Health Disparities, UC Merced – Merced, CA

Took health Disparities and Public Health courses at UC Merced.

Conducted literature research on the effectiveness of breastfeeding compared to formula.

Outreach to BeforeAfterBaby, a nonprofit organization on promoting breastfeeding and effective mother and baby interaction.

Undergraduate Researcher

August 2008 – August 2009

University of California, Merced – Merced, CA

Clean silicon wafer by piranha (H_2SO_4:H_2O_2) with ozone treatment and coating with adhesion solution with spin coater.

Synthesized Cu and Au nanoparticles via block copolymer micelles as template (Lu Lab).

Generate GUVs via electroformation to study separation of lipids using AFM (Hirst Lab).

Center of Computational Biology Intern (Summer)

May 2007 – July 2007

University of California, Merced – Merced, CA

Computer simulation of DHA helixes, protein folding and unfolding, and carbon nanotubes using molecular dynamics (GROMACS). Presented summer research on protein folding at University of Illinois Urbana-Champagne (UIUC).

Specialized Skills

X-ray diffraction: SAXS and WAXS

Atomic force microscopy – dry and fluid mode

Electron microscopy – SEM and TEM

Differential scanning calorimetry

Optical microscopy – fluorescence, optical trap,

Chemical vapor deposition – nanowire growth

Microfluidic chip/microfluidic flow cell

Nanoparticle synthesized via diblock copolymer

Data analysis – Python, MATLAB, Origin Lab

Protein purification – molecular motors

Gel electrophoresis

Abstract

Biological cells are protected by a complex barrier called the lipid membrane. The lipid membrane is a soft material structure consisting of many lipid molecules held together by hydrophobic forces in an aqueous solution. Two simple experimental models were employed to investigate the role of specific lipid molecules in biological membranes. The first model investigated the phase behavior of the binary lipid mixture, 1-dipalmitoyl-2-docosahexaenoyl-*sn*-glycero-3-phosphoethanolamine (DHA-PE) and 1,2-dipalmitoyl-*sn*-glycero-3-phosphocholine (DPPC), using small-angle x-ray scattering (SAXS) and wide-angle x-ray scattering (WAXS). Our results shows that DHA-PE induces phase separation into a DHA rich liquid crystalline (L_{α}) phase and a DHA poor gel ($L_{\beta'}$) phase at overall DHA-PE concentrations as low as 0.1 mol%. In addition, we find that the structure of the $L_{\beta'}$ phase, from which the DHA-PE molecules are largely excluded, is modified in the phase-separated state at low DHA-PE concentrations, with a decrease in bilayer thickness of 1.34 nm for 0.1 mol% at room temperature compared to pure DPPC bilayers. The second model investigated the formation of lipid nanotubes using an anchor system consisting of lipids, kinesin molecular motors, and microtubules in a flow cell. Lipid tubulation was conducted on two different membranes, 1,2-dioleoyl-sn-glycero-3-phosphocholine (DOPC) and DPPC. Lipid nanotubes were pulled from anchored giant unilamellar vesicles (GUVs) by drag force generated from the flow inside the channel. The results showed that DPPC membranes cannot generate lipid nanotubes while DOPC can, which was expected. We find that a drag force of approximately $\approx$ 7.9 pN is sufficient for tubule extraction and that it only requires 1-2 kinesin motor proteins for anchoring the GUV.

Chapter 1

Introduction

1.1 Introduction

In this chapter, the background information of lipids and relevant experimental techniques will be introduced before delving into the research projects in the later chapters. Firstly, the roles of lipid membranes in nature will be covered. The following section will introduce the physical properties of lipid molecules and their effects inside membranes. The next section will be a brief description of a few popular modern techniques used to characterize lipid membranes. Lastly, the chapter concludes with the applications of lipids as biomaterials. Chapter 2 of the dissertation will discuss the theories, techniques, and methods of characterizing the biophysical properties of lipid membranes. Though there are many characterization techniques, we will focus in detail on x-ray scattering. Chapter 3-4 will present the results and discussions of the two projects carried out in this dissertation. The first project examined the interaction of binary lipid mixture of DPPC/DHA-PE. The second project investigated the formation of lipid tubules generated from vesicles using the linkage system of lipid-kinesin-microtubule complex. Chapter 5 will conclude with a summary of the main findings and future works.

1.2 Cell to Lipid Membrane

The study of the lipid membrane has an evolutionary history and is widely studied in great details over the decades. Since the discovery of the cell by microscopist, Robert Hooke, in 1665 with plant cells, researchers have been jumping onto the bandwagon in hopes of unraveling the mysteries of the origin of life [1]. It took over two centuries to confirm that the cell was protected by a barrier called the lipid bilayer [2, 3]. This was because technologies had yet to reach the nanoscale regime. Also, the mechanism of how molecules pass through the lipid membrane was still a mystery. The lipid bilayer is about 6 nm thick and membrane proteins are 2-5 nm in length, which cannot be distinguished by optical microscope. In the late 1900s, the fluid mosaic model was established stating that the cell's plasma membrane encompasses not just lipid molecules, but also membrane proteins, which regulate the passage of huge molecules [4]. The fluid mosaic model also states that the lipid membrane is homogeneous where lipid molecules and membrane proteins randomly diffuse laterally and between monolayers. In 1982, Karnovsky and Klausner conceptualized the idea of microdomains, which are regions of different lipid compositions [5]. This model counters the fluid mosaic model in that the lipid membrane is not homogenous, but consists of organized patches. It was suggested that microdomains help regulate the membrane proteins for the passage of materials through the bilayer. The study of the lipid membrane has come a long way; however, there is still much to be discovered due to the many different types of lipid molecules, membrane proteins, and membrane structures.

1.3 Lipids of the Biological Membrane

The cell's plasma membrane as well as the organelles' lipid membranes both contain different lipid molecules. They are categorized into three types: phospholipid, sphingolipid, and sterol. Phospholipids have a negatively charged phosphate group joined to two hydrocarbon chains by a glycerol group. The phosphate end is polar while the hydrocarbon end is non-polar. They are a major component of the cell membrane, which contribute to the bilayer structure. Common phospholipids found in the cell's membranes are phosphatidylcholine, phosphatidylethanolamine, and phosphatidylserine. Instead of a glycerol, sphingolipids have a sphingosine as a backbone, which is synthesized from the serine amino acid. A common sphingolipid in the membrane is the sphingomyelin, which has a phosphate group attached to the sphingoid base. The roles of sphingomyelin are cell recognition and signal transmission. Lastly, a sterol lipid is made of an alcohol (OH) and four hydrocarbon rings called a steroid. Cholesterol is a sterol lipid found in biological lipid membranes. They are essential lipid molecules in the cell membrane as they directly affect the packing structure of the membrane and regulate activities of certain integral membrane proteins.

1.4 Compartmentalization Role

The cell, which is the essence of life, is protected by the plasma membrane. The main role of the lipid membrane is not only to protect, but compartmentalize the different processes of the cell. All organelles in the cell have different functions to support the life of the cell and should be separated to prevent chaos. Therefore, each organelle has its own unique lipid membrane specific to the function of the organelle. For example, the lipid membrane of the Golgi apparatus is a tubular network where proteins go through several stages to complete its final structure [6]. The double bilayer structure, inner and outer membrane, of the mitochondria allows different agents to pass through its respective barrier. The inner membrane is only permeable to oxygen, carbon dioxide, and water, while the outer membrane is permeable to larger molecules like proteins [7]. Even non-organelles such as ribosomes and liposomes have their own specific lipid membrane for encapsulation of materials. Without a lipid membrane, there is no order to separate the different processes of the cell. The lipid membrane has both micro-scale (compartments) and nano-scale (microdomains) organizations.

1.5 Lipid Fusion

The lipid membrane's fusion and defusion (budding) abilities are very important to cellular life. These processes are called endocytosis and exocytosis. Endocytosis is the process by which the cell takes in outside materials without diffusing them through the plasma membrane. During endocytosis, the membrane forms a small bud that encapsulates the foreign molecule(s) and then buds off from the plasma membrane into the cell in the form of a vesicle. Exocytosis is the opposite, whereby the cell deposits large molecules to the outside of the cell. In the exocytosis process, a vesicle, also known

as a cargo, carries materials and fuses into the plasma membrane. This fusion process breaks the vesicle, thus depositing the materials outside of the cell. The transport of neurotransmitters between neuron cells at the synapses is an example of both endocytosis and exocytosis. In cells, some fusion processes are assisted by membrane proteins for selective fusion. This nature of the lipid membrane enables secure transportation and communication between cells.

1.6 Physical Property

1.6.1 Structure of Lipid molecule and Membrane

The lipid membrane is a bilayer made up of lipid molecules. Lipid molecules are amphipathic, which consist of both a hydrophobic (non-polar) region and a hydrophilic (polar) region, shown in Figure 1.1. It is the anesthetic model by Meyer and Overton that led to the idea that the lipid membrane has properties of both oil and water [8]. The hydrophobic region is the chains of hydrocarbons of varying lengths usually referred to as the tail. The hydrophobic region of each monolayers face each other. The hydrophilic region (head) is the phosphate group, connected to the fatty acid by a glycerol group. In aqueous solution, the hydrophilic region points out towards the water on either side of the bilayer. The lipid membrane was proven to be a bilayer by extracting the cell membrane and spreading it between a water-air interface in a Langmuir Blodgett trough. It was found that the surface area of the spread compared to a cell was at a ratio of 2:1 [3]. It was confirmed through electron microscopy that the hydrophilic region of the bilayer is more densely packed compared to the hydrophobic region [9, 10]. This property of being both hydrophobic and hydrophilic makes the lipid membrane very selective to permeation. Only small molecules like oxygen and water are able to permeate through the barrier but bigger molecules like proteins require membrane proteins to regulate their passage.

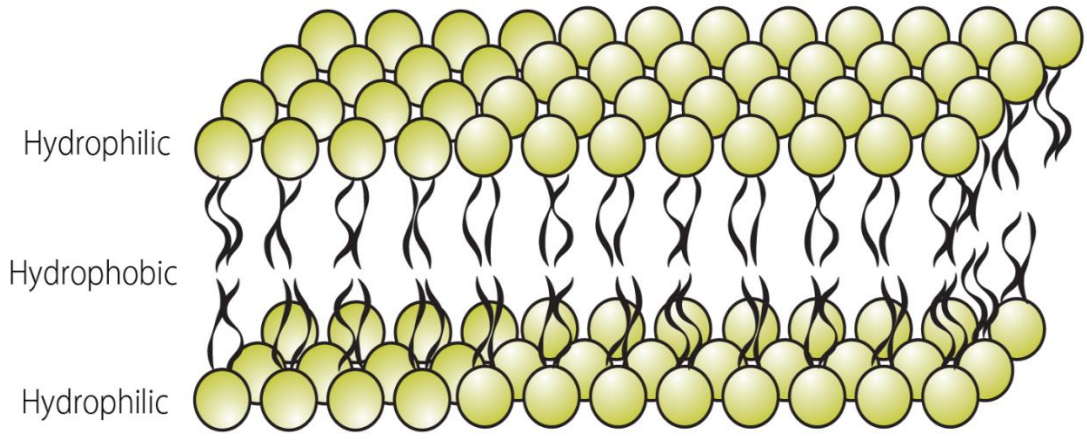

Figure 1.1 Schematic of lipid bilayer.

1.6.2 Lipid Shape – Saturation and Unsaturation

The geometrical distribution of the hydrophobic and hydrophilic regions plays an important role in lipid membrane structures. Lipid molecules are denoted into shapes like a cylinder, a cone, and an inverted cone by the average volume they encompass. Factors such as the hydrocarbon tail length, the number of hydrocarbon tails, and the level of unsaturation all have effects on shape determination. In this project, we will only discuss unsaturation. A lipid molecule is described as unsaturated when its hydrocarbon tail has one or more double bonds. A saturated lipid has no double bond in its hydrocarbon tail(s). The double bonds are either a cis- or a trans-isomer; however, the cis form is commonly found in nature. Opposed to trans-isomer, cis causes a bend in the molecule thus increasing its average volume. The more double bonds a hydrocarbon tail has, the higher its degree of freedom, due to the increased number of conformations the tail can have. Therefore, a saturated lipid is visualized as a cylinder, and an unsaturated lipid is a cone. An inverted cone lipid is typically saturated with the hydrophilic region wider.

1.6.3 Lipid shape – Packing and Curvature

The shape of the lipid influences the structure of the membrane. The packing of inverted cone lipids generate a positive curvature, cone lipids generate a negative curvature, and cylindrical lipids are naturally flat, shown in Figure 1.2. In biological cells, multiple curvatures exist in the plasma membrane of a single cell. Biological cells are not perfectly spherical. For example, red blood cells are oval biconcave disks with a flattened center. Examining the center of the red blood cell, the outer monolayer exhibits a negative curvature while the inner monolayer exhibits a positive curvature. The edge of the red blood cell has the reverse formation. Shape curvature of the lipid membrane is one characteristic that can help identify the lipids of respective local regions. It was shown in plasma membranes of bacteria that lipid molecules in regions of high curvature have more cone lipids and inverted cone lipids [11]. Cells such as neurons have tubular lipid structures of high curvature called dendrites and synapses that form neural networks [12].

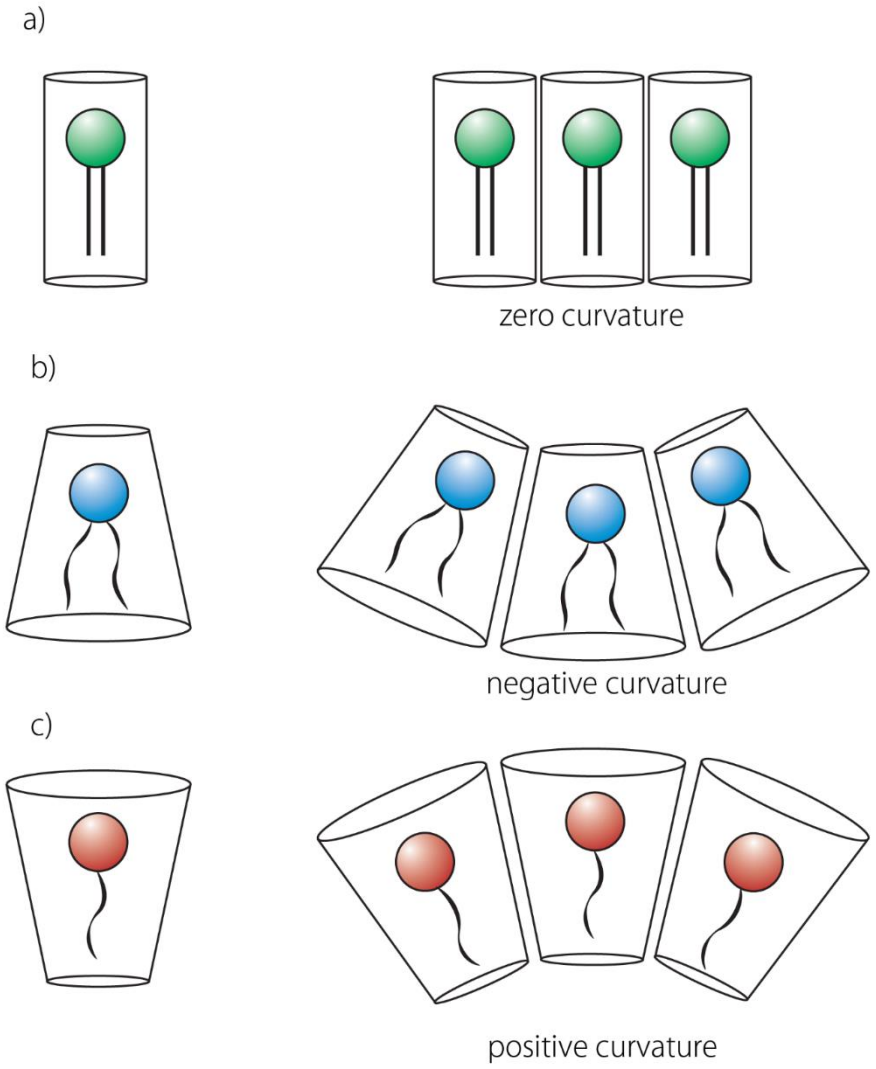

Figure 1.2 Schematic of lipid shape and corresponding curvature. a) zero curvature b) negative curvature c) positive curvature.

1.6.4 Hydration

In an aqueous solution, the vesicle is a typical structure in which the lipid molecules form a bilayer with the hydrophobic tails facing each other and the hydrophilic heads facing the water. Depending on the solvent to lipid ratio, lipid molecules self-assemble into structures that minimize the free energy. At high humidity, a vesicle is the most favorable structure for a lipid bilayer in a free state. If the vesicle makes contact with a surface, it unwinds into a flat bilayer. As the level of humidity is decreased, the lipid membrane transitions into a lamellar phase structure, which is made of stacks of bilayers. Lamellar phase structure can also be obtained by centrifugation because the lipid bilayers are concentrated with low levels of water in the local region. Lastly, at the lowest level of

humidity, the columnal hexagonal structure is favorable where water molecules are trapped inside tubes of reverse micelles. Similarly, if lipid molecules are in nonpolar solvents, the reverse structure patterns occur.

1.6.5 Phases of Lipid Membrane

A lipid membrane that is neither crystal nor liquid but in between is known as a liquid crystal. Crystals have a perfect lattice, long range order, and no diffusion of molecules through the material, while liquid has the opposite features. Both temperature and lipid shape affect the phase of the lipid membrane. Lipid membrane made from same lipid molecule has a unique chain melting or transition temperature (T_m) in which it goes from solid to liquid phase. Below the melting temperature, there is the solid phase known as the gel ($L_{\beta'}$ or S_o) state, which lipid molecules are closely packed (Fig. 1.3a). We will use the symbol $L_{\beta'}$ to represent the gel phase throughout this dissertation. The dense packing of the lipid molecules makes the bilayer resistant to permeation. An example of $L_{\beta'}$ phase membrane in a biological system is human skin cells. They are dead cells with many layers of $L_{\beta'}$ phase membrane that protect many foreign agents from entering the body [13]. Above T_m, the lipid membrane is in a liquid disordered (L_d) state where there is high lateral mobility and high degree of freedom which enable many conformational states of the lipid tails (Fig. 1.3b). A membrane with liquid disordered phase is loosely packed, resulting in increased permeability. The liquid ordered (L_o) phase is also known as lipid raft, which is a special phase obtained by the addition of cholesterol (Fig. 1.3c). Cholesterol incorporates into the hydrophobic region of the bilayer. Cholesterols fill in empty spaces of the hydrophobic region occupying the free spaces of flexible lipid molecules. In result, they reduce the degree of freedom from flexible lipid molecules. Both the L_d phase and L_o phase are subcategories of the L_α phase. Since the following projects does not contain any cholesterol, the symbol L_α will only represent the L_d phase throughout the rest of the dissertation. The ripple ($P_{\beta'}$) phase is another special phase that has a 2D regular structure with coexistence of $L_{\beta'}$ phase and L_α phase (Fig. 1.3d). The ripple phase appears as the intermediate phase before the $L_{\beta'}$ phase transitions into L_α phase [14]. In the process of transitioning into L_α phase by increasing the temperature, part of the $L_{\beta'}$ phase becomes L_α phase. The presence of both phases causes the structure of the bilayer to be in zigzag formation. The differential scanning calorimetry (DSC) is an accurate and common instrument used to detect the transition temperature of a membrane when it changes from one phase to another.

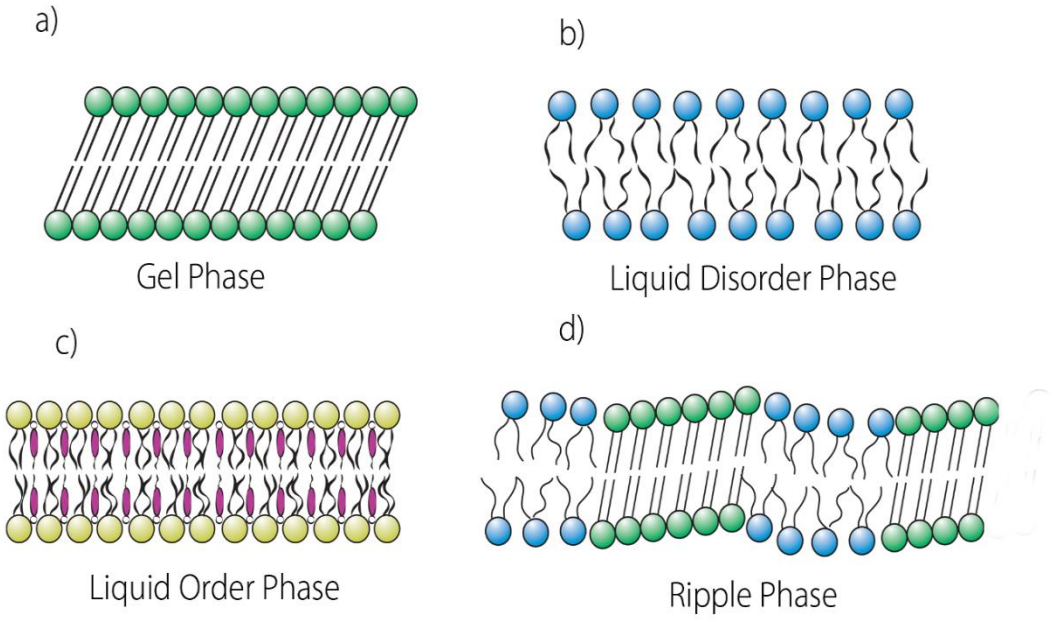

Figure 1.3 Schematic of lipid phases. a) gel (S_o) phase b) liquid disordered (L_d) phases c) liquid ordered (L_o) phase d) ripple ($P_{\beta'}$) phase.

1.6.6 Lipid Domains – Phase Separation

Over the past few decades, it was well studied that the cell membrane was not a random ordering of lipid molecules, but consisted of distinct regions called lipid domains that have different compositions, shown in Figure 1.4 [5, 15]. The theory of micro-domains started from temperature experiments on lipid membrane where they were considered as clusters of higher ordered phases [5, 16]. It was hypothesized that these micro-domains facilitated cellular processes at the membrane interface between the interior and exterior environment. Membrane proteins have been shown to have preference in certain lipid phases. For example, the protein, soluble N-ethylmaleimide-sensitive factor attachment protein receptor (SNARE), has been shown to have high preference for lipid rafts [17, 18]. SNAREs are transmembrane proteins that play an important role in membrane fusion. The presence of lipid domains occurs when there is phase separation in lipid mixture. When mixing one lipid into another, same or similar lipid molecules prefer to reside with each other. However, at low concentration, the probability of finding another similar molecule is low. At higher concentration, similar molecules find each other more readily and form domains. An example is DOPC/DPPC mixture at room temperature. There is no phase separation under 10 mol% of DOPC and the lipid membrane is in $L_{\beta'}$ phase. Between 10-60 mol% of DOPC, there is phase coexistence with many domains of nano and micron sizes. Beyond 60 mol% of DOPC, the whole lipid membrane transitions into the liquid disordered phase [19]. In phase coexistence, each phase has a unique ratio of

both lipids, which is determined by phase boundary. Phase boundary is the concentration at which a new phase is exhibited. In the DOPC/DPPC mixture, the $L_{\beta'}$ phase has a mole ratio of 1:9 DOPC/DPPC, while the liquid disordered phase has a mole ratio of 6:4 DOPC/DPPC.

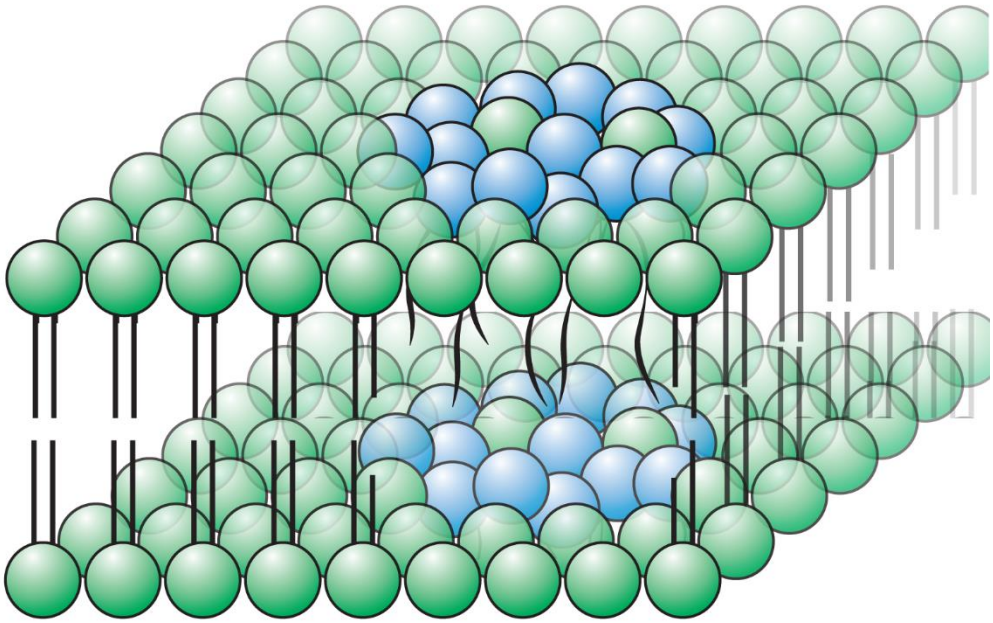

Figure 1.4 Schematic of lipid domain.

1.6.7 Elasticity

The lipid membrane exhibits elastic property due to its ability to stretch or bend without breaking the membrane. The elasticity of the membrane is measured by experimental techniques using an applied mechanical force. In lipid bilayer mechanics, there are two types of elastic modulus: the area expansion modulus, k_a, the bending modulus, k_b. The k_a describes the resistance to expansion within the plane when a force parallel to the plane is applied. In this condition, the distance between neighboring lipid molecules of the whole membrane increases until the break point. The k_b describes the resistance to bending of the membrane when a force perpendicular to the plane is applied. In bending modulus, only a local area experiences the force; the distance between lipid molecules in the local region increases until it breaks. Lipid molecules in the membrane are held together by the hydrophobic force between the molecules. When the lipid molecules are stretched too far apart, the lipid membrane breaks. For a vesicle, it ruptures and forms smaller vesicles. $L_{\beta'}$ phase membrane is less elastic compared to a liquid disordered phase membrane because the lipid molecules are tightly packed. Therefore, it more difficult for foreign materials to permeate through the $L_{\beta'}$ phase, as seen in skin cells [13].

1.7 Modeling of Lipid Membranes

The plasma membrane consists of different classes of lipid. Mimicking the plasma membrane to understand the role of each lipid component is a challenging and complicating task because there are too many factors to consider. Therefore, lipid researchers start with a single lipid membrane model to understand the biophysical property of the lipid molecule of interest and the effect in membrane behavior. Models of single, binary, and ternary mixtures have been extensively studied; however, only a small percentage have been investigated. In single lipid membrane, there are two factors, hydrophobic and hydrophilic, which affect membrane behavior. The addition of a second lipid introduces two more factors. Experimental parameters such as temperature, pressure, hydration, and electrostatic complicate the system even further. Due to the many factors involved in modeling lipid membrane, mimicking plasma membrane is still a long way off.

A single lipid membrane model only provides information about the property of its molecule, which is far from mimicking the plasma membrane. Therefore, it is necessary to model membrane with multiple lipid components. When modeling lipid mixture with components that are very similar, it is difficult to determine the role of each lipid. Lipid membrane models have been simplified to contain 2 or 3 different lipid classes. Common lipid models contain a mixture of saturated lipid, unsaturated lipid, sterol, and membrane protein. Lipid modeling has opened new insights regarding the structures and behaviors of biological membranes. The discovery of lipid domains and lipid rafts from models changed the accepted idea of the fluid mosaic model. Over the decades, lipid membrane models have expanded from understanding the cell to new research topics such as biomaterials, membrane toxicity, and molecular dynamics, to name a few.

1.8 Phase Diagram

Experimental phase diagrams provide information about the interaction between the constituent lipid molecules. Binary and ternary lipid mixtures have been well studied to exhibit phase coexistence at critical concentrations and temperatures. However, there are still controversies concerning the true phase diagram because there are disagreements between phase diagrams of same mixture that were generated from different techniques. Tie-lines in phase diagrams are a useful method to identify the composition of phases in the coexisting region. All points along the same tie-line have the same composition but the area ratio of each phase changes as you move along the tie-line.

1.9 Characterization Techniques

Various experimental techniques were used to characterize the physical properties of lipids in model systems and cell membranes. There are many controversies in lipid research due to the advantages and disadvantages associated with different techniques and methods. An example is the use of labeled lipid molecules to study phase behavior via fluorescence microscopy. Labeled lipid molecules are added to the mixture in order to observe lipid structures because the bilayer thickness is below the optical resolution. However, labeled lipid molecules are considered as contaminants, which can alter the natural behavior of the mixture. In this section, we will briefly discuss a few popular techniques used to characterize properties of lipid membranes.

1.9.1 Fluorescence Microscopy

Fluorescence microscopy is a very popular technique used to characterize micro-structures and lipid phases. Different structures of lipid membranes such as lipid tubules, giant unilamellar vesicles (GUVs), and multi-lamellar vesicles can be observed. The use of GUVs and supported single bilayer are common sample preparation methods. Only small amounts of labeled lipid molecules, 0.05 mol%, were added to the mixture to prevent any significant effects to the membrane behavior. In phase behavior experiments, the labeled lipid molecule is chosen to selectively partition into the preferred phase. Fluorescence recovery after photobleaching (FRAP) is a quick and easy technique used to determine the diffusion coefficient of lipid membranes. A selected region is bleached by an intense energy beam, which destroys the fluorescent probe. After the beam is removed, the bleached region recovers gradually because unbleached lipid molecules randomly diffuse into the bleached region while bleached lipid molecules diffuse outward.

1.9.2 Atomic Force Microscopy

Atomic force microscopy (AFM) is a powerful tool used to characterize nano-scale physical properties. AFM uses a cantilever with a fine tip to probe the surface topology of any sample. It is not limited to spatial resolution; therefore, it provides an exact image of the sample's surface. This method works in both air and fluid environments, which is ideal for lipid membranes. AFM is used to characterize lipid phases and elastic properties of the lipid membrane. The AFM is a very sensitive tool that it is able to detect the height difference of different phases at angstrom scale. Point spectroscopy is the technique used to measure the elastic. The cantilever is a sensitive spring that measures the resistance of the lipid membrane.

1.9.3 X-ray Scattering

X-ray scattering is a powerful instrument used to characterize the regular structure of materials. Small angle x-ray scattering (SAXS) and wide angle x-ray scattering (WAXS) are techniques used to look at repetitive structures at the nanoscale range. Synchrotron radiation is one of the most powerful tools in x-ray scattering that utilizes an intense beam compared to an in-house x-ray beam. Due to its strong source of x-ray, data collection is reduced from hours to seconds. Lipid bilayers are centrifuged to condense the bilayers into stacks forming lamellar structure for x-ray scattering experiments. Scattering from the lamellar structure yields information on the spacing between each bilayer and the molecular packing of the lipid molecules. Electron density profile of the bilayers can also be reconstructed from the scattering data to determine the distance of the water region, hydrophobic region, and hydrophilic region in each stack.

1.9.4 Nuclear Magnetic Resonance (NMR)

Solid state NMR spectroscopy is a popular technique in lipid membrane research because it yields information about the dynamics, membrane phases, and molecular structures. This technique utilizes the spin of nuclei interaction to magnetic or electric field by using deuterated hydrogens. By analyzing the spins, the interaction of molecules with its neighboring molecules can be determined.

1.10 Lipids as Biomaterials

Lipid molecules are essential biomolecules necessary for the survival of cells. In nature, lipid molecules exist everywhere at the interface between polar and nonpolar environments. In other words, lipids are natural surfactants. Surfactants are compounds that lower the surface tension between liquids and solids. There are many applications for surfactants such as detergents, dispersants, emulsifiers, etc. Due to the unique properties of lipids, lipids have been extracted from living species and then synthesized for applications. Aside from being a great source of surfactants, its role of compartmentalization is also utilized in microfluidic chips to keep different solvents separated [20, 21]. Lipids have a big advantage in drug delivery applications in the medical field because of its bio compatibility. Drugs can be encapsulated in liposomes and released at targeted locations [22].

1.11 Conclusion

In this thesis, we first investigated a unique binary lipid mixture of 1, 2-dipalmitoyl-sn-glycerol-3-phosphocholine (DPPC)/ 1-palmitoyl-2-docosahexaenoyl-sn-glycerol-3-phosphoethanolamine (DHA-PE) due to their popularity in the medical field. DHA has been shown to have beneficial health outcomes in humans of all ages. Through clinical trials, DHA has shown positive effects in cardiovascular disease [23], arthritis [24], and infant development [25, 26]; however, the physical effects on the lipid membrane at the

microscale and nanoscale are still largely unexplored. It is a lipid that cannot be synthesized by the body and can only gained through diet. SAXS was employed to study the phase behavior of the mixture DPPC/DHA-PE at low DHA-PE concentration. We also explored the transformation of lipid vesicles into cylindrical tubes. Lipid nanotubes were pulled from GUVs of 1, 2-dioleoyl-sn-glycerol-3-phosphocholine (DOPC) via the linkage system of lipid/kinesin/microtubule and assisted flow.

1. Gest, H. “The discovery of microorganisms by Robert Hooke and Antoni Van Leeuwenhoek, fellows of the Royal Society". Notes and records of the Royal Society of London **2004**, 58 (2), 187–201
2. Fricke, H. The electrical capacity of suspensions with special reference to blood. *Jour of Gen Physio* **1925**, 9, 137-152
3. Gorter, E. and Grendel, F. On bimolecular layers of lipids on the chromocytes of the blood. *Jour of Exp Med* **1925**, 41, 439-443
4. Singer, S. J. and Nicolson, G. L. The Fluid Mosaic Model of the Structure of Cell Membranes. *Science* **1972**, 175, 720–31
5. Karnovsky, M. J.; Kleinfeld, A. M.; Hoover, R. L.; Klausner, R. D. The concept of lipid domains in membranes. *The Jour of Cell Biol* **1982**, 94 (1), 1–6
6. Mollenhuer, H.H. and Morre, D.J. The tubular network of the Golgi apparatus. *Hist. Cell Biol.* **1998**, 109(5-6), 533-43
7. Schenkel, L.C. and Bakovic, M. Formation and regulation of mitochondrial membranes. *Int Jour Cell Biol* **2014**, 709828
8. Hintzensterna, U. V.; Schwarzb, W.; Goerigc, M.; Petermann, H. Development of the "lipoid theory of narcosis" in German-speaking countries in the 19th century: from Bibra/Harless to Meyer/Overton. *The history of anesthesia* **2002**, 1242, 609-612
9. Robertson, J. D. The ultrastructure of cell membranes and their derivatives. *Biochem Soc Symp* **1959**, 16, 3-43
10. Robertson, J. D. The molecular structure and contact relationships of cell membranes. *Prog Biophys and Biophys Chem* **1960**, 10, 343-418.
11. Huang, K. C.; Mukhopadhyay, R.; Wingreen, N. S. A curvature-mediated mechanism for localization of lipids to bactorial poles. *PLOS Comp. Biol.* **2006**, 2, 1357-1364
12. Ramirez, O. A.; Hartel, S.; Couve, A. Location matters: the endoplasmic reticulum and protein trafficking in dendrites. *Biol Res* **2011**, 44, 17-23
13. Norlén, L. Skin Barrier Structure and Function: The Single Gel Phase Model. *Jour of Invest Derma* **2001**, 117, 830–836
14. Rappolt, M.; Rapp, G. Structure of the stable and metastable ripple phase of dipalmitoylphosphatidylecholine. *Eur. Biophys. J.* **1996**, 24, 381-386
15. Philip L. Yeagle, “The Structure of Biological Membranes” 2nd Ed. CRC press (2004)
16. Stier, A.; Sackmann, E. Spin labels as enzyme substrates heterogeneous lipid distribution in liver microsomal membranes. *Biochi et Biophys Acta (BBA) - Biomem* **1973**, 311, 400–8
17. Lang, T.; Bruns, D.; Wenzel, D.; Riedel, D.; Holroyd, P.; Thiele, C.; Jahn, R. SNAREs are concentrated in cholesterol-dependent clusters that define docking and fusion sites for exocytosis. *The EMBO Jour*. **2001**, 20(9), 2202-2213
18. Chamberlain, L.H.; Burgoyne, R.D.; Gould, G.W. SNARE proteins are highly enriched in lipid rafts in PC12 cells: Implications for the spatial control of exocytosis. *PNAS*. **2001**, 98(10), 5619-5624

19. Schmidt, M.L.; Ziani, L; Boudreau, M.; Davis, J. H. Phase equilibria in DOPC/DPPC: Conversion from gel to subgel in two component mixtures. *Jour Chem Phys* **2009**, 131, 175103
20. Nisisako, T.; Portonovo, S.A.; Schmidt, J.J. Microfluidic passive permeability assay using nanoliter droplet interface lipid bilayers. *Analyst*. **2013**, 138(22), 6793-800
21. Sekine, Y.; Abe, K.; Shimizu, A.; Sasaki, Y.; Sawada, S.; Akiyoshi, K. Shear flow-induced nanotubulation of surface-immobilized liposomes. *RSC Advances* **2012**, 2, 2682-2684
22. Allen, T.M. and Cullis, P.R. Liposomal drug delivery systems: from concept to clinical applications. *Adv Drug Deliv Rev* **2013**, 65, 36-48
23. McLennan, P.; Howe, P.; Abeywardena, M.; Muggli, R.; Raederstorff, D.; Mano, M.; Rayner, T.; Head, R. The cardiovascular protective role of docosahexaenoic acid. *Eur. J. Pharm.* **1996**, 300, 83-89
24. Kremer, J.M.; Lawrence, D.A.; Jubiz, W.; DiGiacomo, R.; Rynes, R.; Bartholomew, L.E.; Sherman, M. Dietary fish oil and olive oil supplementation in patients with rheumatoid arthritis. Clinical and immunologic effects. *Arthritis Rheum* **1986**, 3**3**, 810-820
25. J. Dyerberg, A. Leaf, C. Galli, ISSFAL board statement: Recommendation for the essential fatty acid requirement for infant formulas. *J. AM. Coll. Nutr.* **1995**, 14, 213-214
26. N.J. Salem, H.Y. Kim, J.A. Yergey, Omega-3 fatty acids in growth and development. *Academic Press*. New York. **1986**, 319-351

Chapter 2

Theories and Methodologies

2.1 Introduction

This chapter will start by covering the theory of x-ray scattering. X-ray scattering is a powerful tool used to extract structural information from materials with repetitive structures. The fundamental principles of x-ray scattering from a single electron will be discussed and expanded to regular structures. The next section will discuss the experimental setup and sample preparations for x-ray scattering experiments. Then an explanation of how x-ray data were analyzed and interpreted. The following section will cover the mechanics of elastic properties in lipid membranes. The lipid bilayer is a soft material that can be de-formed into various structures. The last section of this chapter will discuss the methods of lipid sample preparation and analysis.

2.2 X-ray Scattering

2.2.1 Synchrotron

X-rays are electromagnetic waves on the wavelength of angstrom. The short wavelength enables the detection of repetitive structures at the angstrom and nanometer scale, which are atomic and molecular packings. In third generation x-ray instruments known as synchrotron, x-rays are generated by accelerating and decelerating charged particles moving at very high speed. A synchrotron is a large cyclic ring that moves charged particles in a circle using bending magnets and straight magnets called undulators. The bending magnets keep the moving particles along the path of the circle. The undulators, an array of alternating pairs of magnetic plates, are the main generator of x-rays that execute small amplitude oscillations on the particles, shown in Figure 2.1. In other words, x-rays are generated when the fast moving particles accelerate and decelerate each time they pass through each pair of magnets. The x-rays produced from each undulator in the ring overlap and interfere with each other and create a coherent beam with narrow beam output and high power. X-rays produced from the synchrotron are stored in the ring and then extracted to each beamline around the ring, which is where individual labs were setup.

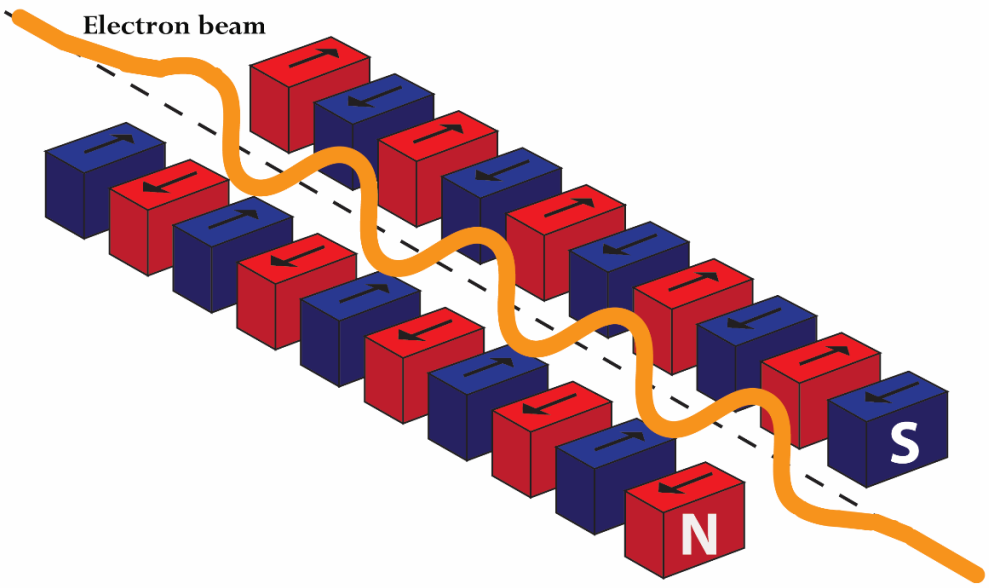

Figure 2.1 Schematic of an electron beam passing through an undulator.

2.2.2 Elastic Scattering

Elastic scattering is when the incident and scattered waves have no change in energy. X-rays have both electric and magnetic waves that oscillate in the direction of propagation. When the oscillating wave incident on the electron, it causes the electron to also oscillate at the same amplitude and frequency as the incident wave. Similar to how x-rays are produced with undulators, the electron's acceleration and deceleration re-radiate its own x-ray like scattered waves. This can be expanded into scattering from an atom of a crystal structure. From Figure 2.2, assume a unit cell where an electron at position M and r_e from the nucleus occupies a space of dS. The unit cell is R_j distance from the origin (O).

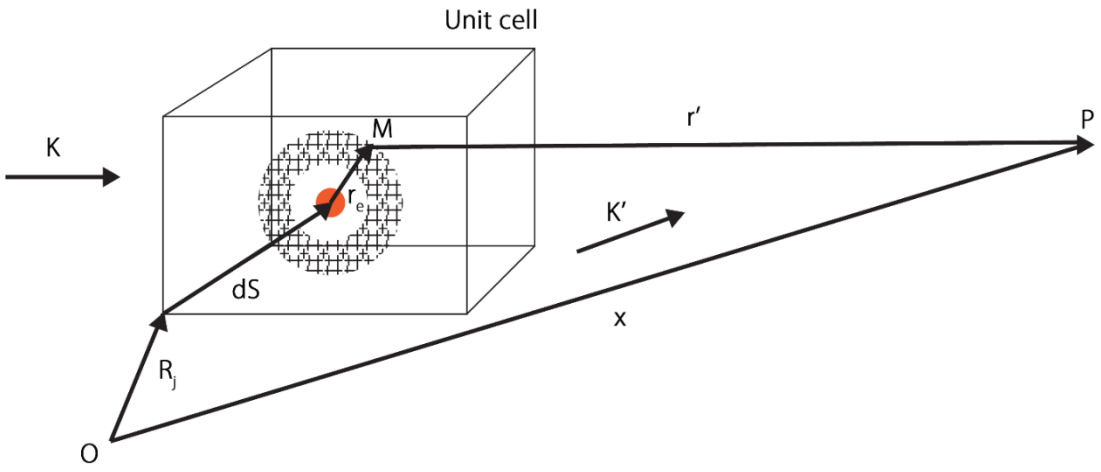

Figure 2.2 Schematic of x-ray scattering from an atom.

When the x-ray beam incidents the electron, the amplitude of the incident wave at a distance r from the origin can be defined as

$$A = A_o e^{i(k.r-wt)} \quad \text{(Eq. 1)}$$

where A is the amplitude, w is the frequency, t is the time. The term $e^{i(k.r-wt)}$ is the simple expression of $sin(kr - wt)$, which is from a wave function. When the electron re-radiate its own x-ray, the scattered wave is defined as

$$A_s = A_o e^{ik.(R_j+dS+r_e)} \quad \text{(Eq. 2)}$$

where A_s is the amplitude of the scattered wave. We can determine the intensity of the scattering at some distance of P as

$$dA_s = Ce^{ik.(R_j+dS+r_e)}p(r)d^3r_e \quad \text{(Eq. 3)}$$

where C is a constant and $p(r)$ is the electron density of the atom. There are three parts to be considered for the scattering: the incident phase factor, the scattering phase factor, and the probability of hitting an electron within the unit cell. We can simplify the scattering phase factor because $\Delta k = k' - k$ and rewrite it as

$$dA_s = Ce^{[i\Delta k.(R_j+dS+r_e)+ik'.x]}p(r)d^3r_e \qquad \text{(Eq. 4)}$$

where x is the distance of the intensity of the scattered x-ray at point P. This function only describe scattering from a single atom, to expand it to a crystal, the scatterings from each electron, atom, and unit cell are to be summed resulting in

$$A = C\left[\sum_{R_j} e^{-i\Delta k.R_j}\right] \cdot \left[\sum_S \left(\int p_s(r_e)e^{-i\Delta k.r_e}d^3r_e\right)e^{-i\Delta k.dS}\right]e^{ik'.x} \qquad \text{(Eq. 5)}$$

This is known as the atomic scattering factor, or structure factor, which is a Fourier transform of the electron density of the unit cell. There are actually 3 terms to the atomic scattering factor, but the latter two are energy dependent and become large only near atomic absorption edges. If the absorption energy of the material is known, then the x-ray beam can be tuned to that specific frequency. Simply stated, this technique is known as resonant scattering, and it is useful in elemental analysis to determine the element by controlling the frequency.

2.2.3 Bragg's Law

Bragg's Law was discovered by William Lawrence Bragg and William Henry Bragg who found that scattering from solid crystals produces diffraction patterns [1]. In solid materials, the high order of periodic packing in atoms or molecules have planes with equal layer spacing. Scattering from a plane applies the same principle as scattering from an electron. When an incident beam is reflected from the planes of the material at the same angle, ABC = DEF, the scattered rays exit the material in phase and constructively interfere to produce a diffraction pattern, shown in Figure 2.3. The angle is equal to $n\lambda$ thus leading to Bragg's Law

$$n\lambda = 2dsin\theta \qquad \text{(Eq. 6)}$$

where n is the order, λ is the incident wavelength, θ is the angle of scattering, and d is the layer spacing. By using this law, we can determine the layer spacing of periodic planes. Bragg's Law can be applied to scattering from stacks of lipid bilayers in lamellar phase structure to determine the thickness of the bilayers.

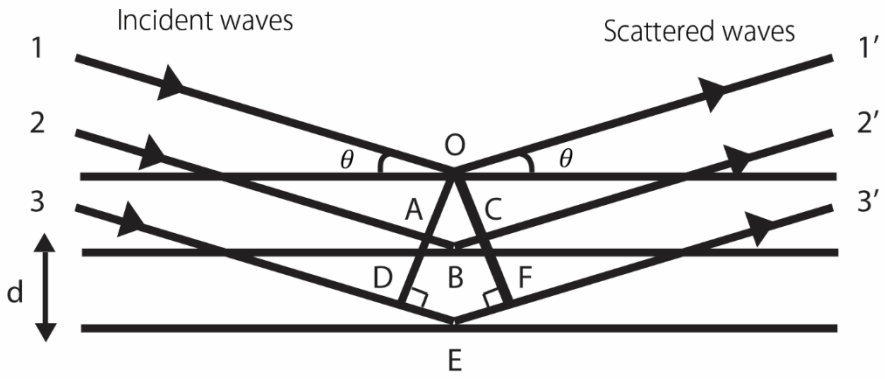

Figure 2.3 Schematic of Bragg's diffraction.

2.2.4 Length Scale of X-ray Scatting

X-ray scattering provides information of the structure of the interested material in a wide range of scales, ranging from angstroms to microns. However, data collection for analysis of the full range is difficult. It is divided into four sections: WAXS (0.1 nm-1 nm), mid-angle x-ray scattering (MAXS) (1 nm-5 nm), SAXS (3 nm-50 nm), and ultra-small angle x-ray scattering (USAXS) (15 nm-2 μm). The camera length determines the working range, which is the distance from the sample to the detector. The shorter the camera length, the smaller the scale range detected. In this dissertation, we collected data from lipid membranes using both WAXS and SAXS methods. SAXS is used to determine the spacing between bilayers. WAXS is useful for determining the chain packing of the lipid molecules.

2.2.5 X-ray Scattering of Lipid Lamellar Structure

In lamellar structure, the lipid bilayers stack on top of each other with a water region between each consecutive bilayer. The repetitive pattern of each layer is half of the water region above the bilayer, the full bilayer, and the following half of the water region below. Each layer is considered a plane stacking in one dimension. When an incident beam, k, is reflected from the plane, it produces a scattered wave, k' defined as

$$Q = (\frac{2\pi}{\lambda})(k' - k) \qquad \text{(Eq. 7)}$$

where the Q vector is in Q -space known as the reciprocal space. Each scattered ray has a Q vector with an origin at O' in Q -space that is $\frac{2\pi}{\lambda}$ from the real space. Since there are many scattering in every direction, this will generate a sphere of radius $\frac{2\pi}{\lambda}$ for each Q vector called the Ewald sphere. However, there is only constructive interference for

planes that intersect with the Ewald sphere. In synchrotron x-ray scattering, it's a powder diffraction technique that produces ring pattern. Each ring represents the q-space of the layers in real space defined as

$$q = \frac{4\pi sin(\theta)}{\lambda} \quad \text{(Eq. 8)}$$

because powder diffraction is the full scattering vector. Solving the above equation for $sin(\theta)$ and substitute into Bragg's Law yields

$$d = \frac{2\pi}{q} \quad \text{(Eq. 9)}$$

Powder diffraction data is a ring pattern and q is measured as the radius of each ring. The d value is inversely proportional to q, which means the lower q results in bigger d-spacing. Lipid bilayer stacks with long range order have many sharp peaks in the diffraction pattern that are multiples of the first order. Short range order returns fewer peaks and is broader.

2.3 X-ray Experimental

2.3.1 X-ray Scattering Setup

SAXS and WAXS measurements were carried out at the Stanford Synchrotron Radiation Lightsource (SSRL) beamline 4-2 at the Stanford Linear Accelerator Center (SLAC). X-ray beam was drawn from the storage ring that accelerated charged particles. The setup took place inside a unit called a hutch, which must closed and locked prior to operating the beam. The hutch barrier provides a shielding from exposure to radiation. The samples are placed between the beam exit and the detector. During operation, the x-ray exits from the tube and incident on the sample in its path; scattered waves from the sample are projected onto the detector, shown in Figure 2.4. We used a wavelength of 1.127 Å (11 keV) with a 1.7 m and 0.2 mm distance from sample to detector for SAXS and WAXS respectively. Powder diffraction patterns were recorded on a CCD detector (Rayonix MX225-HE) using a 1s exposure time. For instrument calibration, we used silver behenate (d_{001} = 58.83 Å) with a sensitivity of 1 Å. Capillaries were mounted into an aluminum temperature chamber designed specifically for this beamline. Using this apparatus, capillary temperature was controlled to an accuracy of ±0.25 K by passing water through tubes into the chamber. Thermistors were mounted close to the sample to monitor the temperature. After collecting powder diffraction patterns using a CCD camera, SasTool software at the beamline was used for radial integration (producing plots of scattered intensity as a function of scattering vector, **q**).

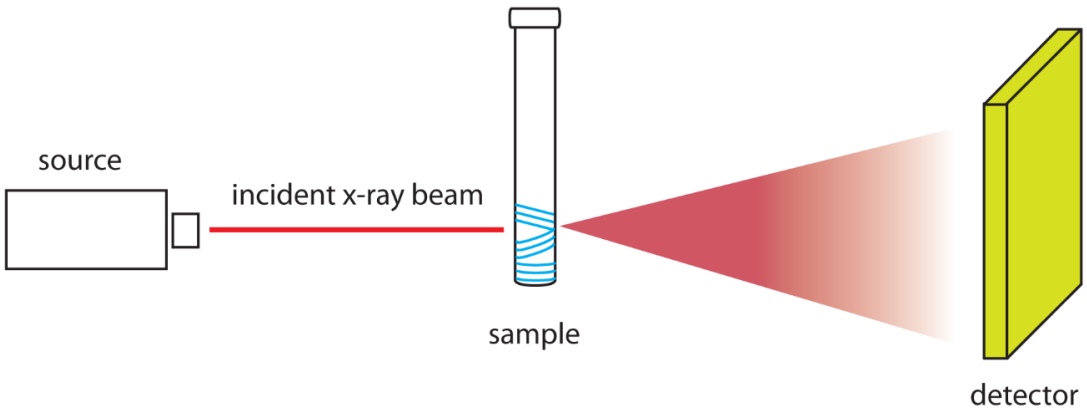

Figure 2.4 Schematic of x-ray scattering from sample onto detector.

2.3.2 Capillary Temperature Chamber

A temperature chamber for capillaries was designed by postdoctoral Pradeep Uppamoochikkal and machine shopped in the Machine Lab at UC Merced. The chamber was made from an aluminum block to conduct the heat from the water cycling through the block, shown in Figure 2.5. There are 8 holes of 4 mm in diameter at the top of the chamber for the insertion of capillaries. In the middle of the chamber is a window at 3 cm x 7 cm, which the bottom of the capillaries are exposed for the x-ray beam. Two thermistors were placed inside the window to measure the temperature inside. Mylar or Kapton was used to seal up the window on both sides to reduce heat escaping. The whole aluminum chamber was encased in styrofoam for heat insulation, except the top and window region. The entire chamber was mounted and locked onto an optical plate stage with x-y movement capability. This enables stability and control of exposed regions to the beam. The thermistors were connected to a multimeter, which displayed the resistance corresponding to the temperature. The multimeter was placed inside the hutch and the resistance readings were viewed from cameras set within the hutch. During the experiment, changes to the temperature were done by heating or cooling of the water through a chiller set outside of the hutch. At higher temperatures, the set temperature of the chiller is higher than the temperature from the thermistor due to heat dissipation.

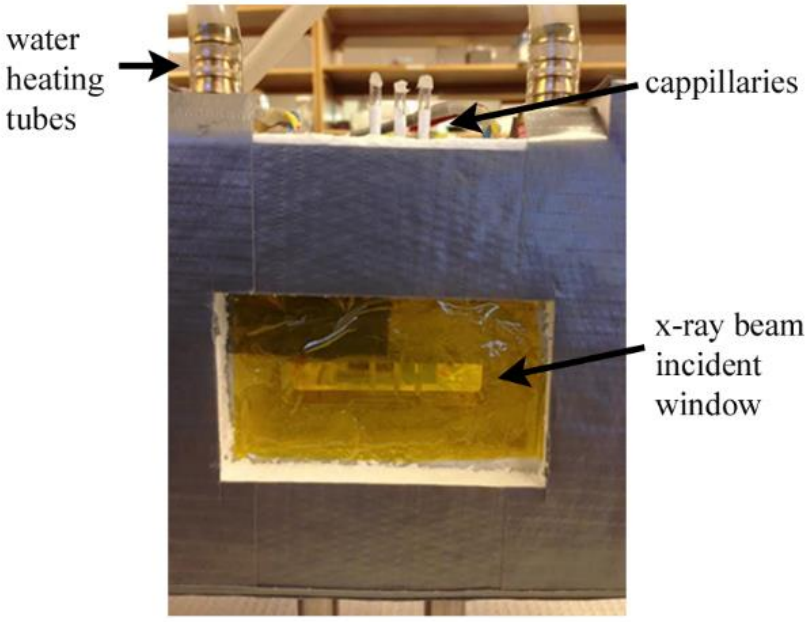

Figure 2.5 Aluminum temperature chamber with capillary samples inserted for x-ray scattering experiment.

2.3.3 Analysis of X-ray Scattering Data

Origin Lab is the main software used to analyze the data from the synchrotron runs. Data obtained included image files of the powder diffraction ring patterns, shown in Figure 2.6. Additionally, ASCII files were obtained through the SasTool software from SLAC, which were plots of scattering q vs. intensity for SAXS (Fig. 2.7) and WAXS (Fig. 2.8) as examples. The software Fit2D was used to view the image files to confirm full diffraction rings. A full ring pattern indicates that there is scattering from layers in every direction with respect to the incident beam. Origin Lab was utilized to analyze the peak position and q-value. Then, the d-spacing was calculated using equation 9. When fitting the peaks, it is ideal to subtract the background scattering such as scattering from water, Kapton film, and glass capillary. This is not necessary for SAXS because the background scattering is outside of the q range of the bilayers. However, for WAXS data, it is necessary to subtract scattering from water.

Figure 2.6 Powder diffraction ring pattern of DPPC membranes.

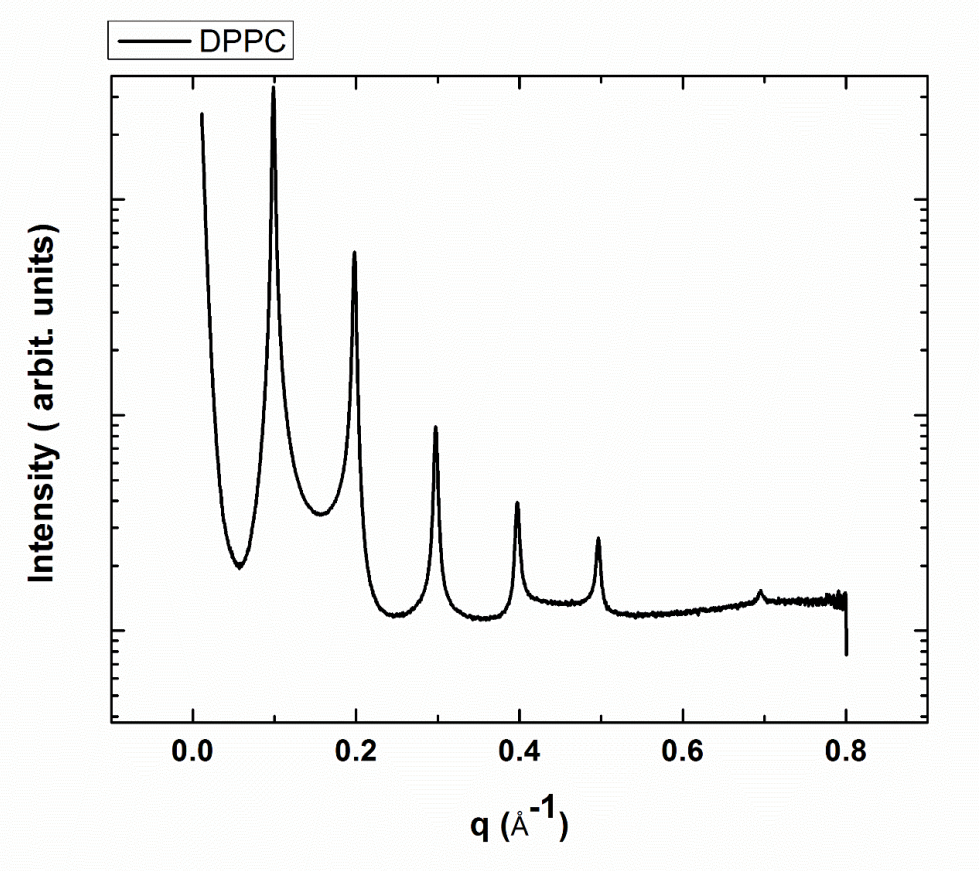

Figure 2.7 SAXS data collected represented as q vs. intensity plot of DPPC membrane with 0.5 mol% α-tocopherol.

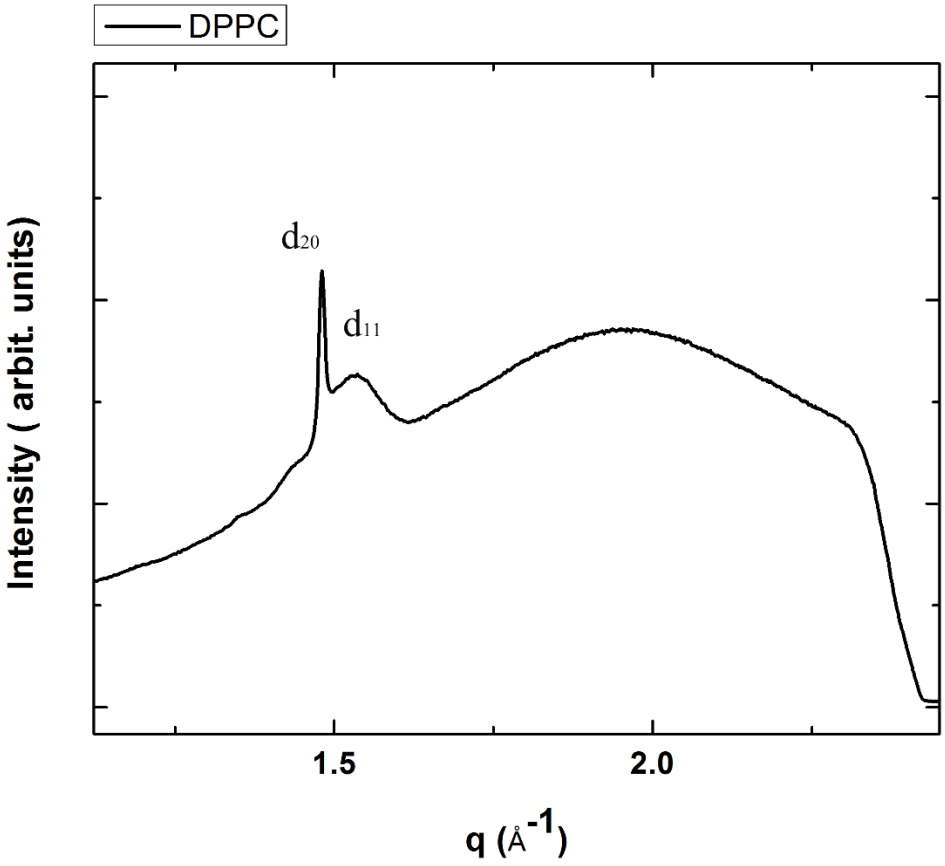

Figure 2.8 WAXS data represented as q vs. intensity plot of DPPC membrane with 0.5 mol% α-tocopherol.

2.3.4 Phase Determination from Data

Powder diffraction through synchrotron x-ray produces ring pattern that represent the spacing between bilayers and molecules depending on the technique used, either SAXS or WAXS. In SAXS, detection of phase separation is possible because bilayers of different phase have different d-spacing corresponding to the bilayer thickness. Observation of two or more first order peaks determines phase coexistence. Determination of which peak corresponds to which phase is done by the number of orders and sharpness of the peak. $L_{\beta'}$ phase membrane have long range order thus resulting in more than 2 orders and sharper. Due to the capture range of the detector, 6 peaks are typically observed, shown in Figure 2.7. As for L_{α} phase, only 2 orders are detected because of the short range ordering, shown in Figure 2.9. The peaks of L_{α} phase are broader than $L_{\beta'}$ phase peaks due to the fluctuation of the bilayers. SAXS is collected at lower *q*s, while WAXS was collected at higher *q*s. For WAXS, the analyzed peak represent the chain packing between the lipid molecules.

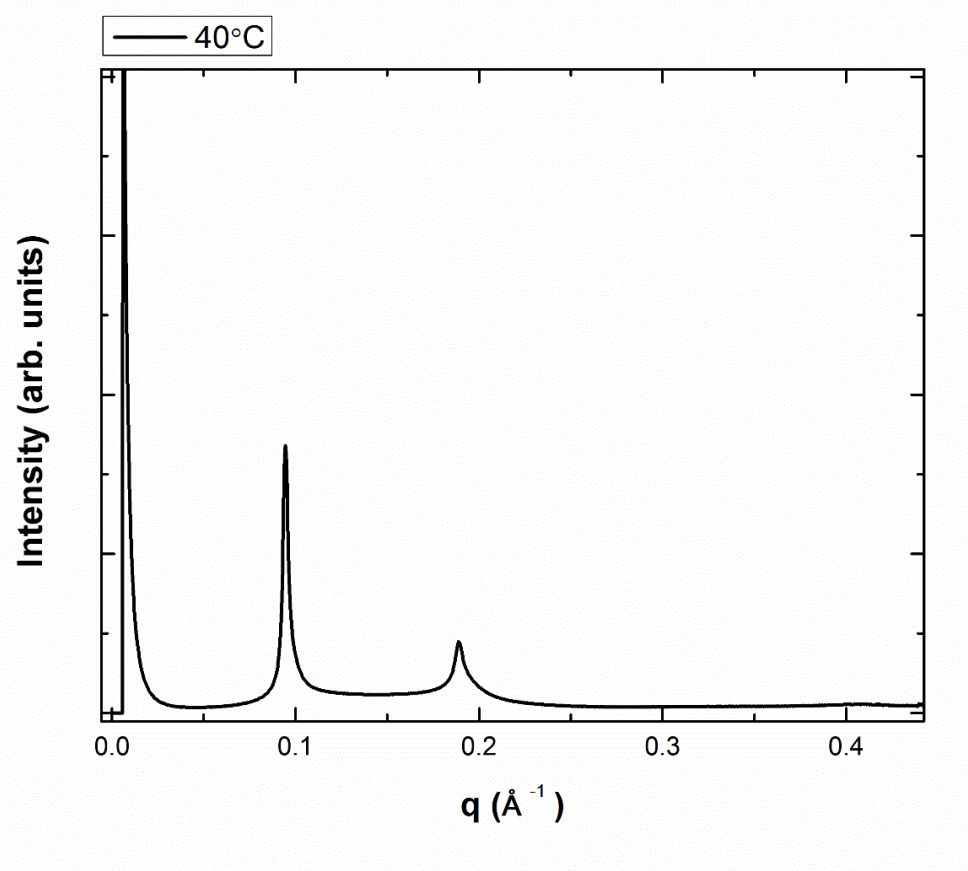

Figure 2.9 SAXS data of membrane in L_α phase for mixture 0.25 mol% DHA-PE/99.75 mol% DPPC at 40°C.

2.3.5 Electron Density Profile

The d-spacings calculated from the q-values contain both spacing of the bilayer region and water region. To determine the distance of these regions, we reconstructed the electron density profile (EDP) of the d-spacing along the z axis [2]. It is expected that the hydrophilic head group are more densely packed than the hydrophobic tails since the tails can take several conformations and mobile. We saw in equation 5 that the structure factor is a Fourier transform of the electron density of the material being scattered. The electron density term, p(r), is in Eq. 5 so in order to reconstruct the EDP, we just need to do the inverse of Eq. 5 as a function in term of z, the direction normal to the bilayer, leading to

$$p(z) = \sum \pm F(h)\, cos(\frac{2\pi hz}{d}) \qquad \text{(Eq. 10)}$$

where $F(h)$ is the structure factor, h is the order parameter, and d is the layer spacing. For lamellar structure, the phase sign of the diffraction is (-,-,+,-). In analyzing the

powder diffraction pattern we generated a plot of q vs intensity. To work in reverse from the plot, we have to use information from the graph. The structure factor

$$F(h) = h\sqrt{I(h)} \qquad \text{(Eq. 11)}$$

where $I(h)$ is the area of the intensity of each peak representing the layer spacing. Inputting the values into equation 10 generates a wave function representing the electron density along the z axis. Figure 2.10 is an example of the electron density profile of gel phase as electron density vs z. The unit of the electron density is arbitrary. It is expected that the hydrophilic region is denser than the hydrophobic region because the fatty acid tails can have many conformations. Reconstruction using more orders provide more accurate information of the distance of each sublayer such as the hydrophobic region and hydrophilic region. In comparing the EDP generated from 3 orders and 4 orders, the bilayer thickness increases by a few nanometers.

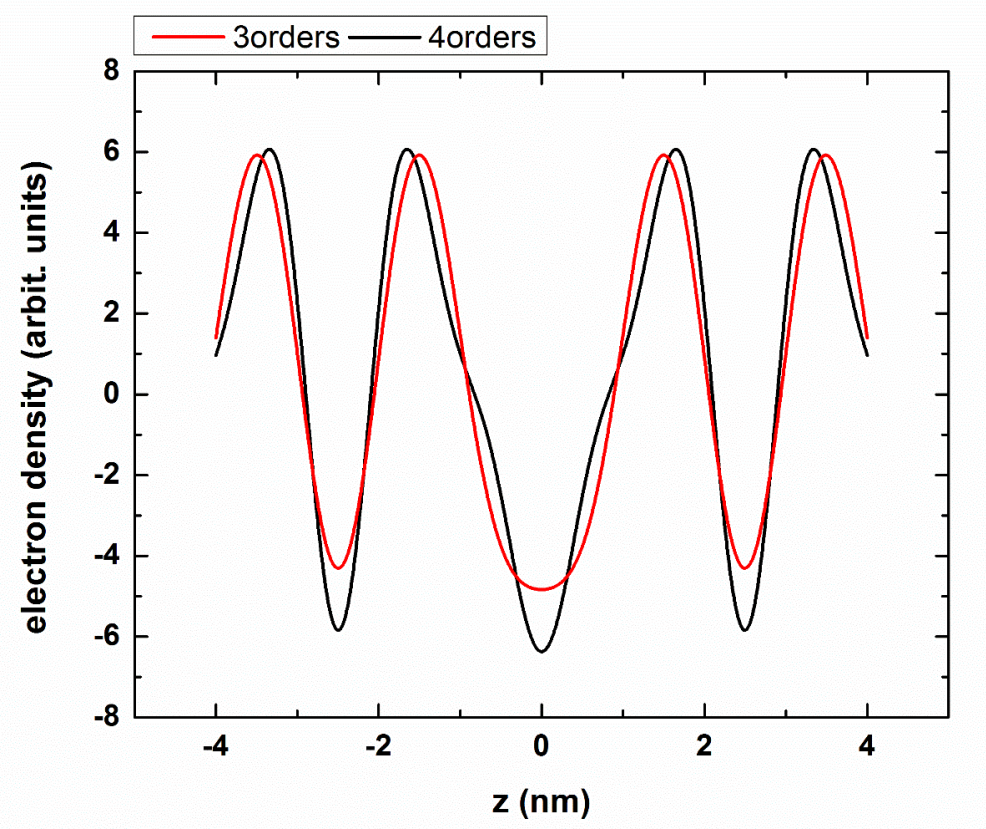

Figure 2.10 EDP of $L_{\beta'}$ phase generated from 3 orders and 4 orders from SAXS data for binary mixture 0.25 mol% DHA-PE/99.75 mol% DPPC.

2.4 Lipid Deformation

The lipid membrane is a flexible soft material that can be bend and stretch. In Chapter 1, we briefly mention the two different elastic modulus of the membrane, k_a and k_b. Lipid membranes of tighter packing, like gel phase, have higher modulus compared to liquid disorder phase. In this section, we will discuss the bending modulus kb and associate force to deformation. A point deformation of the bilayer where the force applied is perpendicular to the membrane will push the membrane outward forming a tube. The free energy cost of bending a flexible sheet is defined by the Helfrich formula

$$E_{bend} = \frac{k_b}{2}(H - c_o)^2 + \kappa K \qquad \text{(Eq. 12)}$$

where k_b is the membrane bending modulus, H is the Mean curvature = $(1/R1 + 1/R2)/2$, κ is the saddle splay modulus and K is the Gaussian curvature $(1/(R1R2))$. In the extraction of tube from the bilayer, there is no saddle splay modulus; therefore, k, the last term, is omitted. Moreover, the spontaneous curvature term is omitted because the bilayer is a natural flat membrane with 0 curvature on the scale of few microns. If we assume a tubule of radius, r and length L being extracted from a vesicle using the Helfrich formula assuming no increase in membrane surface area A and volume V [3, 4]. The free energy, F, for bending the membrane is defined as

$$F = \frac{k_b}{2}(2H)^2\, dA + \sigma A - \rho V - fL \qquad \text{(Eq. 13)}$$

where σ is the surface tension, ρ is pressure. In tethered GUVs, the energy of surface tension (minimizing the surface area) acts against the energetic costs of bending, pressure induced volume increase, and tube elongation to minimize the total free energy. Without the action of deformation forces, the bilayer takes the shape of a spherical vesicle. In the formation of the nanotube, the pressure inside the GUV and tube remain zero, otherwise it would rupture. In order to find the force and radius of the tube, we calculate ∂F/∂R =0 and ∂F/∂L =0 at the equilibrium state thus arriving at

$$r = k_b 2\sigma\,, f = 2\pi 2\sigma k_b \qquad \text{(Eq. 14)}$$

Substitution of the first equation into the second one in terms of r, f, and k_b, we get the relation of

$$f = \frac{2\pi k_b}{r} \qquad \text{(Eq. 15)}$$

By this relation, the r and f are inverse proportional, the higher the f the smaller the generated radius will be.

2.5 Giant Unilamellar Vesicles

Giant unilamellar vesicles (GUVs) are excellent for studying phase behavior and lipid membrane structures. The GUVs are formed through a method called electroformation. It utilizes a house-made device known as an electroformation chamber, shown in Figure 2.11. The chamber consists of two conductive ITO glass slides and one Teflon o-ring between the slides, similar to a sandwich, creating a volume space about 1 ml. Each of the slides are connected to a function generator via copper clamps on the glasses. To form GUVs, lipids are dried onto the conductive side of the glass slides. The slides sandwich the Teflon o-ring with the interior volume filled with aqueous solution. One slide is connected to a positive terminal and the other to a negative terminal of the function generator. The whole setup, electroformation chamber and function generator, is placed inside an incubator set to temperatures above the transition temperature of both lipids. An alternating current (AC) is applied to the chamber. GUVs are formed through budding of the bilayer into the medium. The warm temperature of the incubator rehydrates the dried lipid and self-assembles it into bilayers at the surface of both glass surfaces. The applied electric field between the two glass slides causes the bilayer to fluctuate and bud the bilayer off the surface. Bilayers that are free from the surface reconstruct into vesicles floating inside the medium due to minimizing the free energy. The size of the GUVs can be controlled by the frequency and power applied by the function generator. This technique can produce GUVs with diameters between 1-100 μm.

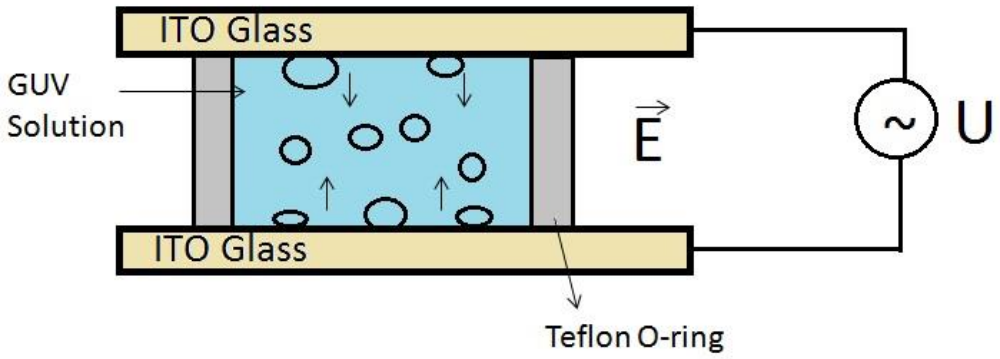

Figure 2.11 Schematic of GUV electroformation chamber.

2.6 Flow Cell

Lipid nanotube generation was carried out in a flow cell, which consists of a glass cover slip taped to a microscope glass slide with double sided tape, shown in Figure 2.12. The microscope glass slide and glass cover slip were cleaned by soaking each in acetone followed by ethanol. They were then heated in the oven to dry off the solution. The covered slip is then plasma cleaned for 5 minutes using a plasma cleaner. The cover slips are then soaked in a polylysine adhesive solution for 12 minutes. The adhesive layer helps the microtubules to bind to the glass surface. The adhesives solution consists of 300 ml of ethanol and the 850 μl of polylysine solution. Afterward, the cover slips were placed in the oven to dry off the ethanol. The flow cell was assembled by placing two strips of double sided tape about 3 mm apart on the microscope glass slide and then placing the cover slip on top of the tape. This creates a channel that is about 12 μl.

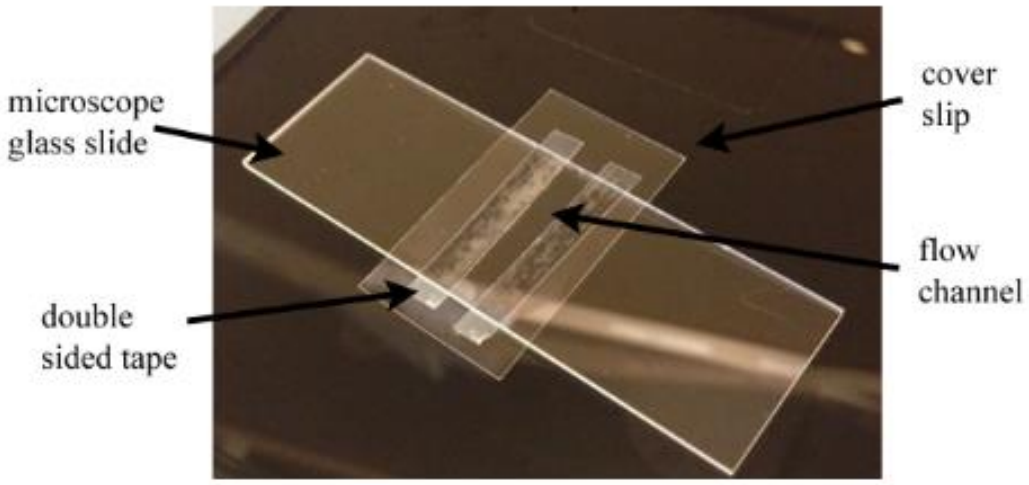

Figure 2.12 Flow cell made of glass slide and glass cover slip.

2.7 Conclusion

The theory of x-ray scattering from electron and regular structures were both explained in this chapter. Solid matters are ideal materials for x-ray scattering experiments due to their periodic packing structure compared to soft matter. However, the structure of soft matters like lipid can still be characterized by an x-ray scattering technique as long as it is in an anisotropic state. The theory of scattering from the dense structures of lipid membrane stacks was introduced in this chapter along with the analysis and interpretation of the corresponding data. This characterization technique was the main tool for investigating the structure of an interesting lipid mixture, which will be presented in Chapter 3.

The theory of elasticity of lipid membrane for the formation of cylindrical tubes from vesicles was introduced in Section 2.4. In Chapter 4, we will present a study on lipid nanotube formation using an anchored system to extract nanotubes from vesicles via flow. The last two sections in this chapter presented the method to form GUVs for nanotube extraction and the setup of the device used in the experiment. More details will be introduced in Chapter 4 regarding the specific method of lipid nanotube formation.

1. Bragg, W.H. and Bragg, W. L. "The Reflexion of X-rays by Crystals". Proc R. Soc. Lond. A **1913,** 88 (605): 428–38
2. Quinn, P.J.; Wolf, C. Hydrocarbon chains dominate coupling and phase coexistence in bilayers of natural phosphatidylcholines and sphingomyelin. *Biochi. et Biophy. Acta*. **2009** 1788, 1126-1137.
3. Deuling, H.J. and Helfrich, W. Red blood cell shapes as explained on the basis of curvature elasticity. *Biophys. J.* **1976**, 16, 861-868
4. Derenyi, I.; Julicher, F.; Prost, J. Formation and interaction of membrane tubes. *Phys. Rev. Lett.* **2002,** 88, 238101.

Chapter 3

X-ray Scattering Study of DHA-PE/DPPC Mixtur

3.1 Introduction

In this chapter, an x-ray scattering study on the phase behavior of binary lipid mixtures of DHA-PE and DPPC at low concentrations below 5.0 mol% DHA-PE is presented. DHA is specifically the polyunsaturated fatty acid segment of the lipid molecule, which consists of 6 C-C double bonds. It is a fascinating component to the lipid molecule that has gained much interest in the fields of research, medicine, and diet. For this dissertation, we will refer the term DHA as the whole lipid molecule. The motivation for this project was because DHA had clinically been shown to have beneficial health outcomes but the physical role and interaction in cell membranes are still largely unexplored. The cell membrane is very complex with many different components. Therefore, we started with a binary lipid model consisting of saturated (DPPC) and unsaturated (DHA-PE) lipids to investigate the role of DHA. X-ray scattering is a suitable tool for characterizing the structure of lipid membrane because it can be tuned to study nano structure. Our results showed that DHA-PE induced phase separation into a DHA rich (L_{α} phase) and a DHA poor ($L_{\beta'}$ phase) at overall DHA-PE concentrations as low as 0.1 mol%. In addition, we found the $L_{\beta'}$ phase with a decrease in bilayer thickness of 1.34 nm for 0.1 mol% at room temperature compared to pure DPPC bilayers. This result was contrary to that seen in similar studies on mono-unsaturated lipids where an increase in bilayer thickness was observed. There are limitation to this technique, which we cannot paint a true image of the lipid membrane structure. However, a discussion of possible causes to the decreased bilayer thickness will be address.

3.2 Background

3.2.1 Health Benefits of DHA

Since early epidemiological studies of the Eskimo diet linked docosahexaenoic acid (DHA) content [1] to cardiac health, polyunsaturated fatty acids have attracted a great deal of attention in the physiological, nutritional and biomedical communities. Numerous studies have drawn links between the high dietary DHA content of diets rich in fish oil to beneficial effects on cardiovascular disease [2], various cancers [3, 4], arthritis [5], depression [6], Alzheimer's disease [7], its role in infant development [8, 9], and in retinal cell function [10]. Claims focused on the dietary benefits polyunsaturated fatty acids have led to a rapid expansion in the incorporation of DHA in the human diet from the beginning of infancy to senior adults. Studies have also shown that excessive intake of DHA can be dangerous, for example, in postnatal growth retardation [11]. Despite intense interest in these ubiquitous molecules there is a significant gap in our knowledge of the physiological effects of DHA and other polyunsaturated lipids in the diet and our current understanding of its specific biomolecular importance.

3.2.2 DHA in Biological Membrane

Certain classes of biological cells contain high concentrations of polyunsaturated lipids in the membrane. For example, DHA is particularly enriched in the synapses of neural membranes [12] and in the rod-cell outer segment in the retina [13]. In these special cases, the amount of DHA present can approach almost 50 mol% of the total membrane fatty acids and di-DHA phospholipids are present [14, 15]; in which both phospholipid chains on the same molecule have the characteristic 22:6 (ω3) DHA composition (alkyl chains 22 carbons long with 6 unsaturated bonds). DHA levels in other biological membranes can vary and are typically about 5%, although this content may be enriched by changes in diet [16]. In membranes altered by dietary DHA, it is possible that di-DHA phospholipids exist in significant amounts and account for the reported DHA-induced alterations in membrane function.

3.2.3 Recent Model Studies of DHA Mixture

Despite the fact that there have been recent studies on DHA lipids in ternary bilayers, not much has been done with a binary system [17-21], an important starting point to gain a basic understanding of how DHA lipids interact with saturated lipids. This article presents a detailed look at the low concentration regime of DHA-PE in the DHA-PE/DPPC binary system using x-ray diffraction. DHA's interaction with other lipids in model systems was previously studied at relatively high concentrations by Stillwell and Wassall [21-23]. In these studies, phase separation was indicated in mixtures of DHA and sphingomyelin at 10 mol% DHA-lipid using differential scanning calorimetry [22]. In another binary mixture of just cholesterol and DHA-lipid, it was shown that cholesterol has a very low solubility in DHA because of highly disordered chain packing in the system [23]. In the combined ternary mixture of DHA-lipid, cholesterol, and sphingomyelin, they also found that cholesterol has a greater affinity for the more rigid sphingomyelin causing the separation of the membrane into a DHA-rich/chol-poor and chol-rich/DHA-poor domains [21].

3.2.4 Lipid Peroxidation

In general, DHA is a challenging lipid molecule to work with due to its high susceptibility to peroxidation. DHA has a total of 6 double bonds that lie in between methylene bridges, therefore the hydrogens in the fatty acid chain are very reactive. Free radicals in the environment can strip these hydrogens from the lipid thus turning that particular region into a radical itself until it becomes stable. The end products of lipid peroxidation as malondialdehyde [24]. There are several methods that can reduce or prevent oxidation of lipids such as the use of antioxidants, limiting light, and an oxygen free environment. Antioxidants such as α-tocopherol (vitamin E) can inhibit the oxidation process because it actively scavenges for reactive oxygen species. In measuring the rate of lipid peroxidation, the thiobarbituric acid assay (TBA) is commonly used. TBA reacts with malondialdehyde to produce thiobarbituric acid reactive species (TBARS), which can be detected by spectroscopy. The TBA assay has been used in many research studies

to measure lipid oxidation in cells [25, 26]. One drawback of this technique is that it is not only specific to lipid as there are other methods to form malondialdehyde. However, in our research, it is sufficient because our mixtures contain only lipids.

3.3 Motivation

It is clear that DHA is a biologically important fatty acid present in all of our cells and this molecule can have a significant impact on both special and general cell functions. However, there is definitely a threshold for the consumption of DHA before it starts triggering negative health effects. Therefore, it is important to find this happy medium in order to control one's health. Fundamental research into the physical interactions between DHA containing lipids and the other lipids in the cell membrane however is still needed, particularly in relation to phase separation effects and their relevance to lipid domain formation. In this work we focus on the lower concentration limit of DHA-PE membrane content and the effects of this molecule on membrane phase behavior in this regime.

3.4 Experimental

3.4.1 Materials

1-dipalmitoyl-2-docosahexaenoyl-*sn*-glycero-3-phosphoethanolamine (DHA-PE) and 1,2-dipalmitoyl-*sn*-glycero-3-phosphocholine (DPPC) were obtained from Avanti Polar Lipids in chloroform and used without further purification. DPPC was stored under -20°C in chloroform and DHA-PE was stored in the -80°C freezer until ready to use. α-tocopherol was purchased from Sigma-Aldrich and prepared as a stock solution of 1 mM in chloroform and stored in freezer at -20°C. Figure 3.1 shows molecular structures for the lipids used in this study. TBA was purchased from Sigma Aldrich and came in powder form. Stock solution of TBA in chloroform was prepared at 10 g/L in Milli-pore water and stored in the refrigerator at 4°C.

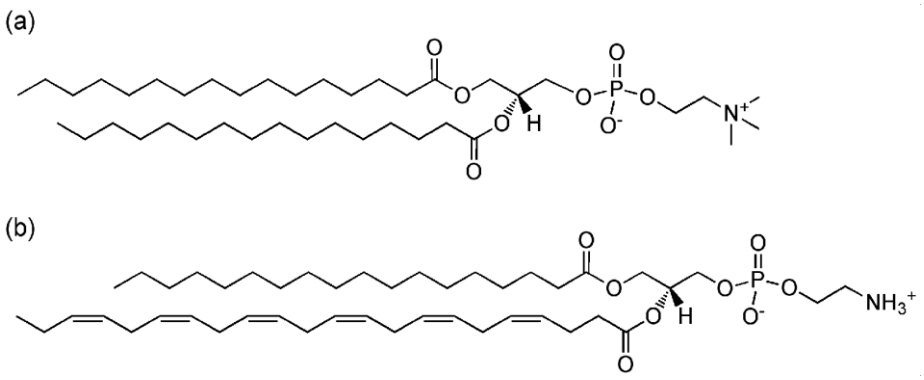

Figure 3.1 Molecular structures for the lipids used in this study, (a) DPPC (b) DHA-PE.

3.4.2 TBA Assay

α-tocopherol was used as an antioxidant to prevent oxidation of DHA-PE. We used a TBA assay to measure the degree of malondialdehyde produced from lipid peroxidation [27]. Concentrations of 0.5 mol%, 1.0 mol%, and 2.0 mol% α-tocopherol were added to 1 mM DHA-PE in chloroform against a control of no α-tocopherol. The mixtures were dried by nitrogen and vacuum dried for 2 hours. The dried lipids were rehydrated with Millipore water back to final concentration of 1mM and vortex. TBA comes in powder form and were dissolved in Millipore water to a concentration of 10g/L. TBA was added to the lipid solutions at a mole ratio 1:9 of DHA-PE to TBA and incubated at 45°C to generate TBARs. We used a higher concentration of TBA to lipid because there are 6 double bonds per DHA-PE. We used the Nanodrop spectrometer from Taso's lab to measure the absorbance of TBARs at 532 nm. The Nanodrop provides fast readout with little volume needed, which is important for oxidation measurement because long exposure to oxygen and light progress more oxidation.

3.4.3 Sample Preparation Lamellar Phase Structure

To prepare multilamellar vesicles for SAXS experiments, DHA-PE and DPPC were mixed by mol% in chloroform with 0.5 mol% α-tocopherol to a final lipid concentration of 25 mM. The mixtures were then dried with high purity nitrogen and vacuum dried for 2 hours to further remove any excess chloroform. Samples were then rehydrated with Millipore water back to 25 mM and incubated at 45°C from 1-10 minutes to release the lipid from the vial's glass wall. The samples were vigorously vortexed to ensure that the lipids were well dispersed with a milky white appearance. The milky white appearance is a visual indicator of multilamellar vesicles. To prepare x-ray samples, about 50 µl of lipid solutions are pipetted into 1.5 mm glass capillaries and centrifuged at low speed for 5-10 minutes to produce pellets in the fully hydrated lamellar phase. Furthermore, the capillaries were sealed with silicone rubber sealant immediately after filling to prevent any evaporation of the water and limit exposure to oxygen. Because DHA is highly

susceptible to lipid oxidation, sample preparations were carried out rapidly under limited light conditions and under high purity nitrogen. Capillaries were then stored at 4°C until the x-ray measurements were carried out.

3.4.4 X-ray Scattering Procedure

SAXS measurements were carried out at the Stanford Synchrotron Radiation Lightsource (SSRL) beamline 4-2 at the Stanford Linear Accelerator Center (SLAC). The whole x-ray beam setup is inside a shield unit called a hutch. We used a wavelength of 1.127 Å (11 keV) with a 1.7 m and 0.2 m distance from sample to detector for SAXS and WAXS experiments respectively. Powder diffraction patterns were recorded on a CCD detector (Rayonix MX225-HE) using a 1s exposure time. For instrument calibration, we used silver behenate (d_{001} = 58.83Å) with a sensitivity of 1 Å. The aluminum temperature chamber was mounted first into the beam pathway between the beam output and the detector. Capillaries were mounted into the chamber in sets of 4-6 capillaries. Using this apparatus, the interior chamber temperature was controlled to an accuracy of ± 0.25 K by passing water through tubes into the chamber. Thermistors were mounted close to the sample to monitor the temperature. Data collection for each temperature was obtained after 5 minutes upon reaching the desired temperature because we wanted the sample to be in equilibrium and stable temperature. After collecting powder diffraction patterns using a CCD camera, SasTool software at the beamline was used for radial integration (producing plots of scattered intensity as a function of scattering vector, **q**). Origin Lab was used for peak finding and further analysis. Refer to chapter 2 for detailed description of the analysis and interpretation method.

3.5 Results

3.5.1 Lipid Oxidation

The DHA molecule is susceptible to oxidation because of its weak double bonds. Figure 3.2 presents the absorbance of TBARs collected at 532 nm using the Nanodrop spectrometer. The purpose of this experiment was to show how effective α-tocopherol prevents the oxidation of DHA-PE. We conducted the experiment with three low concentrations with incubation time up to 2 hours. Low concentrations were used because it minimize significant effect to the lipid membrane mixture. The data presented here only showed up to 30 minutes of incubation time because it was initially the amount of time we used for rehydration of the dried lipids. Most recent data of this project utilized at max 10 minutes for rehydration because some samples dissolved better. Vigorous vortex at room temperature also help reduce the time of incubation. According to the figure, all concentrations of α-tocopherol prevented DHA-PE oxidation equally throughout the 30 minutes. From the result of this experiment, we decided to use a constant concentration of 0.5 mol% of α-tocopherol in all of the lipid mixtures for x-ray scattering experiments. This experiment had a mole ratio of 1:199 (α-tocopherol/ DHA-PE) and it effectively prevented lipid oxidation.

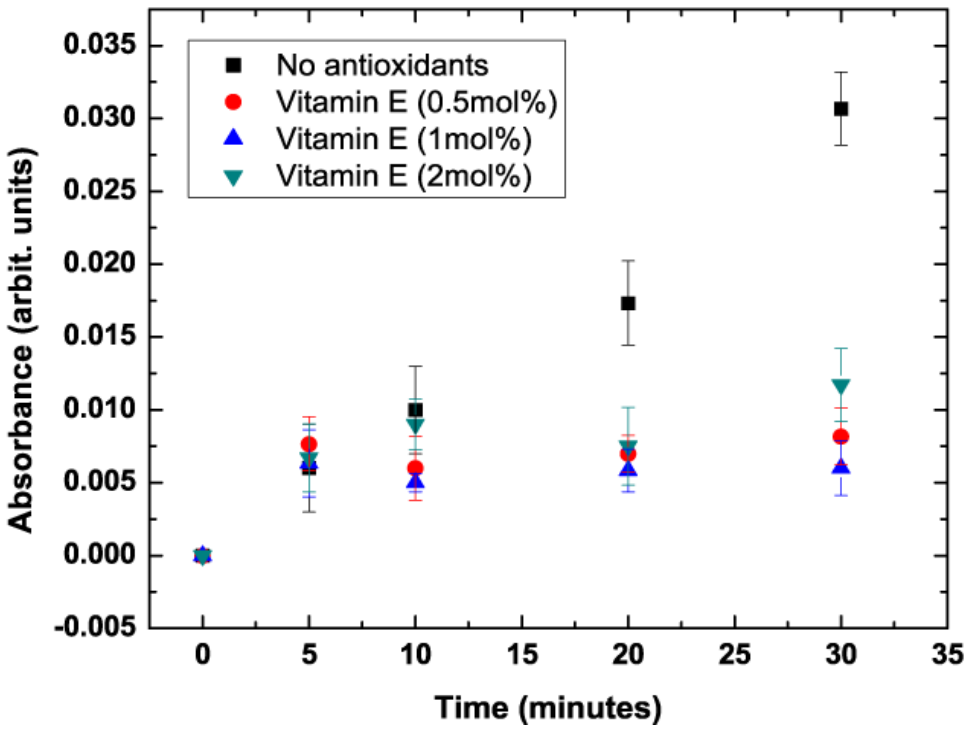

Figure 3.2 Time vs Absorbance plot of TBARS collected using a Nanodrop spectrometer. TBARS was used to quantify DHA-PE oxidation for concentrations at 0.5 mol%, 1 mol%, and 2 mol% of α-tocopherol to prevent oxidation.

3.5.2 Beam Damage on Lipids

In working with DHA-PE, we want to verify that the lipids sealed in the capillaries did not undergo any molecular damage due to the x-ray beam exposure, sample heating, or time. To control for these external factors, data was collected when the thermal chamber reached the desired temperature and 30 minutes afterward. Data collection at each temperature occurred within 1-1.5 hours because it took longer for the chamber to stabilize at higher temperatures. In Figure 3.3, the data at 40°C was collected approximately 12 hours after data collection at 20°C. The sample clearly went into the fluid phase at 40°C and then the sample was allowed to cool back to room temperature. After roughly 48 hours, we recollected data for the same sample and found the result to be identical to the previous data at room temperature. These test experiments confirmed that the sealed lipids did not undergo any detectable molecular modifications in our experiments due to beam damage, heating, or with time time.

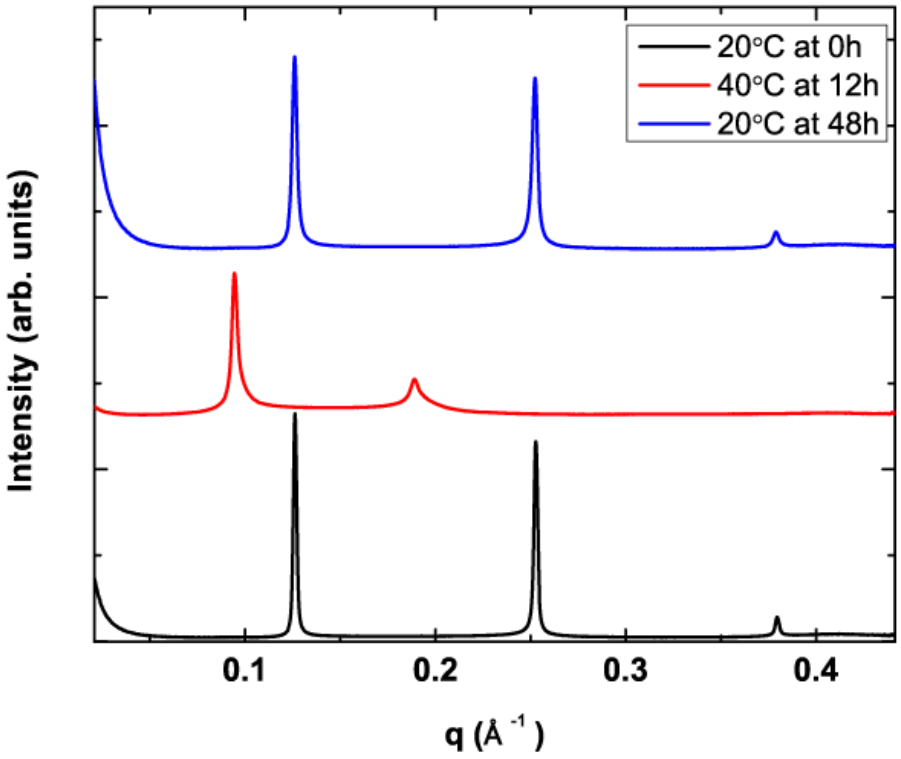

Figure 3.3 q vs intensity plot of binary mixture DHA-PE/DPPC at 0.1 mol% DHA-PE. Sample was heated to L_α phase and cooled back to $L_{\beta'}$.

3.5.3 SAXS Plot

For the control, SAXS data were collected for pure DPPC with 0.5 mol% α-tocopherol at 16ºC, shown in Figure 2.7. Pure DPPC has long range ordering, which is represented by multiple orders of peaks up to 6 orders. The plots show both linear and log scale of the intensity axis because it is harder to identify the 6th order in linear plot. Lipid mixtures were prepared at different DPPC/DHA-PE ratios with 0.5 mol% α-tocopherol and SAXS data collected as a function of temperature. Figure 3.4 shows an example of x-ray scattering data for 0.1 mol% DHA-PE with increasing temperature. The data was plotted as scattered intensity as a function of scattering vector, **q,** and Bragg peaks corresponding to the scattering from stacks of bilayers can be seen. At lower temperatures, the $L_{\beta'}$ phase is clearly present, with 3 orders of diffraction shown from the lamellar stack at $q = 2\pi/d$, $4\pi/d$, and $6\pi/d$. The $L_{\beta'}$ phase in lipid membranes typically produce up to 6 orders of diffractions or more because of its long-range inter-bilayer ordering, but here only 3 orders are shown as the detector was positioned to collect data up to $q_{max} = 0.45$ Å^{-1}. This q range is sufficient to clearly differentiate the $L_{\beta'}$ phase from the L_α phase. Based on this x-ray evidence, we can unambiguously distinguish between the $L_{\beta'}$ phase and the L_α phase in our system. Owing to distinct differences between the $L_{\beta'}$ phase and L_α phase in

lipid mixtures in terms of molecular ordering, we previously demonstrated the use of SAXS to distinguish between scattering patterns for each of these phases and to confirm two and three-phase coexistence in ternary lipid mixtures. This was done by observing distinct sets of Bragg peaks differing in peak width and in the number of orders present [28]. In the case where bilayers exhibit phase separation, similar domains tend to stack together. This fact is evident both from the success of the technique itself (randomly arranged domains in the stack would not produce two sets of Bragg peaks) but was also confirmed independently by fluorescence microscopy on membrane stacks [29].

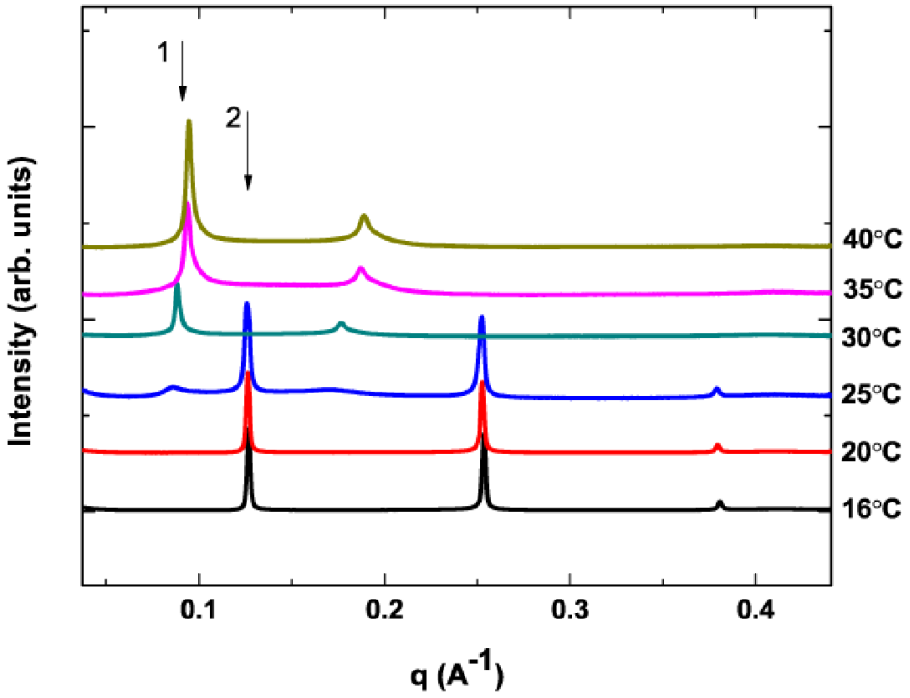

Figure 3.4 Transmission solution SAXS data for mixture of DPPC/DHA-PE at DHA-PE 0.10 mol%. At 25°C, phase coexistence can be observed as two sets of Bragg peaks are present. The first order peaks for each phase are indicated by arrow 1 (L_α phase) and arrow 2 ($L_{\beta'}$ phase).

In Figure 3.4 at 0.1 mol% DHA-PE, the first order peak from the $L_{\beta'}$ phase was seen at **q** = 0.126 $Å^{-1}$ corresponding to a bilayer spacing of d = 4.99 nm. As the temperature was increased to 25°C, we observed the emergence of a second peak at **q** = 0.897 $Å^{-1}$ corresponding to d = 7.00 nm. This peak can be assigned to a stack of membranes in the L_α phase. Unlike the $L_{\beta'}$ phase, the L_α phase only produces 2 orders of diffraction at **q** = 0.897 $Å^{-1}$ and **q** = 0.178 $Å^{-1}$. This scattering signature, more characteristic of short range ordering in the bilayer stack, is expected due to increased thermal membrane fluctuations

in the more fluid L_α phase. The two peaks indicated by the arrows at 25°C are indicative of phase coexistence in the sample. Above 30°C, the $L_{\beta'}$ phase completely disappear as the membrane became homogeneous at T_m. We can also note at this point that the L_α phase had a bilayer d-spacing approximately 2 nm larger than that of the $L_{\beta'}$ phase. The d-spacing of the L_α phase gradually decreased with increasing temperature to d = 6.65 nm at 40°C. Such behavior is expected as increased thermal motion of the lipid tails results in an increase in the lateral distance between neighboring molecules and therefore a decrease in bilayer thickness [30, 31].

3.5.4 WAXS Plot

WAXS data were collected at the same beamline following the SAXS experiments for pure DPPC membranes (Fig. 2.8) and binary membranes (Fig. 3.5) with 0.5 mol% α-tocopherol. WAXS data also contain SAXS information as well due to the wide range from q values between 0 and 1.6. However, this mode is more sensitive to higher q values. The plots shown in the following exclude the low q values as they are not of interest in this mode. For pure DPPC membranes, WAXS data were collected at higher q values of q = 1.486 $Å^{-1}$ (d = 4.228 Å), which represented the d_{20} peak, shown in Figure 2.8. The broad peak next to the d_{20} peak is the d_{11} peak. The sharp peak of d_{20} represents the chain packing order of the lipid molecules. When the membrane was heated to above the transition temperature, the peaks disappeared. Therefore, scattering of any membrane in liquid disordered phase using WAXS mode is unnecessary. Since WAXS captures the spacing between molecules of the lipid bilayers, it also captures the spacing between water molecules, which was shown in the broad peak at q = 1.95 $Å^{-1}$. Before fitting the d_{20} peak, scattering from water was subtracted from the data.

Figure 3.5 shows the gel phase from the WAXS data of binary mixture with 0.1 mol% DHA-PE and 99.9 mol% DPPC. For this mixture, the d_{20} peak is present but not the d_{11} peak. The plot showed two temperatures for the same sample at 20ºC and 35ºC, which represented the $L_{\beta'}$ phase and the fluid phase when the peak disappeared. The d_{20} peak is at q = 1.537 $Å^{-1}$ corresponding to a d-spacing of 4.086 Å. According to the data, incorporation of the DHA-PE lipid into the DPPC $L_{\beta'}$ phase decreased the chain packing. Further analysis of this data will be discuss later in the chapter.

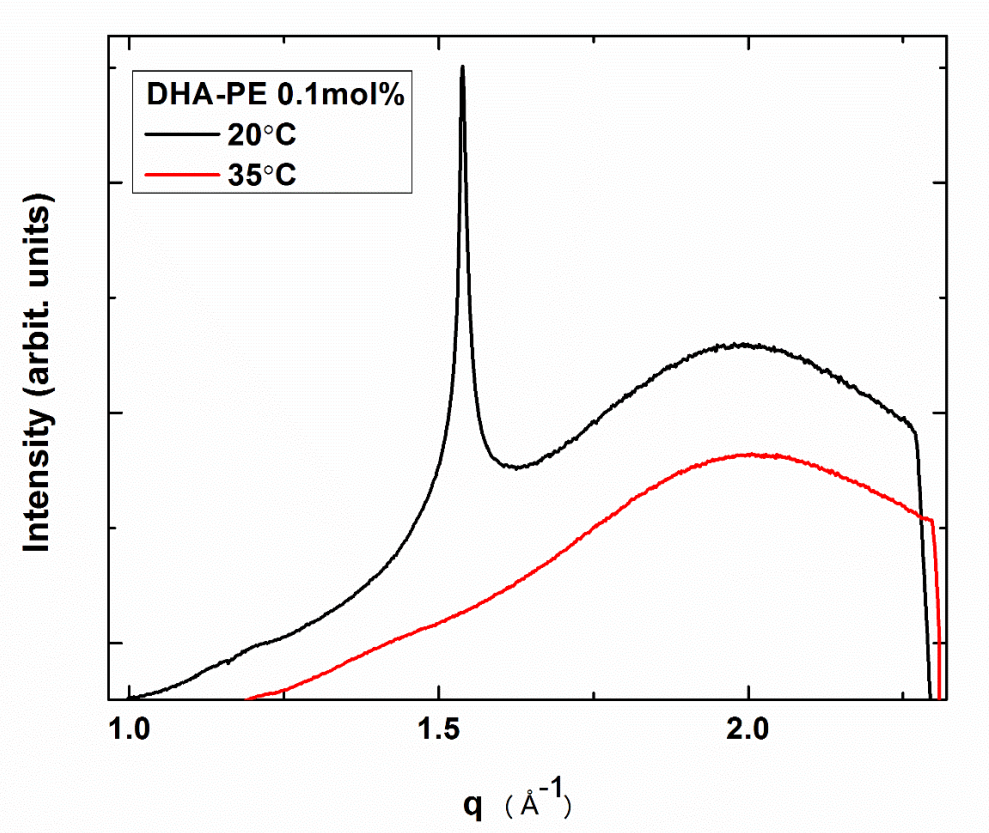

Figure 3.5 q vs intensity plot for WAXS data of binary mixture 0.1 mol% DHA-PE/99.99 mol% DPPC.

3.5.5 Phase Diagram

Figure 3.6 shows a phase diagram in which we mapped out the regions of $L_{\beta'}$, L_{α}, and phase coexistence from 16°C to 43°C using the above described x-ray analysis. 16°C was the lowest achievable temperature for our experimental setup using chilled water to cool the aluminum chamber. The system can be heated reliably to 45°C, but beyond this point it was difficult to maintain a stable temperature due to heat dissipation. Another limitation to temperature accuracy came from the size of the scattering window across the chamber, a significant source of heat loss. As a result, we estimated the temperature at the sample to be accurate to ± 2°C. Future experimental work will involve an improved design for this chamber. From the data set in Figure 3.6, we observed some key points. Firstly, a full membrane in the gel phase is only present at lower temperatures with less than 0.2 mol% DHA-PE. We also noticed that the phase boundaries with added DHA-PE were a function of both composition and temperature. Above 1 mol% DHA-PE the miscibility temperature (T_m) does appear to increase with added DHA-PE. At the concentrations shown in the figure, the phase coexistence region spans approximately 7°C before transitioning completely into the fluid phase at T_m. In the 0 mol% case (Pure DPPC), scattering characteristic of the ripple phase was also observed with the expected

temperature range [32]. However, evidence of the ripple phase was not seen in any of the other mixtures, although it is possible that it may be present with a narrow temperature range and thus not detected in our experiment.

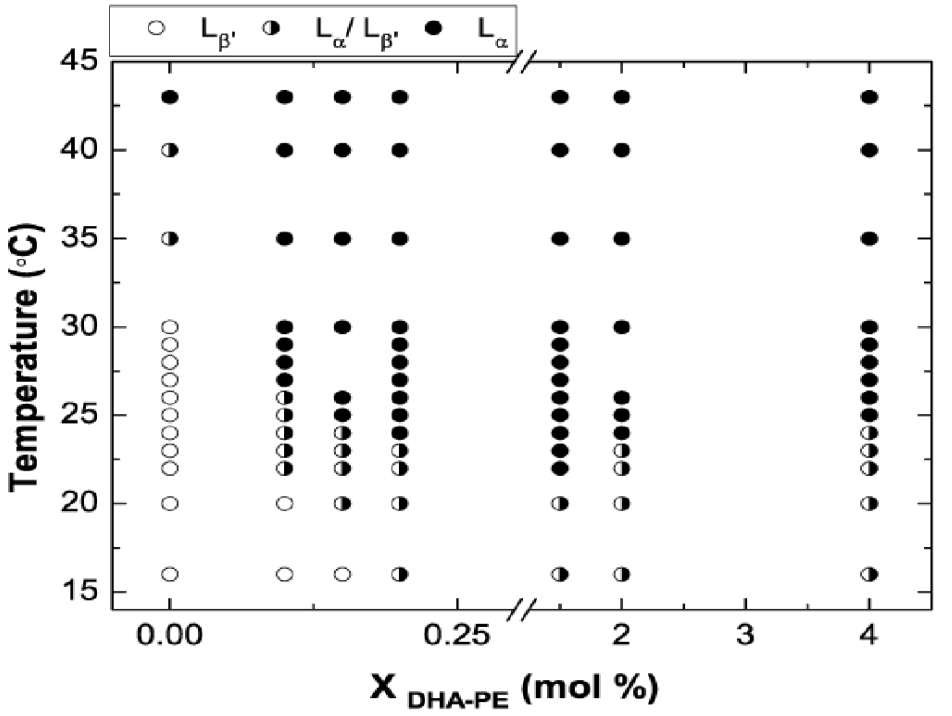

Figure 3.6 Binary phase diagram of DPPC/DHA-PE at low DHA-PE concentrations as determined by SAXS.

3.5.6 Electron Density Profile

From our SAXS data, it was possible to reconstruct electron density profiles and analyze the structure of the bilayer in more detail for the L_α and $L_{\beta'}$ phases. We used this method primarily to obtain an estimate for the average distance between lipid head groups in the two leaflets (d_{pp}) and to calculate the average thickness of the water layer (d_w) for both phases, where d_w is the difference between the complete d-spacing and d_{pp}. Our calculations followed Quinn and Wolf's [33] method to create the electron density distribution graph as a function of thickness (z) for our data, shown in Figure 3.7. In the bilayer, the phosphate head groups are expected to have the highest electron density due to close packing. The region where the hydrocarbon chains meet (z = 0 nm) are expected to have the lowest density. Using this technique, we looked at the electron density profiles of both the $L_{\beta'}$ and the L_α phase coexisting in domain stacks within the bilayer stacks that make up the sample [28, 29]. From our analysis, we obtained a d_{pp} thickness of 3.03 ± 0.06 nm using the 3 Bragg orders collected in the $L_{\beta'}$ phase at 0.1 mol% and 20°C.

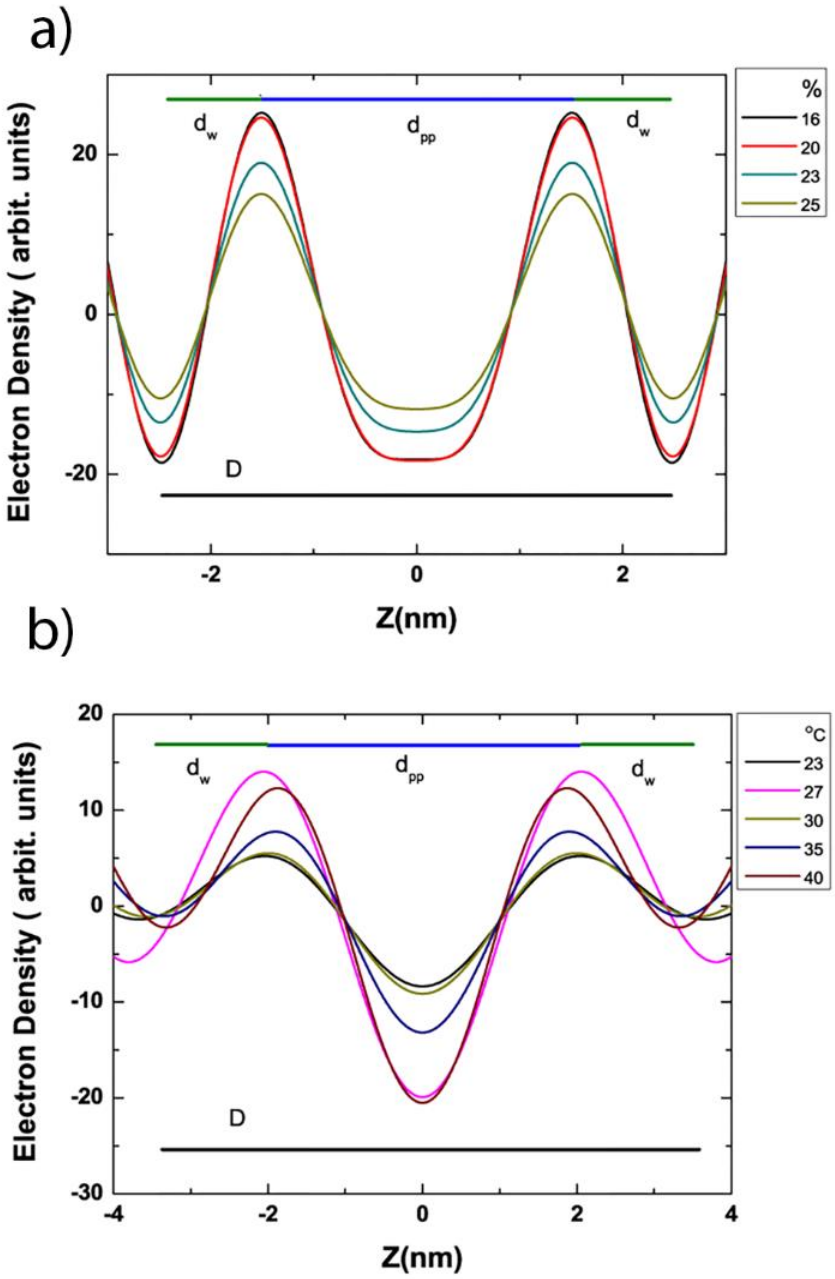

Figure 3.7 Electron density profiles for the coexisting (a) $L_{\beta'}$ and (b) L_{α} phase at 0.1 mol% DHA-PE at different temperatures. The center of the bilayer is at Z = 0 nm.

In general this calculation should be performed using 4 or more orders of diffractions and after a careful analysis of EDP reconstruction comparing the use of 3 orders of diffractions with 4 and 5 orders in one mixture, we found that our measurement of d_{pp} had a 10% systematic error While it was clear that performing the calculation using more orders of diffractions provides a more accurate estimation of the structure, unfortunately this was not possible because the q_{max} for most of our data was too low. To account for this error, we corrected our data accordingly to give an adjusted d_{pp} of 3.33 ± 0.06 nm. Using this method we obtained a water layer of d_w = 1.66 ± 0.06 nm for the $L_{\beta'}$ phase fraction in 0.1 mol% DHA-PE membranes, as shown in Figure 3.7(a).

The water layer from this analysis was quite close to the 1.83 nm water layer for pure DPPC $L_{\beta'}$ phase in excess water from Torbet and Wiklins [34]. For the L_α phase fraction at 0.1 mol% DHA-PE, we calculated the d_{pp} and d_w to be 3.96 ± 0.05 nm and 3.35 ± 0.05 nm respectively. In the calculation for the liquid disordered phase, only 2 orders of diffractions were present, as were characteristics of the short range ordering in this phase, therefore no correction to the EDP data was needed. Figure 3.7(b) shows that the volume occupied by the headgroup peak in the L_α phase is very broad, not as sharp as the $L_{\beta'}$ phase, and this was an indication that the phase exhibited high fluctuations. In other words, our calculation of the thickness of the water layer in the L_α phase was an approximation, since the region was less well defined compared to that of the $L_{\beta'}$ phase. EDP analysis were able to make two key conclusions, firstly that the water layer, d_w, associated with membranes in the $L_{\beta'}$ phase for the mixtures we studied does not change significantly when compared to the expected value for pure DPPC and therefore subsequently that any differences we observe in bilayer d-spacings in this phase are a result of differences in d_{pp}, the membrane thickness.

3.5.7 D-spacing Plots

From our SAXS data taken across a range of lipid mixtures, we plotted two graphs: bilayer d-spacing vs. temperature and d-spacing vs. concentration for both the $L_{\beta'}$ and the L_α phases (Fig. 3.8). In the temperature plot (Fig. 3.8a), phase co-existence is denoted by the presence of both open and solid symbols of the same shape for each concentration shown. As we saw in Figure 3.6, even at low temperatures the higher concentrations exhibit phase separation, due to the presence of DHA. Note also that the square symbol for 0 mol% (pure DPPC) do not change significantly as a function of temperature. The $L_{\beta'}$ phase completely disappears at 30°C for all the concentrations that include some DHA-PE. From looking at the data, we see the dependence of the $L_{\beta'}$ phase d-spacing on temperature (open symbols). This small increase of approximately 0.05 nm was likely due to the increased thermal fluctuations in the membrane when increasing temperature.

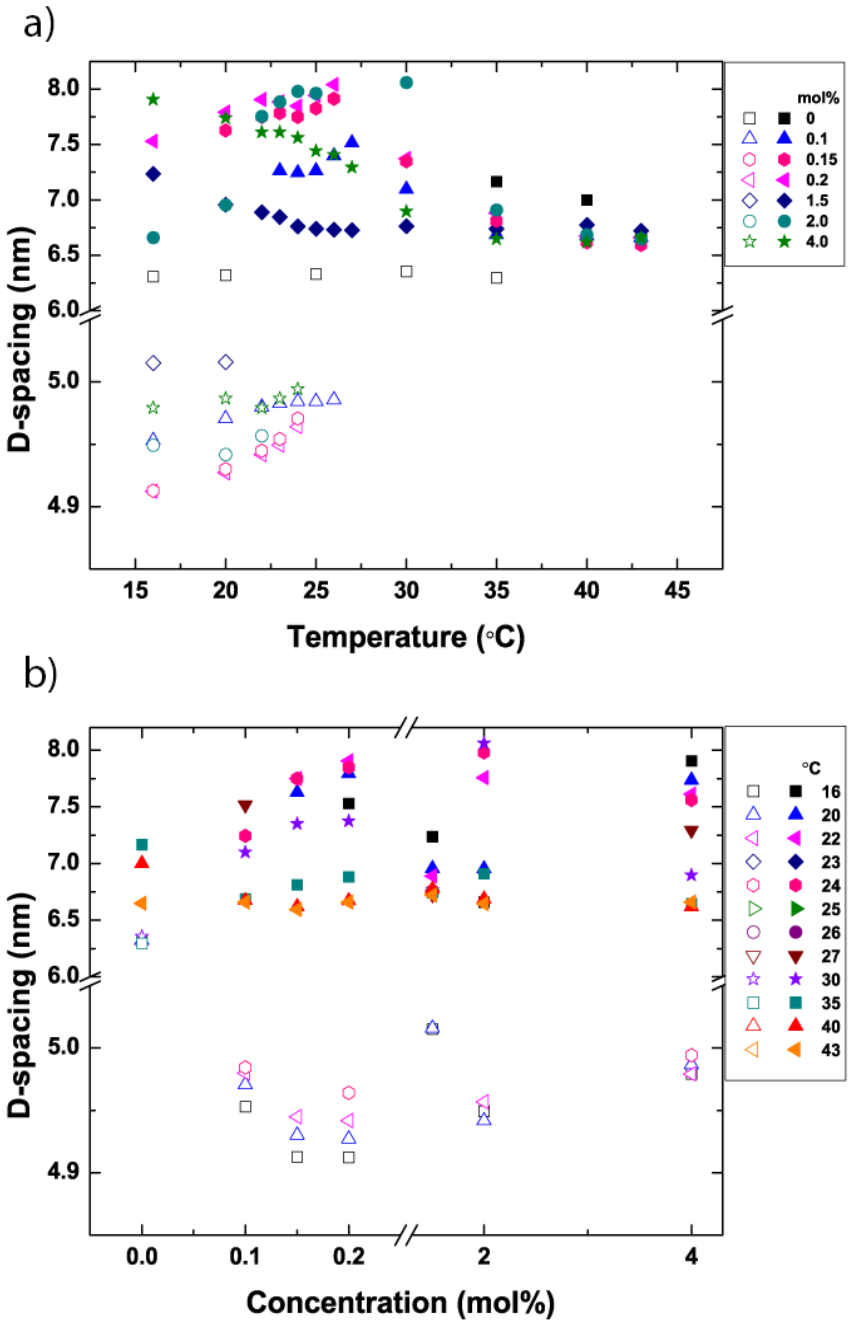

Figure 3.8 Lamellar d-spacing in the $L_{\beta'}$ (open symbols) and L_{α} (solid symbols) phases as a function of (a) temperature (for different DHA concentrations) and (b) DHA concentration (at different temperatures). Where the two phases coexist both open and solid symbols are present at the same temperature or concentration.

The membranes all exhibit homogeneous L_α phase (solid symbols) at 30°C and above. As the temperature increases, the d-spacing of the L_α phase decreases slightly. This effect can be explained thermally. Heating causes an increase in the average lateral area occupied by each molecule, providing a larger volume for the highly flexible DHA chain to occupy and allowing for a slightly thinner bilayer. In Figure 3.8b, we use the same data set to plot d-spacing for both phases as a function of DHA-PE concentration. Results for different temperatures are shown using different symbols. From this plot we can more easily observe that an increase in the concentration of DHA-PE doesn't have a significant effect on the d-spacing of either phase when phase separated at fixed temperature.

At the very low concentration of 0.1mol% DHA-PE, we were able to observe phase separation into $L_{\beta'}$ and L_α phases at room temperature (22°C). Pure DPPC membranes have a T_m at 43°C and at room temperature exhibit the tilted $L_{\beta'}$ phase with a d-spacing of 6.4 nm [35]. Our results demonstrate that the addition of a very small amount of DHA-lipid to the system as a whole decreases the bilayer spacing of this phase fraction dramatically, despite the fact that we expect most of the DHA-PE molecules to partition into the L_α phase. Previous studies of binary systems that also include DPPC such as, DPPC/DOPC [36] and DPPC/cholesterol [35, 37] have shown that the tilt of the $L_{\beta'}$ phase reduces to 0° on addition of different lipids accompanied by a decrease in membrane rigidity (Fig. 3.8b). These effects cause the bilayer thickness in the $L_{\beta'}$ phase to increase. We initially assumed that the DHA molecule would perform the same way as cholesterol and DOPC by reducing membrane rigidity due to its high degree of unsaturation. However, instead of increasing the thickness of the $L_{\beta'}$ phase, we observed that membrane thickness in the $L_{\beta'}$ phase was decreased a significant amount from that measured in pure DPPC $L_{\beta'}$ phase, both at low temperatures where a single $L_{\beta'}$ phase is present and also in the phase separated state.

3.5.8 WAXS

To confirm the role of increased molecular tilt on bilayer thickness, WAXS was also carried out at SLAC and plotted in Figure 3.9. Due to the significant change in the gel phase d-spacing from SAXS measurements, we expected that the lateral packing of the lipids would also change. For pure DPPC bilayer at 20°C, we observed both the d_{20} and the d_{11} peak. The peak d_{20} is at $q = 1.486$ Å^{-1} ($d = 4.228$ Å) corresponding to the in-plane chain packing of the lipids. This result is in agreement with the WAXS peak of gel phase from Nagle [38]. WAXS was carried out for DHA-PE concentrations from 0.25-2.50 mol% across a range of temperatures (16°C-35°C). At 20°C, we obtained a q value of $q = 1.576 \pm 0.002$ Å^{-1} ($d = 3.972 \pm 0.005$ Å) for concentrations of 0.25-0.75 mol%. For 1.00-2.50 mol%, the q value dropped to $q = 1.537 \pm 0.002$ Å^{-1} ($d = 4.086 \pm 0.005$ Å). We plotted the concentration of DHA-PE vs. d-spacing of the d_{20} peak (Fig. 3.9). At all DHA-PE concentrations measured in this WAXS experiment, we observed that the chain packing of the gel phase containing DHA-PE molecules are more closely packed than for pure DPPC membrane. This results is in good agreement with our proposed model of increased tilt shown in Figure 3.10c. When the samples were heated to the fluid phase at above 30°C, the characteristic WAXS $L_{\beta'}$ peak disappeared.

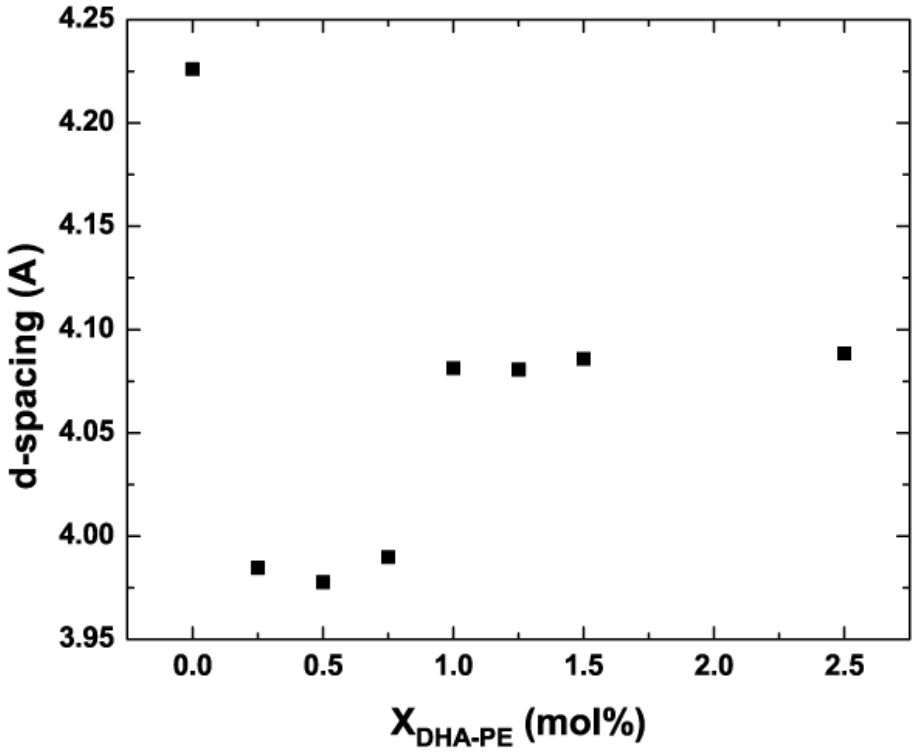

Figure 3.9 Concentration vs d-spacing plot of WAXS analysis of DHA-PE/DPPC.

3.6 Discussion

Increasing the tilt angle of lipid molecules is one possible way to cause a decrease in thickness but there are few other possibilities. A bilayer can be interdigitated, where the hydrophobic region becomes denser and hydrocarbon chains between opposing monolayer pack next to each other [39]. Also, interdigitated membranes have typically only been observed in bilayers of saturated lipids because unsaturated lipids statistically have many conformations, reducing the probability of interdigitation. Most interdigitated membranes are achieved through molecular modification, solvent selection or applying an external force [39]. Based on this evidence we assume that interdigitation can play only a small role here.

3.6.1 Tilt Geometry

To explain the dramatic change in d-spacing, we proposed that instead of the DHA molecules reducing the rigidity of the $L_{\beta'}$ phase, the molecule actually acts to increase the tilt angle of the $L_{\beta'}$ phase. There are two possible scenarios that can potentially explain this phenomenon. In the first, DHA has a long hydrocarbon chain of 22 carbons compared to the 16 carbons of DPPC. The 22 carbon chain may be stretched out within the $L_{\beta'}$ phase geometry because its freedom is being restricted by the DPPC rigid environment. The stretched unsaturated chain will cause the gap between the two leaflets to increase, therefore, the surrounding lipids will have to increase their tilt angle in order to reduce the gap and avoid a vacuum. In the second scenario, The DHA lipids are not extended. Due to the high number of possible configurations for DHA, on average filling out a volume space like a cone, steric interactions increase the tilt of the $L_{\beta'}$ phase (Fig. 3.10c). Entropically this second case is the most likely since the DHA-lipid chain is not extended and there are many possible fatty acid conformations in this geometry. Moreover, it is possible that the interaction of DHA-PE can induce a cross-tilted gel phase causing the bilayer to be thinner as shown for the gel phase of DPPE in a molecular dynamics simulation by Leekumjorn [40]. As mentioned above, the tilt angle of the gel phase is reduced to 0° when either cholesterol or DOPC is incorporated as shown by Schmidt [40] and Kamarker [20, 43]. The $L_{\beta'}$ phase in our system exhibits a dramatic bilayer thickness reduction from 6.28nm in fully hydrated pure DPPC to 4.99 nm with 0.1 mol % DHA-PE at 22°C for example. We suggest that DHA-PE changes the bilayer thickness by increasing the tilt of the $L_{\beta'}$ phase. For a fully hydrated DPPC bilayer of d-spacing at 6.4 nm with a 1.83 nm water layer, the tilt angle is expected to be 32.6° as calculated by Katsaras [41]. By extrapolation, using our decreased d-spacing of 4.99 nm, d_{pp} = 3.33 nm and d_w = 1.66 nm, the new tilt angle would need to be 50.85° for a pure DPPC $L_{\beta'}$ phase. This simple calculation assumes using a pure DPPC $L_{\beta'}$ phase because the concentration of DHA-PE in the gel phase is very low. Such a high tilt angle in the membrane is unlikely and therefore we can expect other factors to play a role in the reduction in d-spacing.

3.6.2 Water Layer

Another possible explanation for the observed decrease in d-spacing thickness is a substantial decrease in the water layer between the stacked $L_{\beta'}$ membranes. We initially postulated that the water layer of the $L_{\beta'}$ phase with DHA-PE could have a dramatic water layer decrease due to the presence of DHA-PE. However, from our EDP analysis, we find that the change in the water later is particularly significant, with a difference of just 0.13 nm from a pure DPPC $L_{\beta'}$ phase to $L_{\beta'}$ phase with DHA-PE. This EDP analysis suggests that thickness changes in the bilayer (d_{pp} decreases by 1.15 nm) have a significant effect on bilayer thickness.

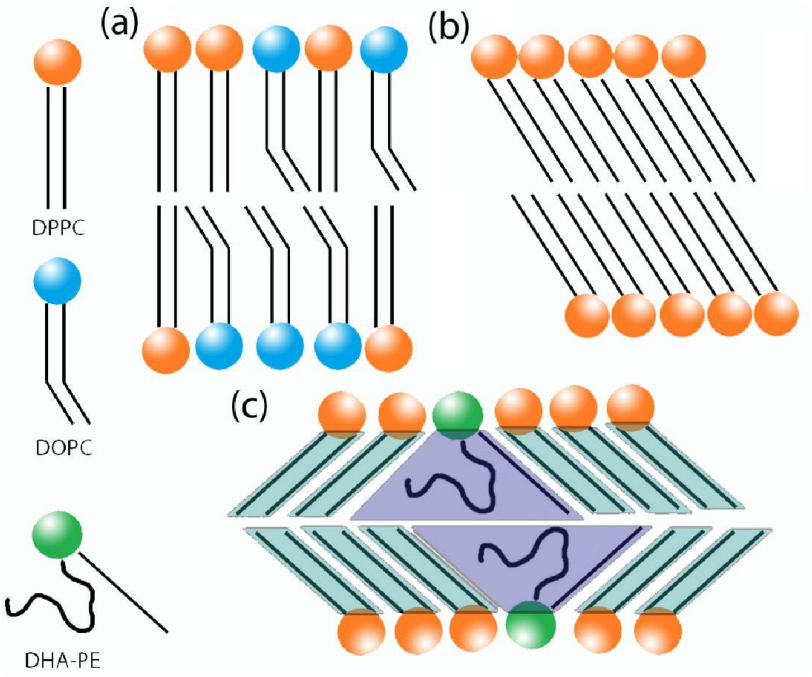

Figure 3.10 Schematic of the $L_{\beta'}$ phase in pure (a) DPPC/DOPC, (b) DPPC, and (c) DPPC/DHA-PE bilayers. DHA may locally induce increased tilt in the gel phase domains.

3.6.3 α-tocopherol

One important discussion point concerns the presence of α-tocopherol in our systems - this might be suggested as the cause of the decreased bilayer thickness in the gel phase. The gel phase is not completely free of DHA-PE in that there is a small amount present in each phase, thus resulting in a decreased transition temperature. NMR studies have shown that α-tocopherol prefers to localize close to DHA-PE in a symbiotic pair feeding on reactive oxygen species while protecting the lipid from oxidation [42]. α-tocopherol molecules that localize around the DHA-PE in the gel phase are expected to have no effect on the bilayer thickness. It was shown by Kamal et al. that α-tocopherol does fluidize the DPPC gel phase and change the transition temperature but this temperature, but this effect is only seen at much higher concentrations than those in our study. In addition, they observed no significant change in bilayer thickness even at high concentrations of α-tocopherol [43]. We had carried out a control experiment with 0.5

mol% of α-tocopherol in DPPC membrane and observed no difference from pure DPPC membrane which was plotted in Figure 3.6 and 3.8. At 0.5 mol% of α-tocopherol, there is no effect on the bilayer thickness and T_m.

3.6.4 Oxidized DHA

A second important discussion point is the effect of oxidized DHA-PE on the gel phase. A recent model from Wallgren on oxidized lipids in the membrane suggested that the oxidized acyl chain caused disruption of the lipid molecules surrounding it by extending the *sn-2* chain towards the polar head group or into the water region. This effect can increase the chain packing density, as seen in our WAXS data [44-46]. It is possible that this could be the cause of our observations, considering that we use easily oxidized lipids, however, we have taken measures to prevent oxidation. Nonetheless, it we find it a very interesting result that such small amounts of DHA-PE at 0.1mol% can have a huge effect on the gel phase bilayer thickness.

3.7 Conclusion

The effects of DHA-PE on the $L_{\beta'}$ phase are clear evidence that there is some small volume of DHA-lipid in the $L_{\beta'}$ phase and that this fraction modifies the membrane structure significantly or that the effects of DHA molecules surrounding these domains are able to modify the domain bilayer structure. We have focused on a DHA lipid containing one DHA fatty acid in the *sn-2* position, while we still have a saturated tail in the *sn-1* position. With only one tail that is highly unsaturated, we can assume that if we were to have a mixture of a lipid consisting of two DHA tails (di-DHA), even more dramatic differences in phase behavior may result. Such studies will be the subject of future work and may reveal interesting results related to the role of di-DHA in biological membranes.

In this project, we investigated the phase behavior of a DHA-lipid with DPPC in the low concentration regime. Remarkably, DHA-lipid concentrations as low as 0.1 mol% induced phase coexistence of the $L_{\beta'}$ and L_{α} phases and a lower concentration bound to this phase separated region in the phase diagram was not found. The effect of DHA on chain packing in the $L_{\beta'}$ was also unexpected and possible evidence for a dramatic increase in lipid tilt. This tilt effect can be explained by geometrical arguments although other factors clearly must play a contributing role. DHA-lipids are extremely prevalent in biological systems however their interactions with membrane lipids, in the dynamic cell are not well understood. Fundamental work on reduced systems such as we present here can help us to gain a better understanding of the biological role of these important molecules.

1. Bang, H. O.; Dyerberg, J.; Hjoorne, N. The composition of food consumed by greenland eskimos. *Acta Med Scand.* **1976,** 200, 69-73.
2. McLennan, P.; Howe, P.; Abeywardena, M.; Muggli, R.; Raederstorff, D.; Mano, M.; Rayner, T.; Head, R. The cardiovascular protective role of docosahexaenoic acid. *Eur. J. Pharm.* **1996,** 300, 83-89.
3. K.K. Carroll, K.K. Dietary fats and cancer. *Am. J. Clin. Nutr.* **1991**, 53, 1064S-1067S.
4. Zerouga, M.; Stillwell, W.; Stone, J.; Powner, A.; Jenski, L.J. Phospholipid class as a determinant in docosahexaenoic acid's effect on tumor cell viability. *Anitcancer Res.* **1996**, 16, 2863-2868.
5. Kremer, J.M.; Lawrence, D.A.; Jubiz, W.; DiGiacomo, R.; Rynes, R.; Bartholomew, L.E.; Sherman, M. Dietary fish oil and olive oil supplementation in patients with rheumatoid-arthritis-clinical and immunological effects. *Arthritis Rheum*. **1990**, 33, 810-820.
6. Hibbeln, J.R.; Salem, N. Dietary polyunsaturated fatty-acids and depression - when cholesterol does not satisfy. *Am. J. Clin. Nutr.* **1995**, 62, 1-9.
7. Itua, I.; Naderali, E.K. Omega-3 and memory function: to eat or not to eat. *Am. J. Alzh. Dis. Other. Dem.* **2010**, 25, 479-482. [8] International Society for the Study of Fatty Acids and Lipids (ISSFAL) Board Statement: recommendations for the essential fatty acid requirement for infant formulas. *J. Amer. Coll. Nutr.* **1995**, 14, 213-214.
8. International Society for the Study of Fatty Acids and Lipids (ISSFAL) Board Statement: recommendations for the essential fatty acid requirement for infant formulas. *J. Amer. Coll. Nutr.* **1995**, 14, 213-214.
9. Salem, N.J.; Kim, H.Y.; Yergey, J.A.; in A.P. Simonpoulos, R.R. Kifer, R.E. martin (Eds.), *Omega-3 Fatty acids in growth and development,* Academic Press, New York, **1986**, pp. 319-351.
10. Vanmeter, A.R.; Ehringer, W.D.; Stillwell, W.; Blumenthal, E.; Jenski, L.J. Aged lymphocyte-proliferation following incorporation and retention of dietary omega-3-fatty acids. *Mechan. Ageing and Dev*. **1994**, 75, 95-114.
11. Church, M.W.; Jen, K.L.C.; Jackson, D.A.; Adams, B.R.; Hotra, J.W. Abnormal neurological responses in young adult offspring caused by excess omega-3 fatty acid (fish oil) consumption by the mother during pregnancy and lactation. *Neuro. and Terat.* **2009**, 31, 26-33.
12. Innis, S.M. *Essential fatty acid metabolism during early development*. In: Biology of Metabolism in Growing Animals. Burrin DG ed. Pub. Elsevier Science, B.V. Amsterdam **2005**. Part III, pp. 235-74.
13. Martin, R.E.; Elliott, M.H.; Brush, R.S.; Anderson, R.E. Detailed characterization of the lipid composition of detergent-resistant membranes from photoreceptor rod outer segment membranes. *Inv. Opthalmology and Visual Sci.* **2005**, 46, 1147-1154.
14. Miljanich, G.P.; Sklar, L.A.; White, D.L.; Dratz, E.A. Disaturated and dipolyunsaturated phospholipids in the bovine retinal rod outer segment disk membrane. *Biochemic et Biophysica Acta,* **1979**, 552, 294-306.

15. Bell, M.V.; Dick, J.R.; Buda, C. Molecular speciation of fish sperm phospholipids: Large amounts of dipolyunsaturated phosphatidylserine *Lipids* **1997**, 32, 1085-1091.
16. Robinson, D.R.; Xu, L.; Tateno, S.; Guo, M.; Colvin, R.B. Suppression of autoimmune-disease by dietary n-3 fatty-acids. *Jour. Lipid Research.* **1993,** 34, 1435-1444.
17. Wassall, S.R.; Stillwell, W. Docosahexaenoic acid domains: the ultimate non-raft membrane domain. *Chem. and Physi. of Lipids.* **2008,** 153, 57-63.
18. Soni, S.; LoCascio, D.S.; Liu, Y.; Williams, J.A.; Bittman, R.; Stillwell, W. ; Wassall, S.R.; Docosahexaenoic acid enchances segregation of lipids between raft and nonraft domains: H-2-NMR study. *Biophy. Jour.* **2008,** 95, 203-214.
19. Williams, J.A.; Batten, S.E.; Harris, M.; Rockett, B.D.; Shaikh, S.R. ; Stillwell, W.; Wassall, S.R. Docosahexaenoic and eicosapentaenoic acids segregate differently between raft and nonraft domains. *Biophy. Jour.* **2012,** 103, 228-237.
20. Shaikh, S.R.; Dumaual, A.C.; Castillo, A.; LoCascio, D.; Siddiqui, R.A.; Stillwell, W.; Wassall, S.R. Oleic and docosahexaenoic acid differentially phase separate from lipid raft molecules: a comparative NMR, DSC, AFM, and detergent extraction study. *Biophy. Jour.* **2004,** 87, 1752-1766.
21. Wassall, S.R.; Shaikh, S.R.; Brzustowicz, M.R.; Cherezov, V.; Siddiqui, R.A.; Caffrey, M.; Stillwell, W. Interaction of polyunsaturated fatty acids with cholesterol: a role in lipid raft phase separation. *Macromol Symp*. **2005**, 219, 73-83.
22. Shaikh, S.R.; LoCascio, D.S.; Soni, S.P.; Wassall, S.R.; Stillwell, W. Oleic and docosahexaenoic acid containing phosphatidylethanolamines differentially phase separate from sphingomyelin. *Biochim. Biophys. Acta*. **2009**, 1788, 2421-2426.
23. Shaikh, S.R.; Cherezov, V.; Caffrey, M.; Soni, S.P.; LoCascio, D.S.; Stillwell, W.; Wassall, S.R. Molecular organization of cholesterol in unsaturated phosphatidylethanolamines: X-ray diffraction and solid state H-2 NMR reveal difference with phosphotidylcholines. *J. Am. Chem. Soc.* **2006**, 128, 5375-5383.
24. Niki, E.; Yoshida, Y.; Saito, Y.; Noguchi, N. Lipid peroxidation: Mechanisms, inhibition, and biological effects. *Biochem. And Biophys. Research Comm.* **2005**, 338, 668-676.
25. Song, J.H.; Fujimoto, K,; Miyazawa, T. Polyunsaturated (n-3) Fatty acids susceptible to peroxidation are increased in plasma and tissue lipids of fats fed docosahexaenoic acid-containing oils. *J. Nutr*. **2000**, 130, 3028-3033.
26. Garcia, Y.J.; Rodriguez-Malaver, A.J.; Penaloza, N. Lipid peroxidation measurement by thiobarbituric acid assay in rat cerebellar slices. *J. Neuro. Methods.* **2005**, 144, 127-135.
27. Rael, L.T.; Thomas, G.W.; Craun, M.L.; Curtis, C.G.; Bar-Or, R.; Bar-Or, D. Lipid peroxidation and the thiobarbituric acid assay: Standardization of the assay when using saturated and unsaturated fatty acids. *Journal of Biochemsitry and Molecular Biology*. **2004**, 37, 749-752.
28. Yuan, J.; Kiss, A.; Pramudya, Y.H.; Nguyen, L.T.; Hirst, L.S. Solution synchrotron x-ray diffraction reveals structural details of lipid domains in ternary mixtures. *Phys. Rev. E* **2009,** 79, 031924.

29. Tayebi, L.; Ma, Y.; Vashaee, D.; Chen, G.; Sinha, S.K.; Parikh, A.N. Long-range interlayer alignment of intralayer domains in stacked lipid bilayers. *Nature Mater.* **2012,** 12, 1074-1080.
30. Small, D.M. Lateral chain packing in lipids and membranes. *Jour. Lipid Research*. **1984**, 25, 1490-1500.
31. Garcia-Manyes, S.; Oncins, G.; Sans, F. Effect of temperature on the nanomechanics of lipid bilayers studied by force spectroscopy. *Biophy. Jour.* **2005**, 89, 4261-4274.
32. Cevc, G.; Marsh, D. *Phospholipid bilayers. Physical Principles and Models*. Wiley-Interscience, New York **1987.**
33. Quinn, P.J.; Wolf, C. Hydrocarbon chains dominate coupling and phase coexistence in bilayers of natural phosphatidylcholines and sphingomyelin. *Biochi. et Biophy. Acta*. **2009** 1788, 1126-1137.
34. Torbet, J.; Wiklins, M.H.F. X-ray diffraction studies of lecithin bilayers. *J. Theor. Biol*. **1976**, 62, 447-458.
35. Nagle, J.F.; Tristram-Nagle, S. Lipid bilayer structure. *Biochi et Biophy. Acta*. **2000**, 1469, 159-195.
36. Mills, T.T.; Huang, J.; Feigenson, G. W.; Nagle, J.F. Effects of cholesterol and unsaturated DOPC lipid on chain packing of saturated gel-phase DPPC bilayers. *Gen Physiol Biophys*. **2009,** 28, 126-139.
37. Karmaker, S.; Raghunathan, V.A.; Mayor, S. Phase behavior of dipalmitoyl phosphatidylcholine (DPPC)-cholesterol membranes. *J. Phys. Condens. Matter* **2005**, 17, S1177–S1182.
38. Sun, W.J.; Suter, R.M.; Knewtson, M.A.; Worthington, C.R.; Trsitram-Nagle, S.; Zhang, R.; Nagle, J.F. Order and disorder in fully hydrated unoriented bilayers of gel phase dipalmitolyphosphatidylcholine. *Phys. Rev. E.* **1994**, 49, 4665-4676.
39. Smith, E.A.; Dea, P.K. Application of Calorimetry in Wide Context. pg. 407-444 (**2013**).
40. Leekumjorn, S., Sum, A.K. Molecular studies of the gel to liquid-crystalline phase transition for fully hydrated DPPC and DPPE bilayers. *Biochi. Et Biophys. Acta* **2007**, 354-365.
41. Katsaras, J.; Yang, D.S-C.; Epand, R.M. Fatty- acid chain tilt angels and directions in dipalmitoylphosphatidylcholine bilayers. *Biophys. Journal.* **1992**, 63, 1170-1175.
42. Atkinson, J.; Harroun, T.; Wassall, S.R.; Stillwell, W.; Katsaras, J. The location and behavior of α-tocopherol in membranes. *Mol. Nutr. Food Res.* **2010**, 54, 1-11.
43. Kamal, M.A.; Raghunathan, V.A. Modulated phases of phospholipid bilayers induced by tocopherols. *Biochim. et Biophys. Acta.* **2012**, 1818, 2486-2493.
44. Wallgren, M.; Beranova, L.; Pham, Q.D.; Linh, K.; Lidman, M.; Procek, J.; Cyprych, K,; Kinnunen, P.K.J.; Hof, M.; Grobner, G. Impact of oxidized phospholipids on the structural and dynamic organization of phospholipid membranes: a combined DSC and solid state NMR study. *Faraday Discuss.* **2013**, 161, 499-513.

45. Khandelia, H.; Mouritsen, O.G. Lipid Gymnastics: Evidence of complete acyl chain reversal in oxidized phospholipids from molecular simulations. *Biophys. J.* **2009**, 96, 2734-2743.
46. Wong-Wkkabut, J.; Wu, Z.; Triampo, W.; Tang, I.M.; Tieleman, D.P. Effect of lipid peroxidation on the properties of lipid bilayers: a molecular dynamics study. *Biophys. J.* **2007**, 90, 4488-4499.

Chapter 4

Lipid Nanotubes Formation

4.1 Introduction

In this chapter, the formation of lipid nanotube from giant unilamellar vesicle (GUV) through the combination of flow assisted and anchored system is presented. The first section provides background information on the importance of lipid nanotubes in biological system and recent studies on lipid nanotubes. Previous related studies have used molecular motors to actively pull on the GUV membrane to extract a nanotube. However, we invert the system geometry in this experiment. Molecular motors are used as static anchors linking GUVs to a two-dimensional microtubule network, and an external flow is introduced to generate nanotubes facilitated by the drag force (f_{drag}). It is a simple experimental model which avoids the complication of using ATP and dynamic of molecular motors. Through this model, the force of nanotubulation and number of motors necessary for nanotubulation can be determined. The theory will be presented before describing the experimental methods. The formation of nanotubes highly depends on the flow rate of the channel and fluidity of the membrane. The results of this experiment will be presented in two parts: observation and analysis. There were several different shapes observed, which will be discussed and elaborated upon. The analysis section applied the theoretical equation that estimated the number of motors and force of forming nanotube. We found that a drag force of approximately ≈7 pN was sufficient for tubule extraction for vesicles ranging from 1-2 μm in radius. By our method, we found that the force generated by a single molecular motor was sufficient for membrane tubule extraction from a GUV.

4.2 Background

4.2.1 Lipid nanotubes in Cells

The lipid membrane is a self-assembled system which can take on various shapes simply by changing its composition, changing the concentration, or applying a force. Lipids are amphipathic molecules and thus self-assemble into bilayers in the cell; these membranes form a barrier that compartmentalizes different cellular processes. Inside the cell, the lipid nanotube is one of various shapes that help facilitate the organization of cellular processes. It has been shown that networks of lipid nanotubes play a role in cellular communication and transport, notably in immunological responses of the synapse [1, 2], connections between the Golgi and endoplasmic reticulum [3, 4], and in chemical signaling [5]. The smooth endoplasmic reticulum is an example of a lipid nanotube system that branches out from the rough endoplasmic reticulum and nuclear envelope. These membranes tubules are found to co-localize with fundamental biopolymers in cells known as microtubules; when microtubules depolymerize, the lipid tubules retract [6]. Recent studies also demonstrate that a minimal system of microtubules and molecular motors is sufficient for tubule extraction [7].

4.2.2 Kinesin motor proteins

Molecular motors are nature's nano-machines and they drive mechanical translocation of cellular materials along their biopolymer tracks (microtubules) in cells. Kinesin (conventional kinesin, or kinesin-1) is a major microtubule-based molecular motor that utilizes the chemical energy stored in ATP to actively step along the microtubule [8]. In the absence of ATP, individual kinesin motors associate with and remain strongly bound to the microtubule, with an un-binding energy of ~5 pN per kinesin motor [9]. When multiple kinesins are present to bind the same cargo to the microtubule, the un-binding energy (or, the force necessary to detach their common cargo) scales linearly with motor number [10-16].

4.2.3 Lipid membrane

In chapter 1, it was mentioned that the lipid membrane behaves like a flexible thin molecular sheet with fluid-like in-plane properties. This fluid-like property depends on the lipid shape, membrane composition, and temperature of the system. The lipid molecules forming the bilayer diffuse freely in the plane of the monolayer or between leaflets with a mobility, often characterized by the molecular diffusion constant, D. The biological membrane has a complicated composition, including many different saturated lipids, unsaturated lipids, and cholesterol lipids. Membrane proteins also resides in biological membranes and have hydrophobic and hydrophilic properties like lipids. Each component in the membrane has an effect on the membrane fluidity and packing structure. However, in the experiment presented here, we used only one type of fatty acid. We used a dioleoyl fatty acid, which has 18 carbon length and 1 double bond as the main lipid, labeled lipid, and anchored lipid. It also has well-known elasticity to simplify our analysis of the multi-component system.

4.2.4 Recent studies on lipid nanotubes

It is widely known that lipid tubules can be extracted from flat bilayers (or vesicles) given enough applied force. Membrane tubules can be extracted from membranes on application of a force with methods such as micropipette aspiration [17, 18], optical tweezers [18-20], molecular motor pulling [21-23], and assisted shear flow [24, 25]. Each of these techniques investigate the mechanical forces necessary to deform the lipid membrane into tubules from GUVs or lamellar structures. Techniques such as force spectroscopy by atomic force microscopy [26, 27] and the Langmuir-Blodgett trough [28] have also been used to quantify the elastic parameters of various membranes without tubulation.

4.3 Our System

In this study, lipid nanotubes are formed through the combination of flow assisted and anchored system of lipid/kinesin/microtubule. The glass surface is coated with microtubules for specific binding of kinesin motor proteins, which act as static anchor sites for GUV linkages. By applying a flow to the system, free GUVs are carried by the flow but anchored GUVs experienced a resisting force due to the microtubule bound motors. Anchored GUVs either pull out lipid nanotubes, remain immobilized, or release from the anchor site. This new experimental system is motivated by previous studies where lipid tubulation is induced through a cluster of arriving and departing kinesins walking along the microtubule [23]. The kinesins are fueled by ATP, which drive the motors to walk along the microtubules. In our system, lipid nanotubes are formed in the absence of ATP. The kinesin motors are anchored to the microtubules and we can control the detachment of kinesin indirectly by the drag force from the GUVs.

Figure 4.1 is a schematic of our system to generate lipid nanotubes. The GUVs are anchored to the microtubule through a three components linkage complex. The linkage complex consists of a kinesin motor binding to the microtubule by kinesin dimers (heads of the kinesin protein). The tail of the kinesin is tagged with a histidine polymer, which binds to the amine group of the 1,2-dioleoyl-sn-glybero-3-[(N-(5-amino-1-carboxypentyl)iminodiacetic acid) succinyl] (ammonium salt) (DGS-NTA) lipid. During the process of the fluid flow in the channel by absorption, the linkage complex may be broken if there is sufficient force. It is not well understood which binding complex is broken when an anchored GUV is detached, the DGS-NTA/kinesin or the kinesin/microtubule. In either case, it is not important which bond is broken since both will not form lipid nanotubes.

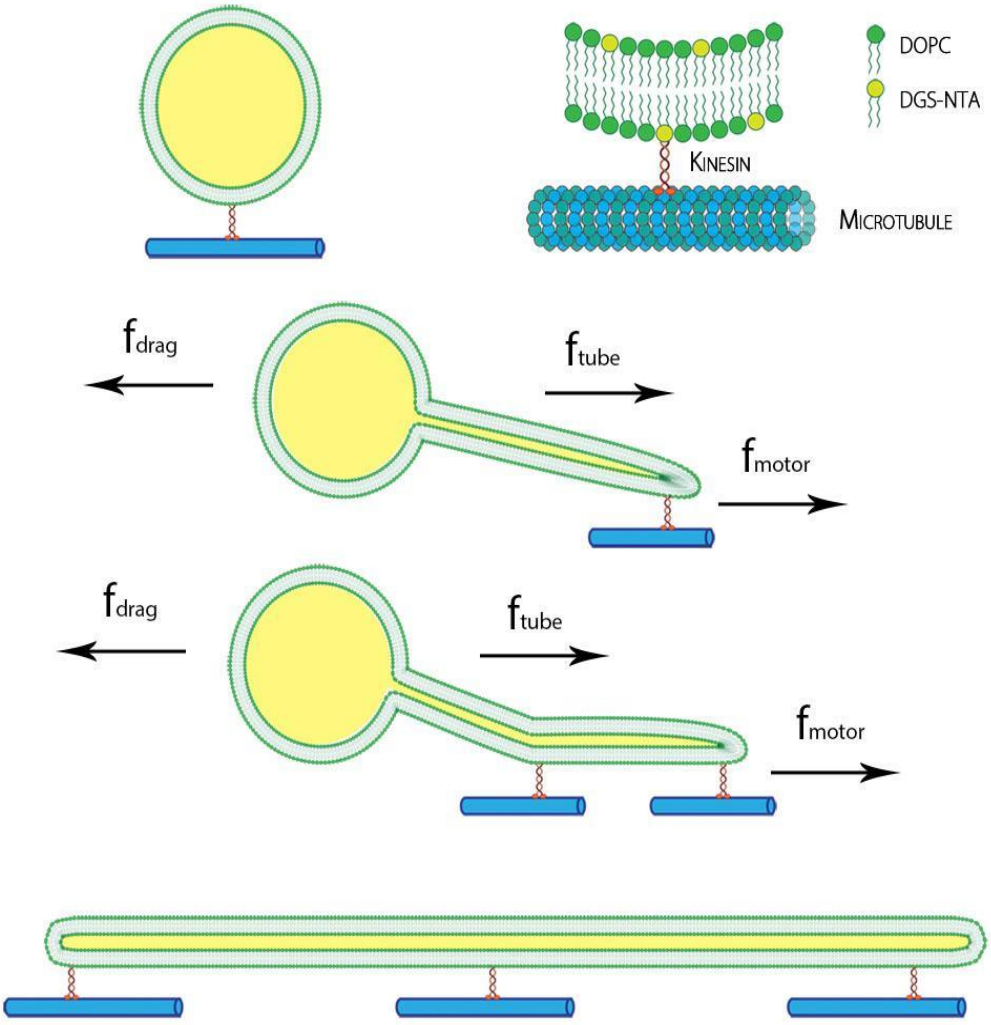

Figure 4.1 Schematic of the lipid-kinesin-microtubule anchor system and formation of lipid nanotube.

4.3.1 Drag Force

The lipid membrane forms a bilayer in aqueous solution and can be represented as a soft flexible elastic sheet that can bend out of plane or stretch laterally by increasing the distance between each lipid molecule. Applying a point force perpendicular to the bilayer will deform the membrane from its equilibrium curvature potentially causing a tube to be extracted. For our system, a GUV binds to a kinesin that anchors to a microtubule. When a flow is applied, a nanotube is extracted from the moving GUV due to the force applied by the anchored kinesin. In a flow, GUVs experience a drag force given by Stoke's equation

$$f = 6\pi\eta r v \qquad \text{(Eq. 16)}$$

where r is the GUV radius under a fluid flow of velocity, v, in a medium of viscosity, η. The viscosity of a dilute aqueous solution near the glass surface in the flow cell can be estimated as η = g ($1e^{-3}$ N s/m^2), where g is a correction factor for flow close to a surface according to Faxen's law [29].

$$g = \left(1 - \frac{9}{16}\left(\frac{r}{h}\right) + \frac{1}{8}\left(\frac{r}{h}\right)^3 - \frac{45}{256}\left(\frac{r}{h}\right)^4 - \frac{1}{16}\left(\frac{r}{h}\right)^5\right) - 1 \qquad \text{(Eq. 17)}$$

where h is the distance from the glass surface and r is the GUV radius. For example, in our flow cell we approximate g = 2.36 for a 1 μm radius GUV, 100 nm above the surface [30]. The g value is typically between 1 and 3 and only valid for when $h - r \geq 0.02r$. We calculated the drag force shown in Figure 4.2 for DOPC GUVs under high and low flow rate.

We first look at a simple system of glass beads or rigid GUVs with high bending rigidity like DPPC in the gel phase, anchored to the surface of microtubule by kinesin to understand the force diagram. In this case we do not expect a tube to form. The force balance function is $f_{drag} \leq f_{motor}$ (motor force). If f_{drag} exceeds the opposing force of the cumulative motors, f_{motor}, that are anchored, then the anchored kinesin/GUV would detach from the microtubule. If f_{drag} is less or equal to the f_{motor}, then the GUV is immobilized. We see clear evidence of this effect with DPPC GUVs, they either detach and are washed away by the flow or are immobilized without tube formation.

4.3.2 Tubulation Force

The theory of lipid nanotube extraction with an applied force was introduced in Chapter 2 section 2.4. By using the equation:

$$f = \frac{2\pi k}{r} \qquad \text{(Eq. 18)}$$

the force it takes to pull a tube of radius r out of a GUV with bending rigidity, k_b, can be calculated. This force is defined as f_{tube} [31, 32]. In our system, the k_b values for DOPC and DPPC are 85 pNnm [33, 34] and 1100 pNnm respectively [35]. We used fluorescence microscopy to observe the lipid nanotubes, however, measuring the tube radius was quite complicated due to limited resolution. According to several other studies, it was determined to be 20-110 nm [7, 36-38]. If a tube has a radius of 50 nm or 100 nm then we get f_{tube} of 10.7 pN and 5.35 pN respectively.

The difference between the f_{drag} and the total f_{tube} for all attached motors resulted in the net force exerted by the motors on the vesicle, $f_{drag} - nf_{tube} = f_{vnet}$, where n is the number of tubes generated depending on the number of linkages of DGS-NTA /kinesin/microtubule. This equation is taken into consideration that each linkage is far enough from each other to generate point deformation which lead to tubulation. If the motors are close then area deformation is dominant where the GUV stretch into an ellipsoid resulting in no nanotubes. We observed no more than one lipid nanotube per GUV in our data, however it is seen in coalescence tether experiments that nanotubes generated close to each other will fuse into a single nanotube [18]. When the nanotubes are fused, the f_{tube} would be distributed. However, the formula $f_{drag} - nf_{tube} = nf_{motor}$ needs to be satisfied initially to generate nanotubes before tube fusion due to distance points of deformation.

4.4 Experimental

4.4.1 Materials

All of the lipids 1,2-dipalmitoyl-sn-glycero-3-phosphocholine (DPPC), 1,2-dioleoyl-sn-glycero-3-phosphocholine (DOPC), 1,2-dioleoyl-sn-glybero-3-[(N-(5-amino-1-carboxypentyl)iminodiacetic acid) succinyl] (ammonium salt) (DGS-NTA), and 1,2-dioleoyl-sn-3-phosphoethanolamine-N-(7-nitro-2-1,3-benzoxadiazol-4-yl) (ammonium salt) (DOPE-NBD)were purchased from Avanti Polar Lipids in chloroform and used without further purification. Lyophilized tubulins were purchased from Cytoskeleton (Cat. T240). Recombinant kinesin protein (K560) were purified as previously described [10]. Silicon beads of 2.47 μm (SS04N) and 4.56 μm (SS06N) in water were purchased from Bangs Laboratories, Inc.

4.4.2 Giant Unilamellar Vesicles (GUVs)

The general method for GUV formation has been introduced in Chapter 2 Section 2.5. To prepare giant unilamellar vesicles (GUVs), 94.95 mol% DPPC or DOPC are mixed with 5 mol% DGS-NTA and 0.05 mol% DOPE-NBD to a final concentration of 5 mM in chloroform. DGS-NTA is chosen because it can bind directly to the HIS-tag of the kinesin protein [39]. DOPE-NBD is a labeled lipid with absorbance at 460 nm and emission at 535 nm for fluorescence imaging. Droplets of lipid mixtures are deposited onto clean indium tin oxide (ITO) slides and allowed to dry in a vacuum chamber overnight to remove excess chloroform. Then the slides are assembled into an electroformation chamber. Two ITO slides are placed between a greased Teflon O-ring with the dried lipid sides facing each other. The chamber is filled with 200 mM sucrose. Once the chamber is assembled, a 2 V sinusoidal voltage with 7.5 Hz is applied across the chamber and incubated at 45°C for 3 hours. GUVs are formed by budding from the stack of bilayers that were hydrated at the ITO glass surface. GUV solution are harvested and stored in centrifuge tubes for further use. GUVs produced from this parameter range from 1 μm -10 μm.

4.4.3 Flow Cell

A flow cell is the platform for the generation of lipid nanotubes. In Chapter 2 Section 2.6, the methodology of the flow cell assembly was introduced. This flow cell is a simple, cost effective, time saving, and disposable design. The disadvantage of this device is that the flow rate is difficult to control because flow is induced by absorption of filter paper at one terminal. Also, another disadvantage is that the flow rate will not be constant. A device with control of flow rate typically microfluidic chip that uses a system of syringes and pumps, however, it is time consuming to fabricate the chip. For our system, a simple flow cell is sufficient because we only need to test two different flow rates, high flow through absorption of filter paper and low flow through surface tension.

4.4.4 Lipid Nanotube Formation

To assemble microtubules, 5 µg/µl tubulin in PEM80 buffer (80 mM PIPES pH 6.9, 2 mM $MgCl_2$, and 0.5 mM EGTA) supplemented with 1 mM GTP and 5% of glycerol was incubated in ice for 3 minutes and then in water bath at 37ºC for 20 minutes. The assembled microtubules were stabilized by mixing in equal volume in PEM80 buffer supplemented with 50 µM taxol and 2 mM of GTP, and then incubated for another 20 minutes at 37ºC. Flow cells were prepared by with placing a polylysine coated cover glass on top of microscope glass slide using double sided tape. The resulting flow cell volume was approximately 12 µL. To pattern the flow cell with microtubules, 12 µL of microtubule solution (15 µg/ml in PEM80, supplemented with 1 mM GTP, 25 µM taxol) was introduced to the flow cell. After 5 minutes of incubation, unbound microtubules were washed away with 12 µl of wash solution (PEM25 supplemented with 1 mM GTP, 25 µM taxol). The flow cell was then blocked with 5.55 mg/ml casein supplemented with 1mM GTP and 25 µM taxol to prevent nonspecific attachment of kinesin onto bare glass. Then 10 µL of kinesins (4 µM) was introduced into the flow cell to allow for binding to microtubules. After five minutes, excess kinesin was washed away with 12 µl wash solution (PEM80 supplemented with 1 mM GTP, 25 µM taxol), and GUVs were introduced into the flow cell and allowed to settle for 10 min. To generate lipid tubules, 20 µl wash buffer was drawn through the flow cell using filter paper.

4.4.5 Lipid Diffusion Measurement

The diffusion constant, D, for GUVs containing 5.00 mol% DGS-NTA was assessed using fluorescence recovery after photo bleaching (FRAP) on supported lipid bilayers. Lipid mixtures of 94.95 mol% DOPC, 5.00 mol% DGS-NTA, and 0.05 mol% DPPE-NBD (dye) were mixed in chloroform and vacuum dry to remove excess chloroform. Dried lipids were then rehydrated with water to final concentration. Small unilamellar vesicles were formed via tip sonication and drop casted onto a clean glass slide coated with bovine serum albumin. Then the sample was incubated at 50ºC for 1 hour to allow for fusion on the surface forming a single bilayer. The bilayer was observed using fluorescence microscopy and a small circular region overexposed by high power to bleach the region. The recovery of the bleached region was recorded for analysis of the

diffusion constant for the lipid mixture. Snapshots of bleached region recovery was captured by Q-imaging camera at 120 sec interval for 20 minutes. Diffusion constant, *D*, was determined by first fitting Soumpasis formula to the data [40].

$$f(t) = e^{\frac{-2\tau_D}{t}}[I_0(\frac{2\tau_D}{t}) + I_1(\frac{2\tau_D}{t})] \quad \text{(Eq. 19)}$$

where $f(t)$is the normalized fluorescence**,** τ_D is the characteristic time for diffusion, *I* is the fluorescence intensity, and *t* is the time. τ_D is determined from the fit, which we can now calculate the *D* value for a bleached region of radius ω using

$$\tau_D = \frac{\omega^2}{4D} \quad \text{(Eq. 20)}$$

4.4.6 Flow Velocity and Measurement

Under high flow rates, we observed that most GUVs greater than 4.5 μm in diameter were washed away from the flow cell leaving smaller ones that were anchored. However, with a lower flow rate, anchored GUVs with diameters up to 10 μm remain in the flow cell. To quantify the flow rate, we calculated the speed of flowing 2.47 μm glass beads using bright field optical microscopy. For a low flow rate, a 20 μl of the wash buffer was deposited at one end of the channel. This will create a low flow as the solution spreads in every direction due to capillary action. We generated a high flow rate using a strip of 1 x 4 cm filter paper to draw through 20 μL of wash solution to the opposite end of the flow cell. We measured an average low flow rate at 61.3 ± 3.7 μm/s and high flow rate at 177.6 ± 18.2 μm/s. We're aware that the flow rate in either case is not constant. We calculated an average flow rate for the first 2 seconds during which time we expected to generate the fastest flow. We noted that bigger GUVs are not washed from the flow cell channel under a low flow rate while the high flow rate was sufficient to detach the big vesicles from the anchor points.

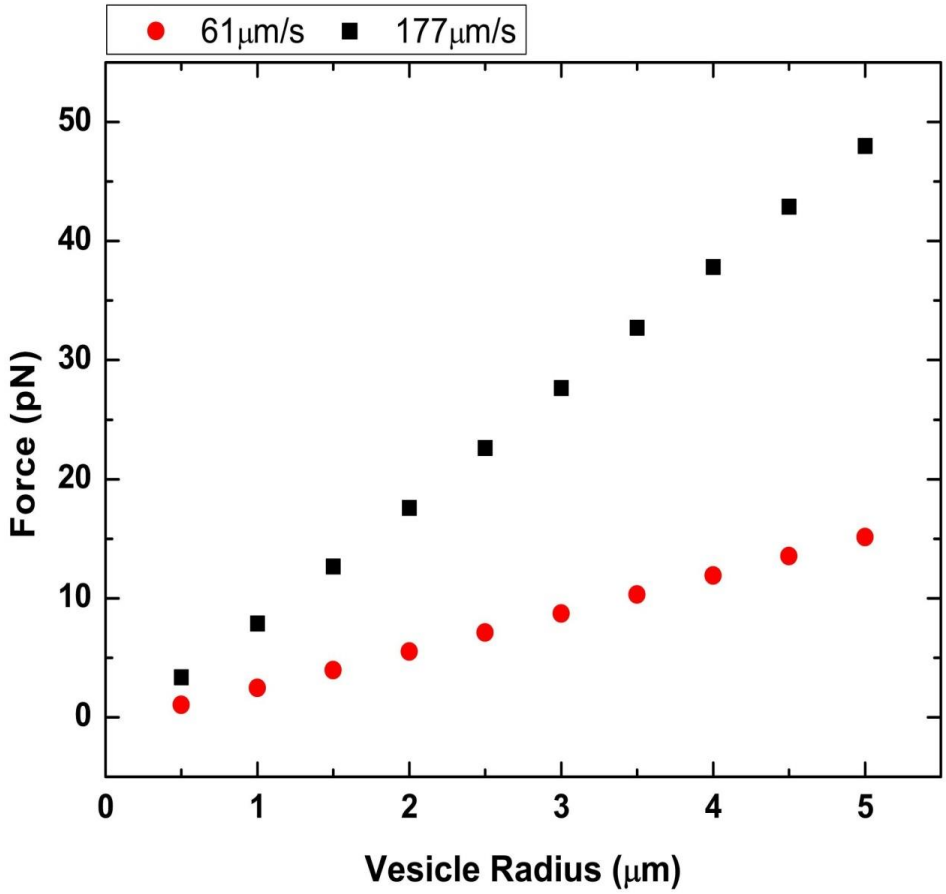

Figure 4.2 Plot of vesicle radius vs drag force. Two different flow rate at 61.3 μm/s and 177.6 μm/s were plotted using both Stoke's and Faxen's law.

4.5 Results

4.5.1 Crumpled Vesicles

At room temperature, DPPC GUVs are not perfectly spherical but crumpled due to the tilted packing in the bilayer, shown in Figure 4.3 [41]. DPPC membranes exhibit gel phase below 43ºC, which make the membrane rigid and have almost no diffusion of the molecules in the membrane. It is difficult for the tilted gel phase to bend into a circle, therefore causing defects at the bends. If the DPPC GUVs are heated to above transition temperature, then they will become spherical. The tight packing of the DPPC lipids generates a high bending rigidity of 1100 pNnm. Due to their high bending rigidity, no lipid nanotubes were formed when the flow was introduced. DPPC GUVs as big as 20 μm were flown into the flow cell channel and allowed to sink to the surface by the gravity

of the sucrose interior. Afterward, the channel was washed by filter paper absorption and only GUV's with sufficient anchors to prevent being wash away were left behind.

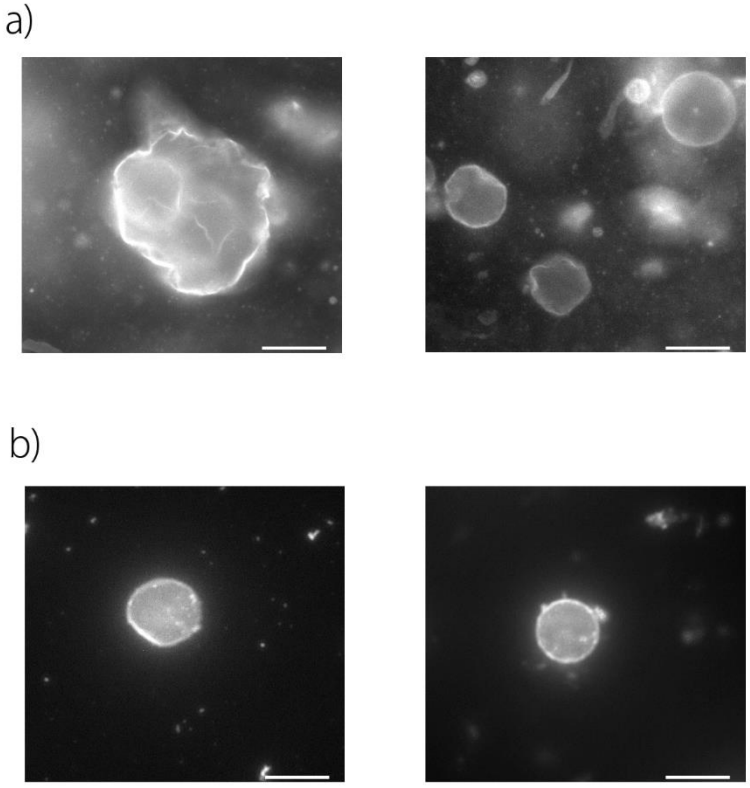

Figure 4.3 Fluorescence microscopic images of DPPC crumpled GUVs. a) DPPC GUVs before flow channel wash b) DPPC GUVs after flow channel wash. Scale bars are 10 μm.

4.5.2 Stabled Full Vesicles

Unlike DPPC GUVs, DOPC GUVs were not crumpled at room temperature because the membranes were in liquid disordered phase. The transition temperature of DOPC is 10ºC. This section presents anchored DOPC GUVs that do not generate lipid nanotubes and do not stretch. The simplest case is for small GUVs below 1.5 μm in diameter. They were viewed as being immobilized because the generated drag force was not sufficient enough to displace the GUVs. Furthermore, lipid nanotubulation was unfavorable for small GUVs because the radius of possible nanotubes was too big compared to the GUV radius. Any possible displacement of the anchored GUVs would have stretched the whole vesicle, not just a small nanotube. However, there were bigger GUVs observed to remain

immobilized as well. This is possibly due to it having more anchors. This will be discussed in more detail in later sections.

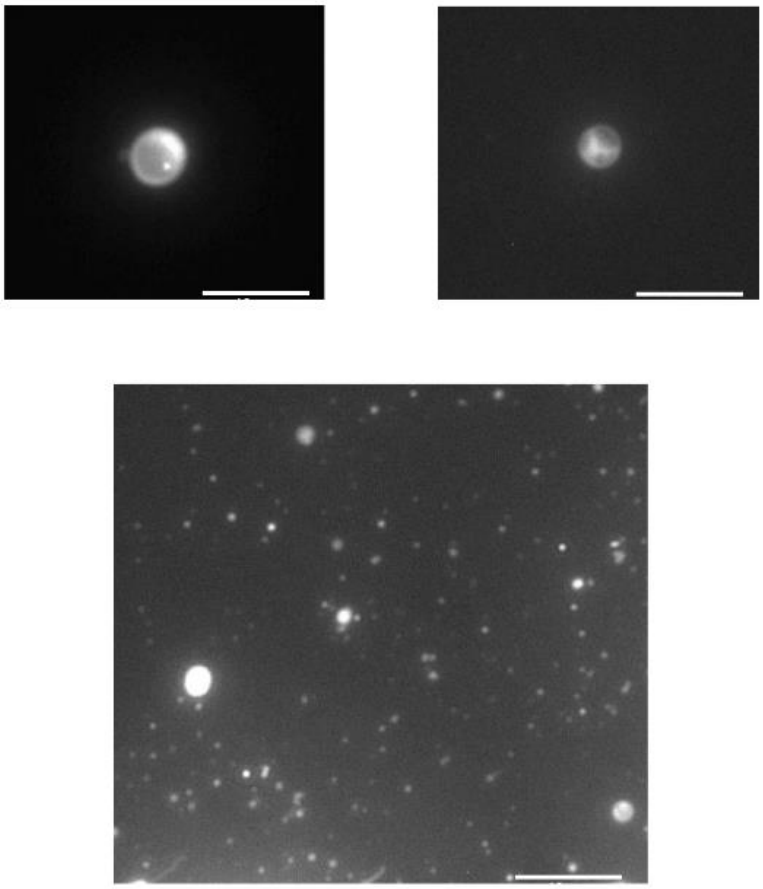

Figure 4.4 Fluorescence microscopic images of DOPC GUVs. Scale bars are 10 μm.

4.5.3 Tethered Vesicles

A tethered vesicle is a vesicle with a lipid nanotube pulled out using the same membrane, shown in Figure 4.5 and Figure 4.6. The volume between the vesicle and the nanotube was continuous. Under the right conditions, lipid nanotubes were extracted from DOPC GUVs that had formed linkages of DGS-NTA/kinesin/microtubule. Without the linkage, the GUVs would have been washed away by the flow. At a low flow rate of 61.3 μm/s, lipid nanotubes were formed for GUVs greater than 4.5 μm in diameter. However, at a

high flow rate, lipid nanotubes were formed for smaller GUVs between 2 μm and 4.5 μm in diameter. In Figure 4.7, a 2 μm diameter DOPC GUV generated a lipid nanotube under the high flow rate of 177.6 ± 18.2 μm/s and stretched to 57 μm in length. Since we imaged the lipid nanotubes using fluorescence microscopy, an optical technique, we could not accurately measure the radius. However, various measurement techniques have been used by other research groups, and have found that a typical nanotube is between 20 nm and 110 nm [7, 36-38].

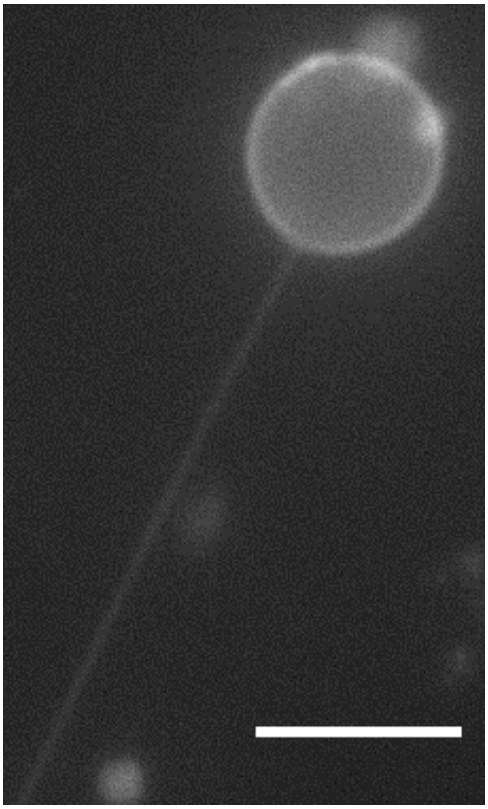

Figure 4.5 Fluorescence microscopy of DOPC tethered GUV. Scale bar is 10 μm.

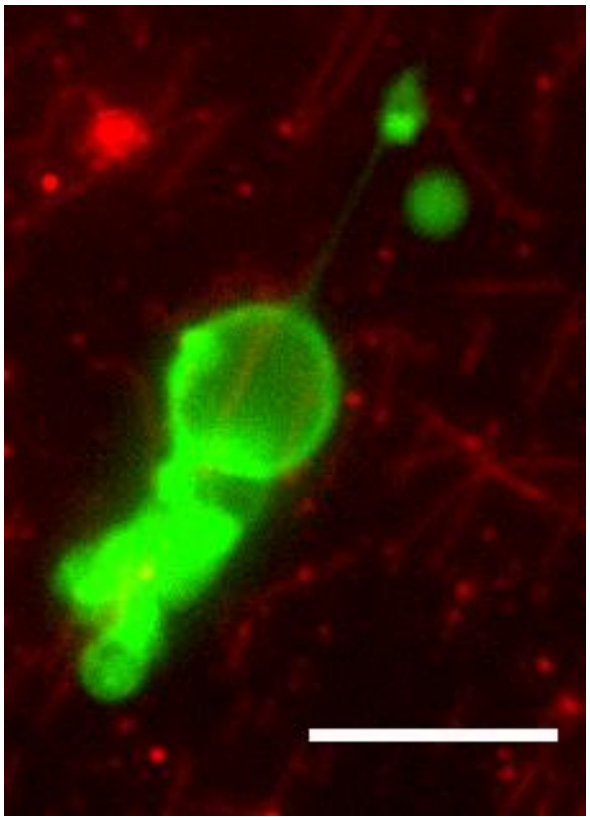

Figure 4.6 Fluorescence microscopy overlay image of DOPC tethered GUV. The microtubules were labeled in red and GUV labeled green. Scale bar is 10 μm.

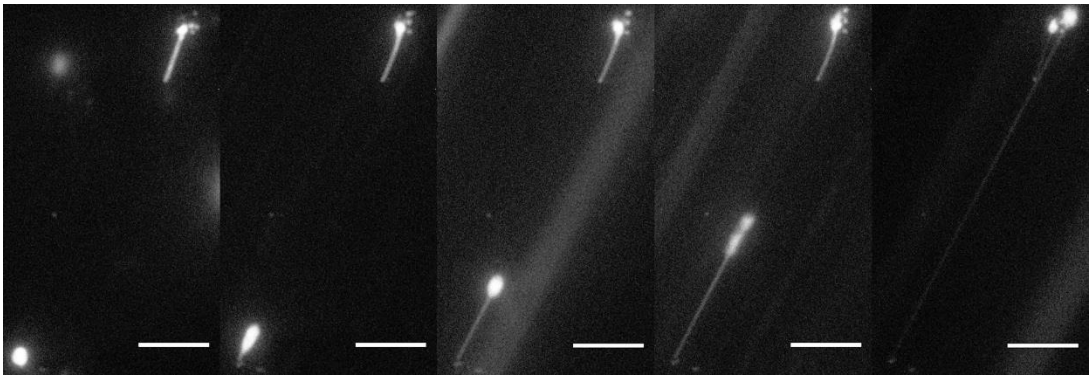

Figure 4.7 Fluorescence microscopy of lipid tubulation of DOPC/DGS-NTA (5 mol%) GUV of 2 μm in diameter under high flow. Scale bar is 10 μm.

4.5.4 Lipid Nanotubes

Lipid nanotubes were observed after introducing the flow into the channel shown in Figure 4.8. Anchored DOPC GUVs that met the right conditions were able to extract lipid nanotubes and fully stretch into a cylindrical tube. The lipid nanotubes were very stable because additional flow in the channel do not wash the lipid nanotubes from the microtubules. This was good evidence that there were multiple linkages along the nanotube. Without multiple linkages, the lipid nanotubes would have returned back into a GUV. In most cases, lipid nanotubes did not experience further stretching because the drag force was very small, due to the low radius. There were lipid nanotubes that contained a small vesicle along the nanotube. These small vesicles did move along the nanotube during additional flow processes, but most did not further increase the length of the nanotube unless it could generate enough drag force. Lipid nanotubes were measured to be as high as 100 μm.

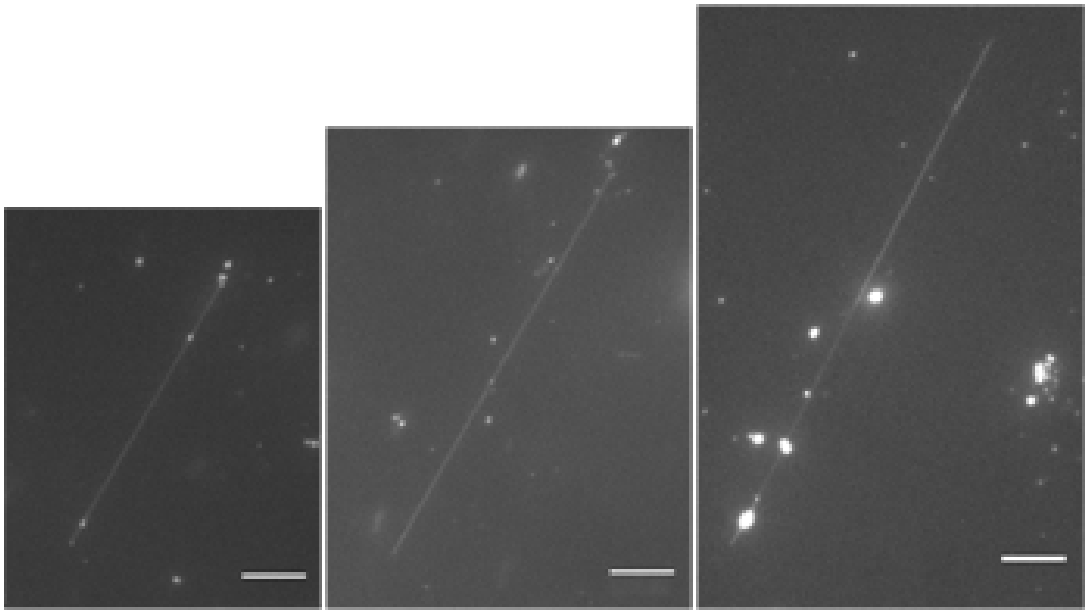

Figure 4.8 Fluorescence microscopy of DOPC lipid nanotubes. Scale bars are 10 μm.

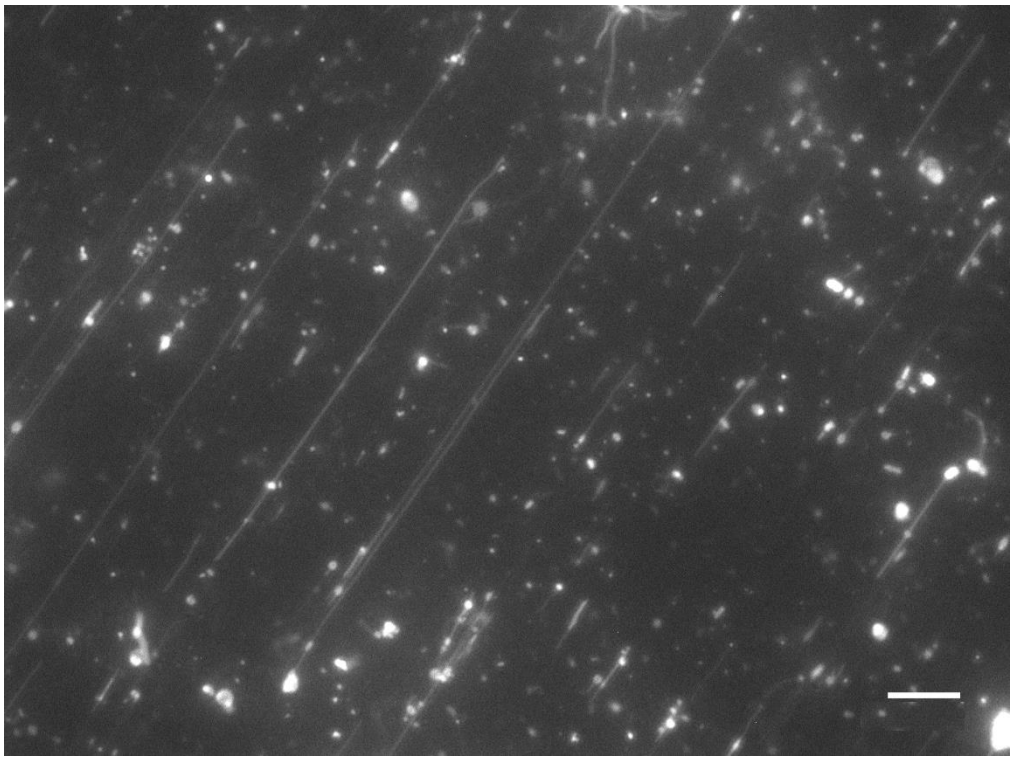

Figure 4.9 Fluorescence microscopy of DOPC lipid nanotubes and GUVs. Scale bar is 10 μm.

4.5.5 Stretch and Retraction

During the flow process, some DOPC GUVs were stretched by the drag force from the flow while some remained un-stretched, as shown in Figure 4.9. This was dependent on the number of anchors of each GUV. In Figure 4.10, the GUV remained at the same position and did not stretch under a flow rate of 177 μm/s. However, a 3 μm diameter GUV was stretched under the same flow rate, and no nanotube was formed. It was stretched into an egg-like shape, and retracted back to its initial position when the flow stopped. A lipid nanotube could not be formed because the radius of the extracted region was too large. The vesicle's ability to retract back to its initial state is because the lipid membrane is similar to a spring.

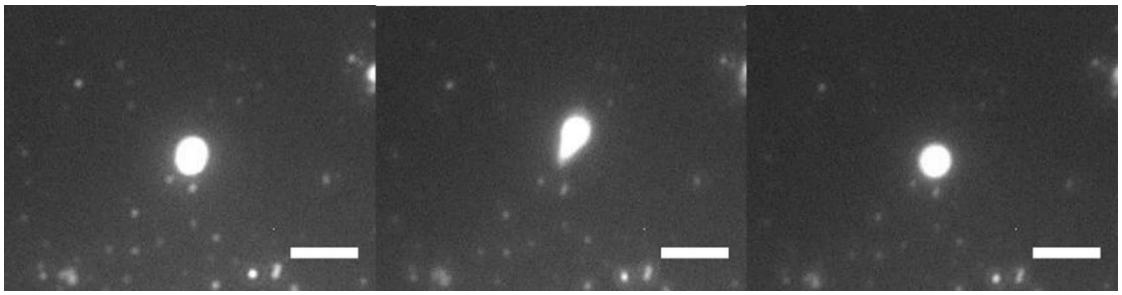

Figure 4.10 Fluorescence microscopy of DOPC GUV in stretch and retract motion. Scale bar is 10 μm.

4.6 Discussion

4.6.1 Effect of Bending Rigidity

To compare the effects of membrane composition on tubulation we also prepared GUVs with a different membrane bending rigidity, k_b. The bending rigidity is the membrane's resistance to bending deformation. At room temperature, DOPC is in L_α phase with k_b = 85 pNnm [34] but DPPC exhibits the gel phase at the same temperature with k_b = 1100 pNnm [35]. To compare these radically different membrane rigidities in our experiment we formed GUVs with the DPPC membrane by electroformation and followed up with the above described procedure to produce lipid nanotubes.

4.6.2 Tubulation Cases

In our experiments we have observe three different cases where $f_{vnet} = f_{drag} + nf_{tube}$

1) $f_{vnet} > nf_{motor}$: Large GUVs are washed from the flow cell after introduction of flow. Large GUVs generate a f_{vnet} higher than the nf_{motor} from anchored kinesin(s). Kinesin motors' resisting force is not sufficient to overcome the strong drag force and thus the large GUV is swept away from the surface.

2) $f_{vnet} \leq nfmotor$: Under our high flow rate of ≈177 μm/s, smaller GUVs less than 5 μm that are anchored to the microtubule via kinesin are not washed from the flow cell. f_{vnet} is not strong enough to detach the motors from their bound state. Depending on the number of motors being attached to the microtubule and their distribution, a tube may be pulled out from the vesicle given a sufficiently deformable membrane.

3) $f_{vnet} \ll nfmotor$: The net force from the drag force and tube force is too low compared to the max force from the total number of bound kinesins. In this group of GUVs, no nanotube is generated because it would cost too much energy to make tubes per anchored motor. In this case, having too many bound anchor sites and a stiff membrane prohibits the GUV from either washing away or pulling out nanotubes.

4.6.3 Determination of Motors for Nanotubulation

In Figure 4.11 and Figure 4.12, we calculated the theoretical minimal number of motors needed to successfully anchor a GUV and generate a nanotube given the calculated drag force for both high and low flow. As mentioned in the results section, large GUVs are washed from the flow cell under high flow, as represented in case 1. This was because they generated a high drag force that overcame the resisting force from the combined anchored motors. This calculation of motor numbers assumes that each motor has a maximum binding force of 5 pN to the microtubule. Lipid nanotubes that were extracted from the GUVs are 67.6 nm in radius. We assumed 67.6 nm for the radius of generated nanotubes in all GUVs estimated because it was the smallest radius generated with our system for both low flow and high flow. From the graphs, we found that nanotubulation requires a minimum of one or two motors initially in both low and high flow. According to the graph, if there are more motor/lipid linkages than the estimated value, then the GUV does not form a nanotube and remains immobilized. However, if there are less kinesin/DGS-NTA linkage, then the GUV flows away. In Figure 4.12, we plotted the estimated number of motors for GUVs up to 5 μm in radius but only observed nanotubes up to 2 μm. We believe it is possible to form nanotubes for the bigger GUVs by increasing the concentration of kinesin motors and microtubules on the substrate. However, these linkages have to be distanced enough from each other, which can be quite difficult. If too many anchored motors are close together, which is likely the case especially on the same microtubule, only the motors at the edge experience the force from the vesicle. Having too many anchor sites will not cause a point deformation, but it will cause area deformation much like stretching a GUV into an ellipsoid. We have observed some GUVs to stretch into ellipsoids in the presence of the flow, but retracted back to a sphere when the flow was stopped (Fig. 4.10).

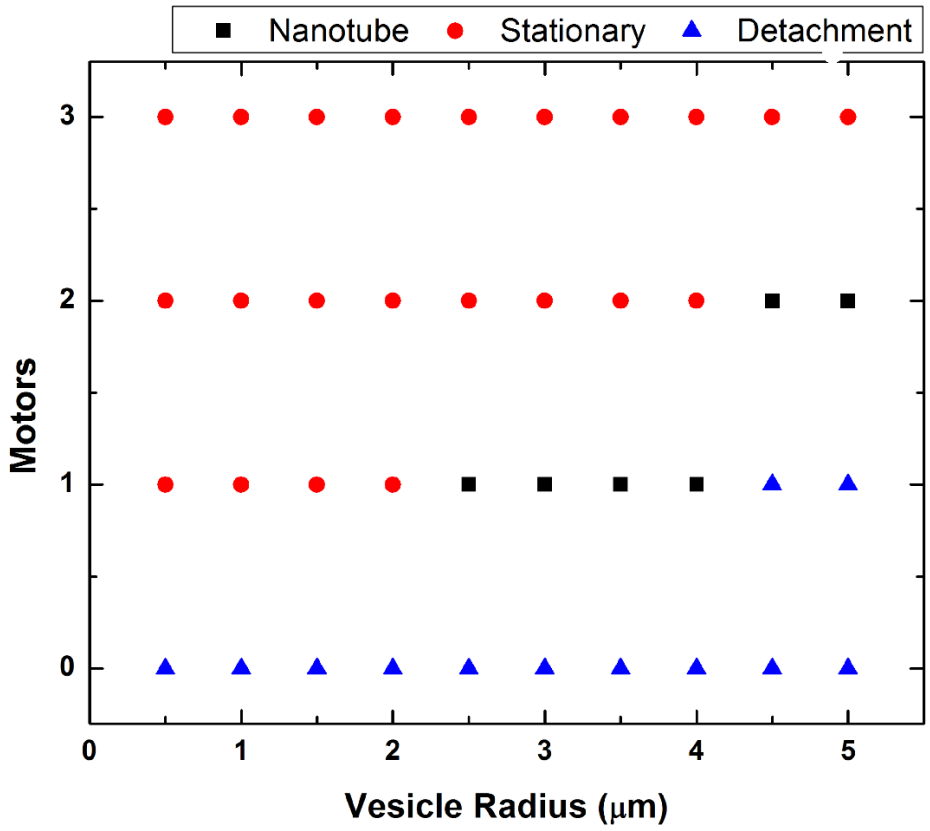

Figure 4.11 Phase diagram plot of vesicle radius vs motors for DOPC GUVs under low flow.

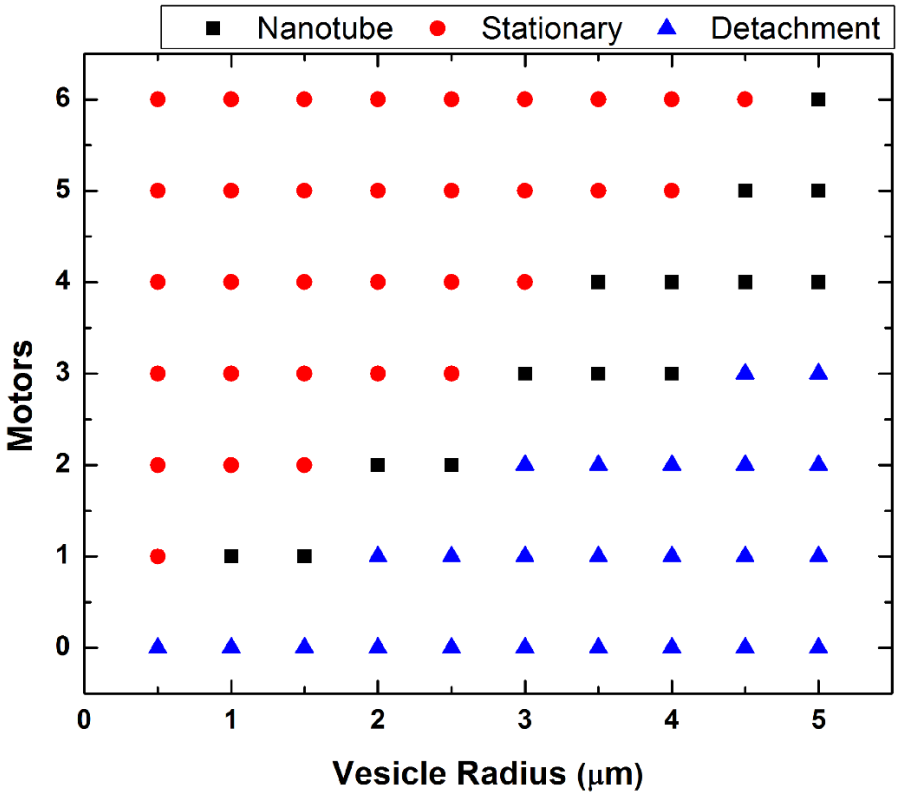

Figure 4.12 Phase diagram plot of vesicle radius vs motors for DOPC GUVs under low flow.

4.6.4 Stabled Shape via Multiple Kinesin Linkages

Tethered GUVs and fully stretched GUVs into cylinders are evidence of multiple linkages of the DGS-NTA lipids to kinesin motor proteins. During the flow process, tubulation can be observed from displaced anchored GUVs. When the flow was slowed down or stopped, GUVs retracted back to their initial location. However, during the process of tubulation, if a GUV was able to make another lipid/kinesin/microtubule linkage, then a tethered GUV was stabilized because it retracted back to its most recent anchor. For fully stretched vesicle into cylindrical tube, both ends of the cylinder had anchor sites. The probability of making additional tube-microtubule motor linkages is high with our lipid mixture of DOPC with 5mol% DGS-NTA. The lateral diffusion of DOPC/DGS-NTA lipid molecules at room temperature is high, 9.01 ± 0.58 $\mu m^2/s$ compared to pure DOPC at 8.2 $\mu m^2/s$ [42], shown in Figure 4.13.

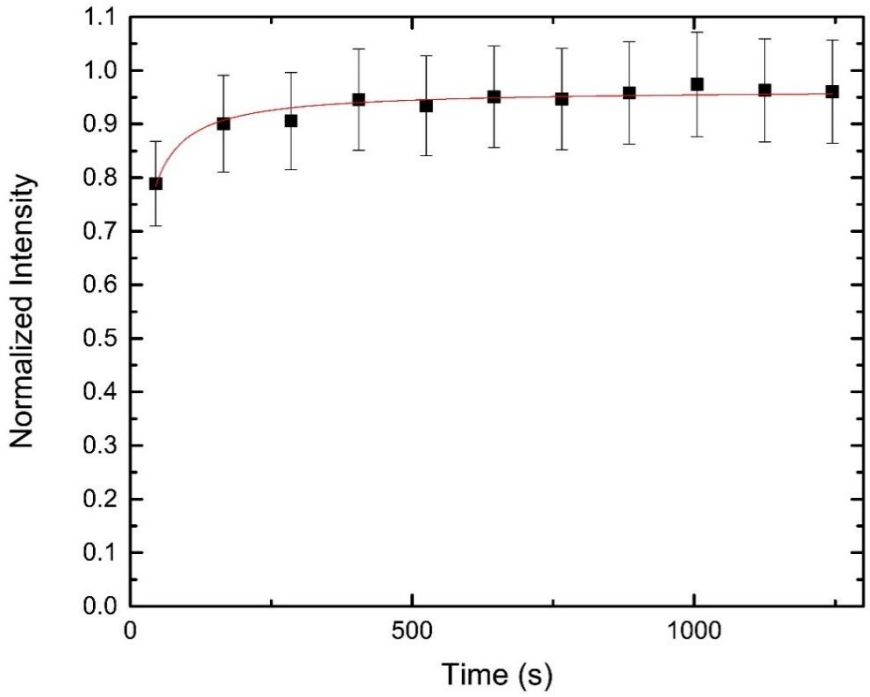

Figure 4.13Plot of time vs intensity for the membrane recovery of 5 mol% DGS-NTA/95 mol% DOPC membrane.

The hydrophobic tails of both lipid molecules are the same but DGS-NTA have a bigger hydrophilic head which may contribute to increased lateral diffusion. This suggests that for a moving GUV traveling along microtubule coated with kinesin motors, there's a high probability that a DGS-NTA lipid will be present at the bottom of the GUV to bind with incoming kinesin. Increasing the concentration of kinesin motors potentially increases the number of fully stretched GUVs as extra binding sites can act to hold the tubule in place, however there will be a trade-off because too many motors present in the system will affect its ability to even form a nanotube and elongate in the case of multiple initial bindings. The fully stretched tethered tubules we observe are very stable and straight, they all stretch in the direction of the flow. We also observe that once stabilized, additional stretching due to a secondary flow does not occur. This is likely because with a cross section of only approximately 140 nm the tubes do not generate enough drag force to detach the multiple bound kinesin motors from the microtubules and allow further extension.

4.7 Conclusion

We have developed a simple experimental system to generate flow-induced lipid nanotubes using kinesin molecular motors anchored to microtubules. By this method, we can estimate the number of motors necessary for anchor and tubulation. Our experiments demonstrate that it takes as little as one to two motors to pull out a tube from a GUV. The fabrication of the flow cell and experimental procedure is simple, quick, and provide fast readout of the motor count. A flow cell with better flow rate control will be fabricated in the future for quantitative analysis. The presence of nanotube stability requires multiple anchors for GUVs that do not fully retract back to its initial position and fully stretched nanotubes. This may provide possible insight to stability of nanotube networks in cells.

1. Carlin, L. M.; Eleme, K.; McCann, F. E.; Davis, D. M. Intercellular transfer and supramolecular organization of human leukocyte Antigen C at inhibitory natural killer cell immune synapses. *J. Exp. Med.* **2001,** 194, 1507-1517
2. McCann, F. E.; Eissmann, P.; Önfelt, B.; Leung, R.; Davis, D.M. The activating NKG2D ligand MHC class I-related chain a transfers from target cells to NK cells in a manner that allows functional consequences. *J. Immunol.* **2007,** 178, 3418-3426.
3. Hirschberg, K., Miller, C. M., Ellenberg, J., Presley, J. F., Siggia, E. D., Phair, R. D. & Lippincott-Schwartz, J. Kinetic analysis of secretory protein traffic and characterization of golgi to plasma membrane transport intermediates in living cells. *J. Cell Biol.* **1998,** 143, 1485–1503
4. Martinez-Menarguez, J. A., Geuze, H. J., Slot, J. W. & Klumperman, J. Vesicular tubular clusters between the ER and golgi mediate concentration of soluble secretory proteins by exclusion from COPI-coated vesicles. *Cell* **1999,** 98, 81–90
5. Watkins, S. C.; Salter, R. D. Functional connectivity between immune cells mediated by tunneling nanotubules. *Immunity* **2005,** 23, 309-318.
6. Terasaki M, Chen LB, Fujiwara K. Microtubules and the endoplasmic reticulum are highly interdependent structures. *J Cell Biol.* **1986,** 103, 1557–1568
7. Roux, A.; Cappello, G.; Cartaud, J.; Prost, J.; Goud, B.; Bassereau, P. A minimal system allowing tubulation with molecular motors pulling on giant liposomes. *PNAS* **2002,** 99, 5394-5399.
8. Schnitzer, M.J. and Block, S.M. Kinesin hydrolyses one ATP per 8-nm step. *Nature* **1997,** 388, 386-390.
9. Uemura, S.; Kawaguchi, K.; Yajima, J.; Edamatsu, M.; Toyoshima, Y.Y.; Ishiwata, S. Kinesin-microtubule binding depends on both nucleotide state and loading direction. *PNAS* **2002,** 99, 5977-5981
10. Xu, J.; Reddy, B.J.; Anand, P.; Shu, Z.; Cermelli, S.; Mattson, M.K.; Tripathy, S.K.; Hoss, M.T.; James, N.S.; King, S.J.; Huang, L.; Bardwell, L.; Gross, S.P. Casein kinase 2 reverses tail-independent inactivation of kinesin-1. *Nat Commun.* **2012,** 3, 754.
11. Shubeita, G.T.; Tran, S.L.; Xu, J.; Vershinin, M.; Cermelli, S.; Cotton, S.L.; Welte, M.A.; Gross, S.P. Consequences of motor copy number on the intracellular transport of kinesin-1-driven lipid droplets. *Cell* **2008,** 135, 1098–1107
12. Mallik, R.; Petrov, D.; Lex, S.A.; King, S.J.; Gross, S.P. Building complexity: an in vitro study of cytoplasmic dynein with in vivo implications. *Curr Biol*. **2008,** 15, 2075–2085.
13. Vershinin, M.; Carter, B.C.; Razafsky, D.S.; King, S.J.; Gross, S.P. Multiple motor based transport and its regulation by Tau. *Proc Natl Acad Sci USA* **2007,** 104,87–92.
14. Jamison, D.K.; Driver, J.W.; Rogers, A.R.; Constantinou, P.E.; Diehl, M.R. Two kinesins transport cargo primarily via the action of one motor: implications for intracellular transport. *Biophys J.* **2010,** 99, 2967–2977.
15. Vershinin, M.; Xu, J.; Razafsky, D.S.; King, S.J.; Gross, S.P. Tuning microtubule-based transport through filamentous MAPs: the problem of dynein. *Traffic* **2008,** 9, 882–892.

16. Xu, J.; Shu, Z.; King, S.J.; Gross, S.P. Tuning multiple motor travel via single motor velocity. *Traffic* **2012,** 13, 1198-1205.
17. Mannerville, J.B.; Bassereau, P.; Ramaswamy, S.; Prost, J. Active membrane fluctuations studied by micropipette aspiration. *Phys Rev E* **2001,** 64, 021908.
18. Cuvelier, D.; Derenyi, I.; Bassereau, P.; Nassoy, P. Coalescence of membrane tethers: experiments, theory, and applications. *Biophys J.* **2005,** 88, 2714-2726.
19. Koster, G.; Cacciuto, A.; Derenyi, I.; Frenkel, D., Dogterom, M. Force barriers for membrane tube formation. *Phys Rev Lett.* **2005,** 94, 068101.
20. Inaba, T.; Ishijima, A.; Honda, M.; Nomura, F.; Takiguchi, K.; Hotani, H. Formation and maintenance of tubular membrane projections require mechanical force, but their elongation and shortening do not require additional force. *J. Mol Biol.* **2005,** 348, 325-333.
21. Leduc, C.; Campas, O.; Zeldovich, K.B.; Roux, A.; Jolimaitre, P.; Bourel-Bonnet, L.; Goud, B.; Joanny, J.; Bassereau, P.; Prost, J. Cooperative extraction of membrane nanotubes by molecular motors. *PNAS* **2004,** 101, 17096-17101.
22. Shaklee, P.M.; Idema, T.; Koster, G.; Storm, C.; Schmidt, T.; Dogterom, M. Bidirectional membrane tube dynamics driven by nonprocessive motors. *PNAS* **2008,** 105, 7993-7997.
23. Koster, G.; VanDujin, M.; Hofs, B.; Dogterom, M. Membrane tube formation from giant vesicles by dynamic association of motor proteins. *PNAS* **2003,** 100, 15583-15588.
24. Sekine, Y.; Abe, K.; Shimizu, A.; Sasaki, Y.; Sawada, S.; Akiyoshi, K. Shear flow-induced nanotubulation of surface-immobilized liposomes. *RSC Advances* **2012,** 2, 2682-2684.
25. Brazhnik, K.; Vreeland, W.N.; Hutchison, J.B., Kishore, R.; Wells, J.; Helmerson, K.; Locascio, L.E. Directed growth of pure phosphatidylcholine nanotubes in microfluidic channels. *Langmuir* **2005,** 21, 10814-10817.
26. Scheffer, L.; Bitler, A.; Ben-Jacob, E.; Korenstein, R. Atomic force pulling: probing the local elasticity of the cell membrane. *Euro Biophys J.* **2001,** 30, 83-90.
27. Picas, L.; Rico, F.; Scheuring, S. Direct measurement of the mechanical properties of lipid phases in supported bilayers. *Biophys. J.* **2012,** 102, L01-L03.
28. Nichols-Smith, S.; Teh, S.; Kuhl, T.L. Thermodynamic and mechanical properties of model mitochondrial membranes. *Biochi. at Biophys. Acta* **2004,** 1663, 82-88.
29. Radenovic, A. Optical Trapping. Advanced Bioengineering Methods Laboratory. École Polytechnique Fédérale de Lausanne
30. Hirokawa, N. and Noda, Y. Intracellular transport and kinesin superfamily proteins, KIFs: structure, function, and dynamics. *Phys. Rev.* **2008,** 88 (3), 1089-1118.
31. Deuling, H.J. and Helfrich, W. Red blood cell shapes as explained on the basis of curvature elasticity. *Biophys. J.* **1976,** 16, 861-868
32. Derenyi, I.; Julicher, F.; Prost, J. Formation and interaction of membrane tubes. *Phys. Rev. Lett.* **2002,** 88, 238101.
33. Pan, J.; Tristram-Nagle, S.; Kucerka, N.; Nagle, J.F. Temperature dependence of structure, bending rigidity, and bilayer interactions of dioleoylphosphatidylcholine bilayers. *Biophys. J.* **2008,** 94, 117-124.

34. Rawicz, W., Olbrich, K. C., McIntosh, T., Needham, D. & Evans, E. Effect of chain length and unsaturation on elasticity of lipid bilayers. *Biophys. J.* **2000,** 79,328–339.
35. Lee, C.; Lin, W.; Wang, J. Measuring the bending rigidity of giant unilamellar liposomes with differential confocal microscopy. *Laser and Electro-Optics. CLEO*, **2000**, Conference
36. Tokarz, M.; Hakonen, B.; Dommersnes, P.; Orwar, O.; Akerman, B. Electrophoretic transport of latex particles in lipid nanotubes. *Langmuir* **2007,** 23, 7652.
37. Adams, K. L.; Engelbrektsson, J.; Voinova, M.; Zhang, B.; Eves, D. J.; Karlsson, R.; Heien, M. L.; Cans, A. S.; Ewing, A. G. Steady-state electrochemical determination of lipidic nanotube diameter utilizing an artificial cell model. *Anal. Chem.* **2010**, 82, 1020.
38. Stepanyants, N.; Jeffries, G.D.M.; Orwar, O.; Jesorka, A. Radial sizing of lipid nanotubes using membrane displacement analysis. *Nano Lett.* **2012,** 12, 1372-1378.
39. Herold, C.; Leduc, C.; Stock, R.; Diez, S.; Schwille, P. Long-range transport of giant vesicles along microtubule networks. *ChemPhysChem* **2011,** 0000, 1-7.
40. Soumpasis, D. Theoretical analysis of fluorescence photobleaching recovery experiments. *Biophys. Jour.* **1983,** 41(1), 95-97.
41. Hirst, L.S.; Ossowski, A.; Fraser, M.; Geng, J.; Selinger, J.V.; Selinger, R.L.B. Morphology transition in lipid vesicles due to in-plane order and topological defects. *PANS*. **2013,** 110(9), 3242-3247.
42. Lindblom, G. and Oradd, G. Lipid lateral diffusion and membrane heterogeneity. *Biochim. et Biophys. Acta.* **2009,** 1788, 234-244.

Chapter 5

Conclusion & Future Work

5.1 Conclusion and Future Work

In this dissertation, two different experiments were carried out on lipid membranes. The first experiment focused on the effect of membrane phase structure between two different types of lipid, polyunsaturated (DHA-PE) and saturated (DPPC), using x-ray scattering. The drive for this project was to understand the role of the DHA-PE molecule in biological membranes by using a model system. Initially, we hypothesized that DHA-PE molecules would alleviate the tilt angle of the tilted DPPC $L_{\beta'}$ phase and induce phase separation at low concentrations. However, we obtained unexpected results concerning the former hypothesis. If DHA-PE alleviates the tilt angle of the $L_{\beta'}$ phase then it would increase the bilayer thickness; however, the bilayer thickness decreased. This was determined through fitting the peak of the $L_{\beta'}$ phase to obtain the d-spacing from the q vs intensity plots. Further analysis supported this finding such as the EDP, which indicated that the d_w remain unchanged while the d_{pp} decreased. Also, WAXS data agreed with the decreased bilayer thickness due to the increased chain packing distance between molecules. The latter hypothesis was correct as we observed phase separation at low concentrations. However, it was still a surprising result because it is quite difficult to imagine a single DHA-PE molecule finding another similar molecule in a sea of DPPC molecules. This experiment is still far from solving the mysteries of how DHA benefits health because we have yet to investigate the effect of DHA in cell membranes. However, the surprises we have seem from DHA-PE in this model system were the same surprises DHA plays in health. The findings of this experiment can be applied to biomaterials for strengthening lipid membranes of $L_{\beta'}$ phase, but more research is required as we have only stepped on new information about DHA. Future work would focus on different techniques to further support the increased tilt angle caused by DHA incorporation. Such techniques like transmission electron microscopy, AFM, NMR, and molecular dynamics would greatly help explain the increased tilt angle and decreased bilayer thickness. Another direction would be to use a similar molecule like DHA but without the problem of oxidation, such as with diphytanoyl lipids, because its methylated fatty acid tail causes the lipid to have high fluctuation like DHA.

The second experiment had two specific aims: lipid nanotube formation and methodology of determining the amount of kinesin motors for tubulation. The motivation of this project was to mimic and understand the formation of lipid nanotubes inside biological cells. Previous research has used kinesin supplied by ATP to extract nanotubes from GUVs, but it requires a constant supply of kinesin motors because of the detachment of kinesins. Therefore, we designed a simple system that can form lipid nanotubes without detachment of the kinesin motors by immobilizing the motors and generating nanotubes by drag force. The flow cell device was easy and quick to assemble, and formation of nanotubes occurred in few seconds. Moreover, readout of the kinesin motor count was fast using our theoretical approach. We found that nanotubulation from GUVs were dependent on the flow rate, GUV size, membrane rigidity, and number of motors anchoring the GUVs. Flow rate was inversely proportional to GUV size because low flow rate generates nanotubes from bigger GUVs while high flow rate generates nanotubes from smaller GUVs. This was because the required force for tubulation was 7.9 pN, which corresponded to the drag force produced from the GUVs and flow rate. Membrane

rigidity played a role in tubulation because membrane with high rigidity resisted bending of the membrane into tubes with higher curvature, as seen with DPPC membranes. Lastly, it was important to minimize the number of motors anchoring the GUVs in order to extract lipid nanotubes because high numbers of anchors immobilize the GUV while too few or no motors washed the GUVs with the flow. Using our theoretical formula approach, we calculated that tubulation occurred with 1 or 2 motors. Using this simple method, we generated stable tethered GUVs and lipid nanotubes due to multiple anchors along the nanotubes. This result may provide some insights to stable lipid tubules existing inside cells along the microtubule network. This system had minimum control of the flow rate; therefore, future work will be to design a microfluidic flow cell with multiple flow rates and stable flow. It will provide more accurate determination of the drag force generated from GUVs and longer period of stable flow. We only experimented with two different lipids, DOPC and DPPC, which leaves a lot of room for exploring other lipids and mixtures. Membrane consisting of different phases may generate surprising structure with our flow system. It will also be very interesting to work with different temperatures in our flow cell. Since DPPC is in $L_{\beta'}$ phase at room temperature, it will be interesting to transition the $L_{\beta'}$ phase into L_{α} phase to form lipid nanotubes and cool it back to room temperature. There are countless future experiments to explore. Moreover, our success of lipid nanotubes generation from this method can further be applied as biomaterial in tubular network applications.